DATA-DRIVEN MECHANICAL DESIGN AND CONTROL METHOD OF DEXTEROUS UPPER-LIMB PROSTHESIS

A Dissertation
Presented to
The Academic Faculty

by

Joshua Lee

In Partial Fulfillment
of the Requirements for the Degree
Doctor of Philosophy in the
Woodruff School of Mechanical Engineering

Georgia Institute of Technology
December 2022

DATA-DRIVEN MECHANICAL DESIGN AND CONTROL METHOD OF DEXTROUS UPPER-LIMB PROSTHESIS

Approved by:

Dr. Frank L. Hammond III, Advisor
School of Mechanical Engineering &
Department of Biomedical Engineering
Georgia Institute of Technology

Dr. Lewis Wheaton
School of Biological Sciences
Georgia Institute of Technology

Dr. Jaydev Desai
Department of Biomedical Engineering
Georgia Institute of Technology

Dr. Marco Santello
Biological and Health Systems Engineering
Arizona State University

Dr. Jun Ueda
School of Mechanical Engineering
Georgia Institute of Technology

Date Approved: July 27, 2022

To Mom, Dad, Sharon, and Soeun

ACKNOWLEDGEMENTS

I would like to thank my advisor Dr. Frank L. Hammond III for his continuing guidance and support throughout my studies over the last 7 years. Also, lab members in the Adaptive Robotic Manipulation Laboratory have always been supportive of my work and have provided challenges that were necessary to steer my work in the right direction. I thank my friends that have helped me loosen up in tense situations and have fun so that I could get back to work and progress through my studies. My parents and sister Sharon have made all of this possible through their continuing support and encouragement. I thank my wife Soeun for helping me get back to pursuing my studies during hard times in the pandemic, who has given me strength, support, and motivation to push me through the end of this study. I am truly blessed to have Soeun in my life. Finally, I thank God for empowering me to persevere through all my studies.

TABLE OF CONTENTS

LIST OF TABLES

LIST OF FIGURES

SUMMARY

With an increasing number of people, 320,000 per year, suffering from impaired upper limb function due to various medical conditions like stroke and blunt trauma, the demand for highly functional upper limb prostheses is increasing [1]; however, the rates of rejection of prostheses are high due to factors such as lack of functionality, high cost, weight, and lack of sensory feedback. Modern robotics has led to the development of more affordable and dexterous upper limb prostheses with mostly anthropomorphic designs. However, due to the highly sophisticated ergonomics of anthropomorphic hands, most are economically prohibitive and suffer from control complexity due to increased cognitive load on the user.

Thus, this thesis work aims to design a prosthesis that relies on the emulation of the kinematics and contact forces involved in grasping tasks with healthy human hands rather than on biomimicry for reduction of mechanical complexity and utilization of technologically advanced engineering components. This is accomplished by **1) experimentally characterizing human grasp kinematics and kinetics as a basis for data-driven prosthesis design**. Using the grasp data, steps are taken to **2) develop a data-driven design and control method of an upper limb prosthesis** that shares the kinematics and kinetics required for healthy human grasps without taking the anthropomorphic design.

This thesis demonstrates an approach to decrease the gap between the functionality of the human hand and robotic upper limb prostheses by introducing a method to optimize the design and control method of an upper limb prosthesis. This is accomplished by first, collecting grasp data from human subjects with a motion and force capture glove. The collected data are used to minimize control complexity by reducing the dimensionality of the device while fulfilling the kinematic and kinetic requirements of daily grasping tasks. Using these techniques, a task-oriented upper limb prosthesis is prototyped and tested in simulation and physical environment.

CHAPTER 1

INTRODUCTION

The development of robotic upper limb prostheses has always faced a dilemma of balancing between functionality, the ability to replicate the grasp performances of the human hand, and complexity, in terms of the number of the required control inputs and actuation methods. The functionality of a widely adopted single degree of freedom gripper and a more complex and expensive myoelectric controlled prosthetic hand differs vastly in terms of variety in grip patterns, the number of objects that could be grasped, and dexterity in grasp manipulation [2]. However, the preferences of prosthetic users towards single degree of freedom grippers outweigh myoelectric prostheses by far due to factors like simplistic control and low cost [3]. Thus, for the adaptation of prostheses with better functionality, the complexity of control and cost of fabrication needs to be addressed. Additionally, traditional upper-limb prostheses follow the ergonomics of anthropomorphism, while some others have explored the translation of the functions of the human hand to prosthetic devices [4]. However, only a few have explored the simultaneous translation of the kinematics and contact kinetics of anthropomorphic grasps to prosthetic grasps.

This thesis work aims to address the need for an economic and dexterous prosthetic hand by first devising a method to investigate the functionality of the human hand in terms of grasp kinematics and contact kinetics, outlined in detail in Chapter 2. Conventional methods of characterizing grasps have focused primarily on the kinematics and pose configurations of human grasps. However, only a few studies have investigated the contact forces involved in grasping tasks associated with activities of daily living, and none to our knowledge have investigated the use of a combined kinematic and contact force grasp dataset in the development of the design and control method of a robotic upper-limb prosthesis. Thus, a three-fold approach is taken to develop a grasp database to serve as a basis for the development of a functional upper-limb prosthesis:

1. **Aim 1:** Perform a set of human subject experiments where the subjects wear a customized sensorized characterization glove that captures the kinematics and contact kinetics of grasps to perform grasping tasks with objects typically involved in activities of daily living (ADL).
2. **Aim 2:** Extract the core components of grasp kinematics and contact kinetics with machine learning methods (principal component analysis and linear discriminant analysis) to develop a **grasp synergy matrix,** a concept first proposed by Ciocarlie et. al. where features of grasps, such as joint configurations or fingertip positions, are reduced to a smaller set of components for the automation of grasp synthesis [5].
3. **Aim 3:** Establish the kinematic and contact kinetic translation from the anthropomorphic grasps to robotic grasps by mapping the contact coordinates attained

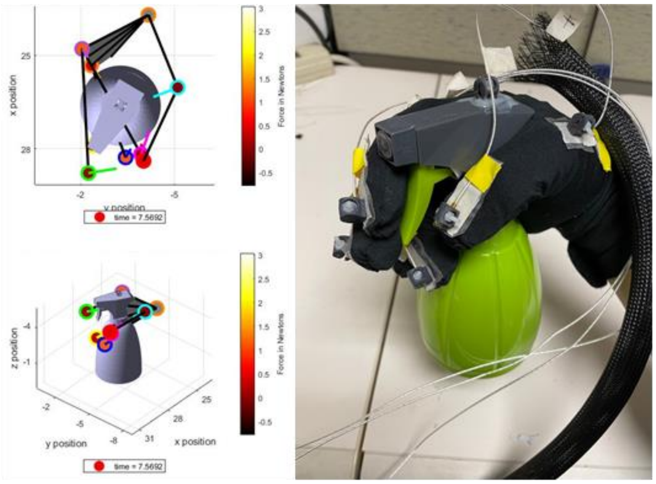

Figure 1: A frame of the grasping animation showing the human subject using a spray bottle. Colored circles represent fingertip and palm sensor locations, and arrows show the relative normal contact force vector.

from the product of the **eigengrasps**—a vector of coordinates in the grasp latent space—and the synergy matrix using a set of virtual spheres.

The benefits of integrating the kinematic components of grasps with the contact kinetics are analyzed using evaluation methods such as Calinski-Harabasz indices, F1-scores, and classification tests with confusion matrices. Figure 1 shows one of the examples of robotic grasps generated virtually with the eigengrasps tuned through MATLAB; grasps generated virtually are compared to those formed by human subjects.

Chapter 3 demonstrates the design and control method of a three-fingered design of a robotic upper-limb prosthesis motivated by the kinematics and correlation between the contact points on the human hand and from literature studies on the functionality of the human hand. First, the control method of an arbitrary robotic prosthesis using the combined kinematic and contact kinetic dataset is developed using the grasp synergy matrix mentioned in **Aim 3**. The method to develop a synergy matrix, attain the eigengrasps, and translate grasps using virtual spheres is further established in Chapter 3. After developing methods for forming synergistic poses and contact forces, a series of rudimentary prototype designs are considered (e.g. split-hook device, three-fingered gripper-type device) before developing the final prototype inspired by the grasp dataset attained from Chapter 2. The reduction from a fully anthropomorphic prosthetic hand to a three-fingered device simplifies control complexity and actuation requirements and reduces the

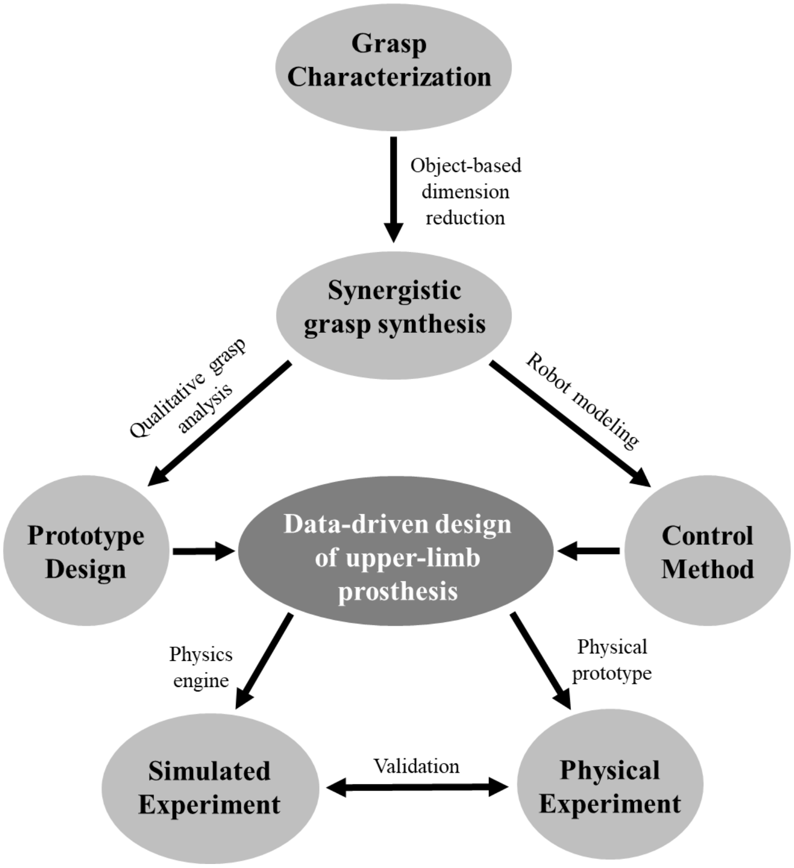

Figure 2: Core concepts and contributions of this thesis. The arrows show the correlations between each contribution. A data-driven design of upper-limb prosthesis is developed from a grasp study and is validated with experiments.

cost of fabrication and the overall weight of the system. The design methodologies and procedures to improve the repeatability and accuracy of the system are discussed in detail. The mathematical model of the system is optimized using a stereo camera-based calibration system.

Using the computer-aided design model of the prosthetic hand developed in Chapter 3, validation of the synergy-based control of the upper-limb prosthesis using the robot simulator, CoppeliaSim is explored in Chapter 4. The robotic structure is established such that the theoretical motions match those visually in simulation, and the inverse kinematics, contact kinetics, and world dynamics were configured to match the conditions of the prosthetic device and the real world. The world physics provided in CoppeliaSim are tested with a simple grasping task of a cylindrical

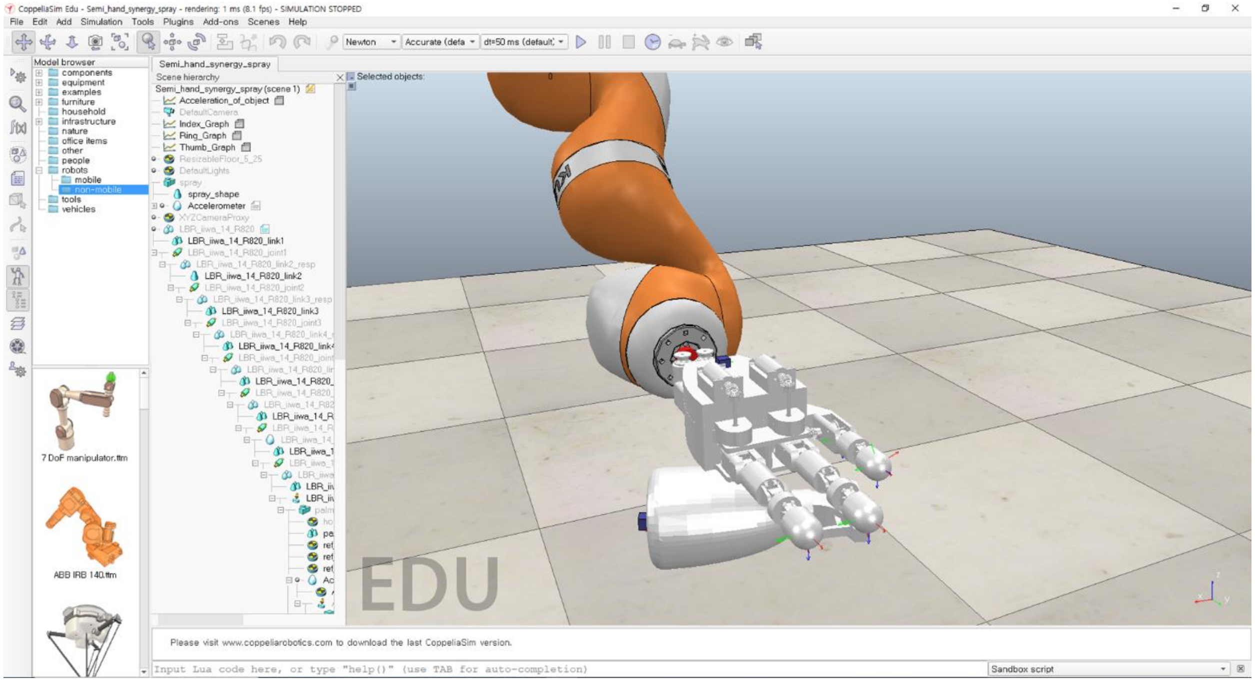

CoppeliaSim Edu - Semi_hand_synergy_spray - rendering: 1 ms (8.1 fps) - SIMULATION STOPPED

Newton

Accurate (defa

dt=50 ms (default;

Please visit www.coppeliarobotics.com to download the last CoppeliaSim version.

Input Lua code here, or type "help()" (use TAB for auto-completion)

Sandbox script

Figure 3: Simulation of grasps using the prosthetic hand imported to CoppeliaSim. The prosthetic device is attached to a virtual serial manipulator that induces perturbations to the grasps formed with the hand.

object, and the relationship between the contact dynamics and world dynamics is tested with varying masses of the cylinder. After validation, the synergy-based grasp pose configurations and contact force modulations are performed in CoppeliaSim using MATLAB as the source for computing the required joint displacements and torques for a given set of eigengrasps associated with the object to be grasped. Finally, a virtual experiment is designed and executed as shown in Figure 3 to test the grasp stability and robustness with the synergy-based method of grasp pose and torque modulation, compared to that without synergy-based torque modulation. The prosthetic hand is attached to the serial manipulator, KUKA IIWA 14, and is exposed to perturbations while maintaining grasps with multiple daily objects using synergy-based pose and contact force modulation.

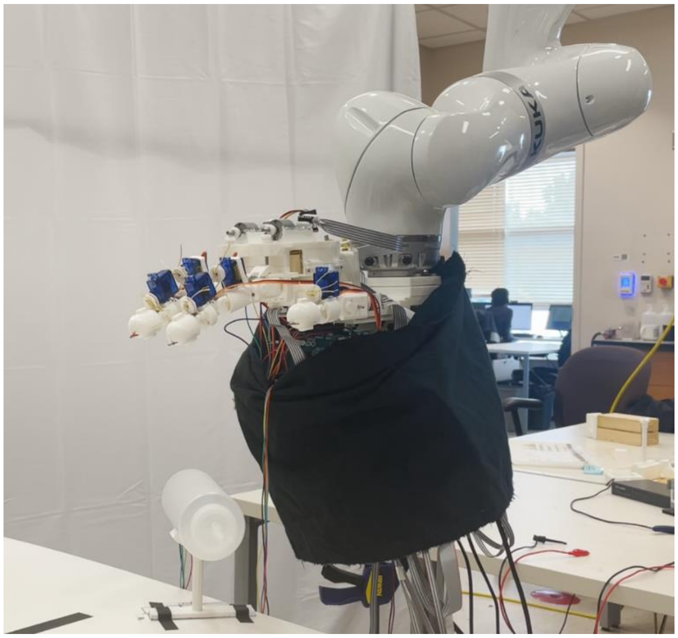

Figure 4: Setup of the physical experimentation with the prosthetic device mounted to the KUKA manipulator. The KUKA guides the hand to the target object, and the perturbation trial starts after the hand accomplishes its grasp.

Chapter 5 demonstrates experimentation with the physical setup of the prosthetic device with the KUKA manipulator as performed in simulation via CoppeliaSim. First, the synergy-based pose and torque modulation are realized using a custom-made graphical interface to interact with the microcontrollers that regulate input signals to the actuators. The sensing components (e.g. accelerometer) are also characterized for evaluation of grasp stability and robustness. Finally, as demonstrated in Figure 4, the prosthetic device is mounted to the physical KUKA manipulator, and perturbation trials are performed with the same objects test in simulation. The results are analyzed in detail for each of the objects tested in the experiment.

Finally, Chapter 6 summarizes the discoveries made in this thesis work and explores the potential applications of the grasp data-inspired design and control of a robotic prosthesis. The main findings of this thesis work are highlighted as well as future improvements that can be made further down the research paths.

CHAPTER 2

CHARACTERIZATION OF GRASPS WITH HUMAN SUBJECT EXPERIMENTATION ON GRASPING TASKS OF DAILY OBJECTS

2.1 Background

Previous efforts to study the dynamics and kinematics of grasping tasks performed with healthy human hands include visual inspection [6], the use of sensorized objects [7][8][9], visual tracking of objects and the hand using markers [10][11][12], and the use of a sensorized glove [13][14]. While all the listed studies produce valid and useful observations, the limitations of the studies are also apparent. The use of sensorized objects is advantageous in that it avoids issues with the variability of measurements between subjects fairly well, and the pressure distribution across the objects' surface geometries is simpler to track. However, this provides little information about the configuration of the hand grasping the object as well as the locations of the contact points on the hand, which are critical for the development of a prosthesis design. Marker tracking of the hand and the object is also a frequently adopted method due to ease of implementation and little limitation on the number of markers that could be placed on the objects. However, this introduces a problem of occlusion, which is expected to happen frequently in grasping tasks, and even with multiple recording devices, the exact configuration of each finger while in contact with the object may be difficult.

2.2 Introduction

This study utilizes a sensorized glove (TactilGlove) manufactured by Pressure Profile Systems to attain the contact pressure distributions across the palmer surface of the fingers and the palm. In addition to the provided system, the positional information of the configuration of the hand is attained using a set of electromagnetic position trackers (TrakStar) manufactured by Northern Digital Incorporation. While there have been several studies that utilize sensorized gloves for the characterization of grasps [13][14][15], this system can attain data sets like no other. Previous studies using a sensorized glove have focused on the grasp dynamics at static equilibrium at specific grasp configurations. While these studies are informative, they miss the dynamics and the kinematics during the process of reaching stable grasps. Then again, these measurements are not possible without simultaneous collection of time-synced data of the pressure distribution and configurations of the hand and the object at grasp. By using the combination of the sensorized glove and the EM trackers—integrated system shown in Figure 5—it is possible to attain time-relevant information of the grasp dynamics and the kinematics of healthy human grasps.

Figure 5: Photo of the TactileGlove with electromagnetic (EM) motion trackers attached. The inset zoomed-in image of the middle finger shows the tracker sensor mounted on a thermoplastic elastomer mount, fastened with a nylon screw to prevent EM interference.

2.3 Methods

2.3.1 Grasp Characterization Glove

We utilize an electromagnetic tracking system, (TrakStar 3D Guidance System, Ascension Technology Corporation) to track fingertip and wrist locations during grasping. A total of eight trackers are used: five for fingertips, one for the thumb base, one for the wrist, and one for the object location and orientation. The system measures the Cartesian coordinates of the trackers with respect to the electromagnetic transmitter as well as the internal Euler angles at a rate of 80 Hz—which seems sufficient given that similar studies that analyzes handshapes and hand kinematics using the Cyberglove uses joint angle data sampled at 50-70 Hz [16][17]. The Euler angles are used to attain the normal directions of the contact forces with respect to the force sensors.

The TrakStar system is susceptible to magnetic distortion from nearby conductive metals; precautions have been made to ensure that no metallic components are placed within 1m range and that objects used for grasping tasks are either non-metallic or are replaced with 3D printed PLA replicas. The 3D printed components are the door lever and key; others like knife, fork, and hammer are ready-to-use tools made of nonmetallic materials like ceramic, plastic, and rubber (mallet). The weight of the door lever does not play a big role in grasp as the lever is screwed to the door piece, and the subjects' tasks involve grasping and twisting the lever that's being held by the mount on the door piece. The key has a very small profile and weight, and grip force is more proportional to how hard the subject pinches and twists the key rather than the forces that counteract the forces of gravity. With the average weight of a house key being approximately 15 g (0.049 N in weight) and the variance of the pinch force being in the range of 14-20 N, weight only comprises 0.245-0.35% of the error. The system's performance specifications suggest a static accuracy, in optimal conditions, of 1.4 mm RMS error in position and 0.5 degree RMS error in orientation (experimental validation shows 1.001 mm RMS error in position and 0.03 degree RMS error in orientation) whereas previous studies done by Santina et. al. employs marker-based joint angle measurement for study on postural hand synergy with error ranging from 2.2 – 3.1 mm [18]. Provided that the motion spectrum of the grasp study lies between an average of 20 mm to 74 mm (computed from the standard deviation of position data of each tracker from the database), 1.4 mm can be regarded as an acceptable measurement error.

The force distribution across the palmar surface of the hand is measured using the TactileGlove developed by Pressure Profile Systems. It consists of 52 capacitive pressure sensors embedded in a nylon fabric glove. The TactileGlove measures the normal forces of contact as there are no commercially available sensors that measure tangential contact forces to our knowledge, and the study is limited to the resources available to us. Pressure distribution data is communicated via a Bluetooth dongle at a rate of 40 Hz. For synchronization with the 3D guidance system, the 80Hz kinematic data is downsampled to 40Hz. The performance specifications of the capacitive sensors provided by Pressure Profile Systems are: a full-scale range of up to 80 psi, a maximum force measurement of 28 N at the little finger, and 70 N at the remaining fingertips (with maximum force measurements from the database being 3 N at the little finger, 31.8 N from the remaining fingertips), maximum gain non-repeatability of 3%, and the minimum sensitivity of 0.04 N. The system integrity is tested with the Instron Force Testing System, where the contact dynamics within grasping tasks are modeled using a silicon molded hand (Dragon Skin^{TM} 10, Smooth-On), inserted inside the TactileGlove, shown in Figure 6. At each of the contact point locations where force data are utilized, 10 cyclic tests are executed by the Instron to verify if the TactileGlove

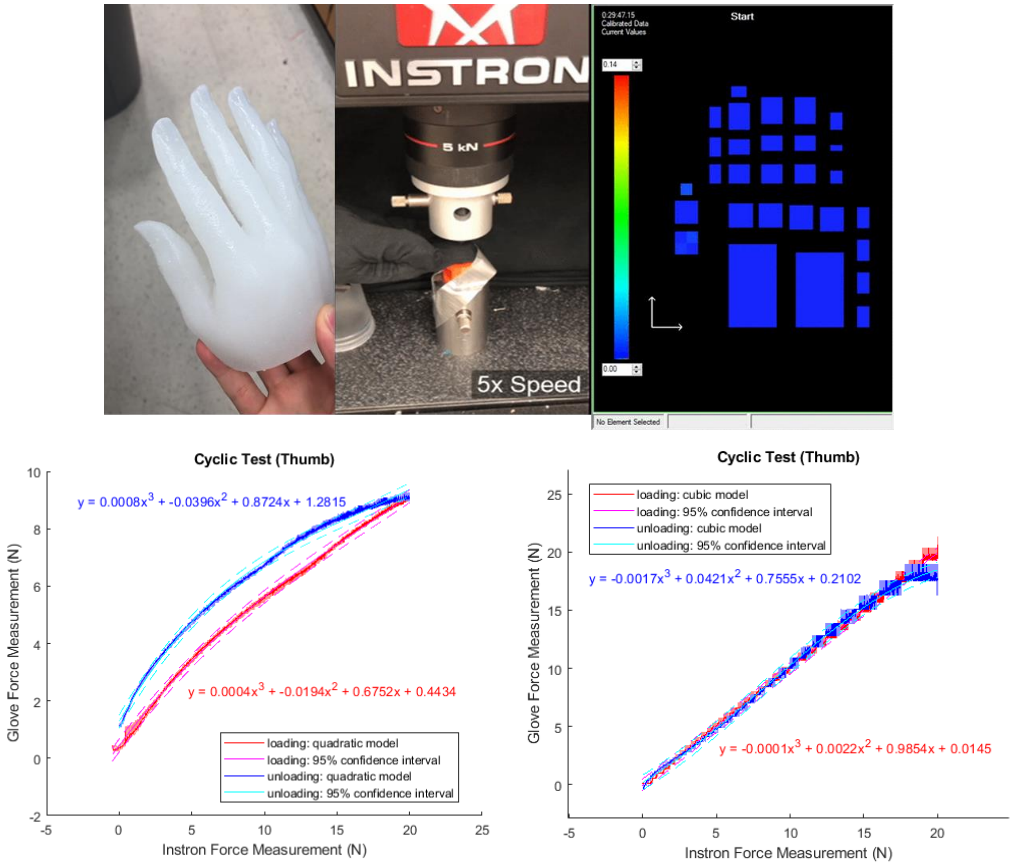

Figure 6: (Top) Testing measurements of the TactileGlove using a silicon-molded hand. Data are displayed in colormap using acquisition software Chameleon provided by the manufacturer. **(Bottom)** Cubic correlation between the Instron load cell and the sensors before calibration is shown on the left. Correlation post-calibration is shown on the right.

system yields a roughly linear correlation between the measured and actual force values. The resulting force mapping plot of Instron data to TactileGlove data shows a linearized force loading trend and a cubic unloading trend as shown in Figure 6. Discrepancies in force measurements and hysteresis greater than that suggested by the manufacturer appear to arise from the nonlinearity of the silicone hand more than from the non-linearity of the capacitive sensors themselves. To ensure that measured data matches actual force values during contact, the cubic regression equation derived from Figure 6 is used to map the measured data to the predicted actual forces. Validation of the cubic model using a new cyclic test is shown in Figure 6 where measured and actual force values show a linear loading trend with the first and second terms in the cubic equations being significantly less than the third and fourth terms. The unloading trend has relatively high first and second-order terms, but its discrepancy is concentrated at 18N or higher. As such, a cubic model is used to predict force values when pressure values are above 18N and the pressure differential is negative.

2.3.2 Data collection from human subjects

To develop a database of the grasp kinematics and kinetics of daily grasps, human subjects were invited to perform various grasping tasks while timestamped position and pressure data are collected. Subjects were provided with the characterization glove and 10 random objects from a pool of 36—chosen from a combination of objects used in previous works in grasping—listed in Table 1, and were asked to perform tasks typically associated with each object like tossing the tennis ball or swiping the credit card on a reader [19][20][21][22]. Refer to Appendix A for the mass and volume of each object used in the experiments. The experimental protocol for the study included the following steps:

- **Briefing:** Subjects are briefed about the protocols and process of the study as well as the precautions to take for safety and proper measurement (lasting ~10 min.),
- **Subject Training:** Subjects are asked to wear the provided motion/force tracking glove and are given a training period for using the glove to manipulate the objects without tampering with the sensor readings (~15 min.),

- **Grasping Trials:** For each object, subjects perform the tasks specific to the given object for approximately 30 seconds for 10 total objects (~15 min.),
- **Object Change:** Data are recorded and saved to archive after each grasping task; the EM tracker is removed and placed on a new object after each run (~10 min.),
- **Post-Trial Survey:** The subjects are asked survey questions relating to their experience during the study and are asked for feedback (~10 min.).

The experiments lasted approximately one hour, in total, per subject. All experimental procedures have been approved by the Georgia Institute of Technology Institutional Review Board.

Nine subjects participated in the study over a period of two weeks. While some previous works had each subject grasp the entire set in the object list, our work focuses more on the in-depth dynamics of grasp rather than mere postural analysis, requiring more time from the subjects to participate in each grasping task [23][24]. Requiring subjects to perform dynamic tasks in all 36 objects would be too taxing, and bias due to mental or physical fatigue may occur (considering that mental fatigue was reported in the post-study survey). Thus, we had to limit the study so that at least 2 or 3 grasps were attained for each object, where a similar number of grasps was used per object in some other previous works [19][21].

Table 1: List of all objects used in human subject experiment. A total of 36 objects are chosen from a combination of items used in related works.

Door lever	Peeler	Key	Toothbrush	Milk carton	Book
Kitchen spoon	Cubic prism	Comb	Knife	Spray	Espresso cup
Wine glass	Pen	Lid of a jar	Tennis ball	Glass bottle	Tape roll
Screwdriver	Coffee mug	Dust brush	Hammer	Game controller	Credit card
Squeeze bottle	Bowl	Measuring cup	CD	Cereal box	Spoon
Tumbler	Notebook	Whiskey glass	Fork	Dish	Mouse

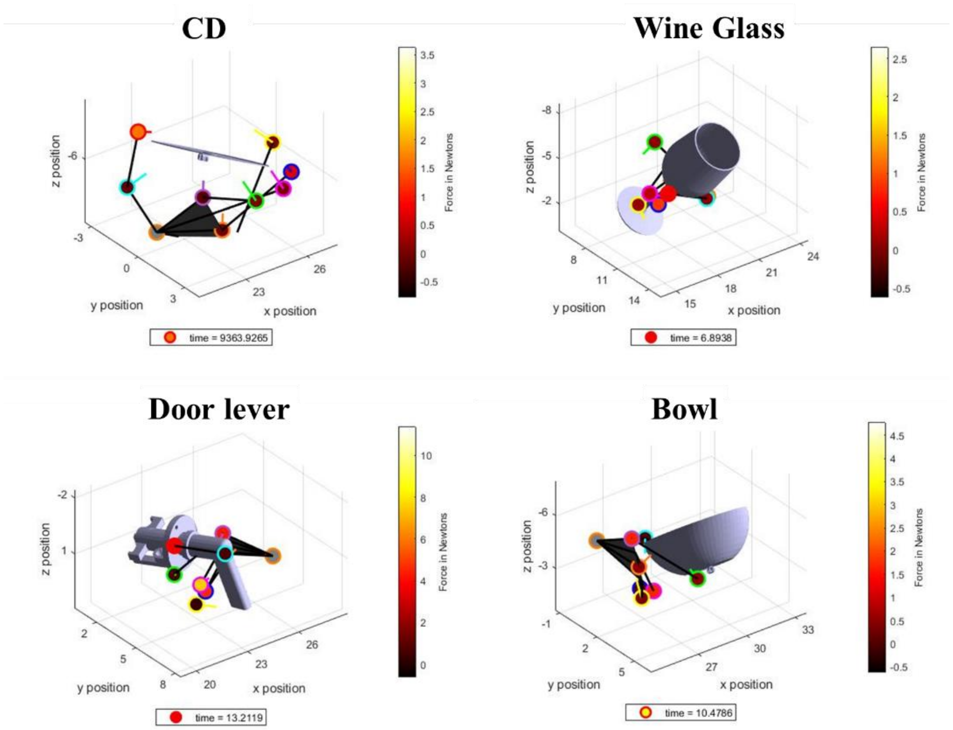

Figure 7: Frames of graphical representation of grasping tasks by human subjects. A skeletal representation of the hand allows easy visualization of different hand configurations. The color infills at critical locations of the hand illustrate the contact dynamics of the hand during task performance.

For all objects, the subjects started from a pre-grasp pose where all the digits are extended and free from contact. The subjects then reached for the object and closed in their digits with as much contact as they needed to form a firm, stable grasp with no slippage. Then, subjects performed tasks that are typically associated with each object (for example: lift and toss a tennis ball, rotate the door lever and pull the door-piece about its hinge, and slide the computer mouse across the table surface). Refer to Appendix B for the grasp pose used (from grasp taxonomy by Feix et. al.) in each object and the mass and volume of each object [25]. Finally, the subjects returned the objects to their original positions and moved their hands away from the object with all the fingers flexed.

The subjects were required to be: right-hand dominant, able to grasp daily living objects without hindrance, able to speak English fluently, able to give written consent, and be 18 years old or higher.

For the post-trial survey, some reported mental fatigue and/or hand fatigue at the end of the study, and some reported that their grasps differed from natural grasps due to slipperiness induced by the surface properties of the glove system.

Ten trials were performed by each subject, and the resulting grasp database consists of 90 video files of 36 objects, totaling 45 minutes' worth of data. The execution time to generate animated models for nine subjects was approximately 15 minutes, (1.67 minutes per subject), and the entire file size including raw data, CAD models, and video files totaled 2.91 GB (324 MB per subject). The system can generate a simplistic and informative graphical representation of the grasping tasks with 324 MB worth of data within 62 minutes (60 minutes of data collection and two minutes of graphics generation) per subject. The frame rate for the animated models is high enough to illustrate, in detail, the low-bandwidth interactions associated with normal usage models for objects of daily living, but not high enough to register events such as object slip and vibration, which have frequency components in the 100's to 1000's of Hz.

2.3.3 Identifying core components of grasps

We hypothesize that just as the principal component analysis of the joint orientations of the hand has led us to better understand and make predictions grasps and perform optimization of grasps, analysis of the force distribution across the palmar side of the hand may aid our understanding of optimal grasps and grasp predictions [20]. Kinematic features of grasp used for position data are the Euclidean distance between each of the fingertips and the wrist and the rotational displacement: yaw and pitch, between the wrist and fingertips. We assume that these features would sufficiently describe the grasp kinematics as similar features have been used by Romero et. al. where they have been successfully able to extract postural synergies by using fingertip positions for grasp features [26]. In addition to using kinematic data for analysis, we have performed a principal component analysis of force distributions of the hand at the fingertips and three evenly spaced positions on the palm. Analyses have been performed separately for the pre-grasp phases and full contact phases for comparison with previous works, where the gradual evolution of grasps occurs during the pre-grasp phase and where grasps are most fully distinguished in the full contact phase [27].

Principal component analysis (PCA) has been performed on each set of subject trials with a different pool of 10 objects as the inter-subject variability was too great to perform meaningful representation on the 2D plane via PCA analysis. Within each trial, two separate sets are considered: the entire kinematic and kinetic dataset in the pre-grasp phase and the entire dataset in the full-contact phase for comparison with previous works, where the gradual evolution of grasps occurs during the pre-grasp phase and where grasps are most fully distinguished in the full contact phase as suggested in Figure 8 [27]. For each set, each variable is normalized with respect to its mean and standard deviation (e.g., force values at the thumb normalized by mean force and standard deviation at the thumb). MATLAB's `pca` function that takes the m-by-n kinematic and contact force data (m: number of observations within each trial; n: number of variables like Cartesian coordinates of the thumb, pressure at the palm) as input is utilized to generate n-by-n (n: number of variables) principal component coefficients with columns sorted in descending component variance. The product of the m-by-n dataset and the principal component coefficient

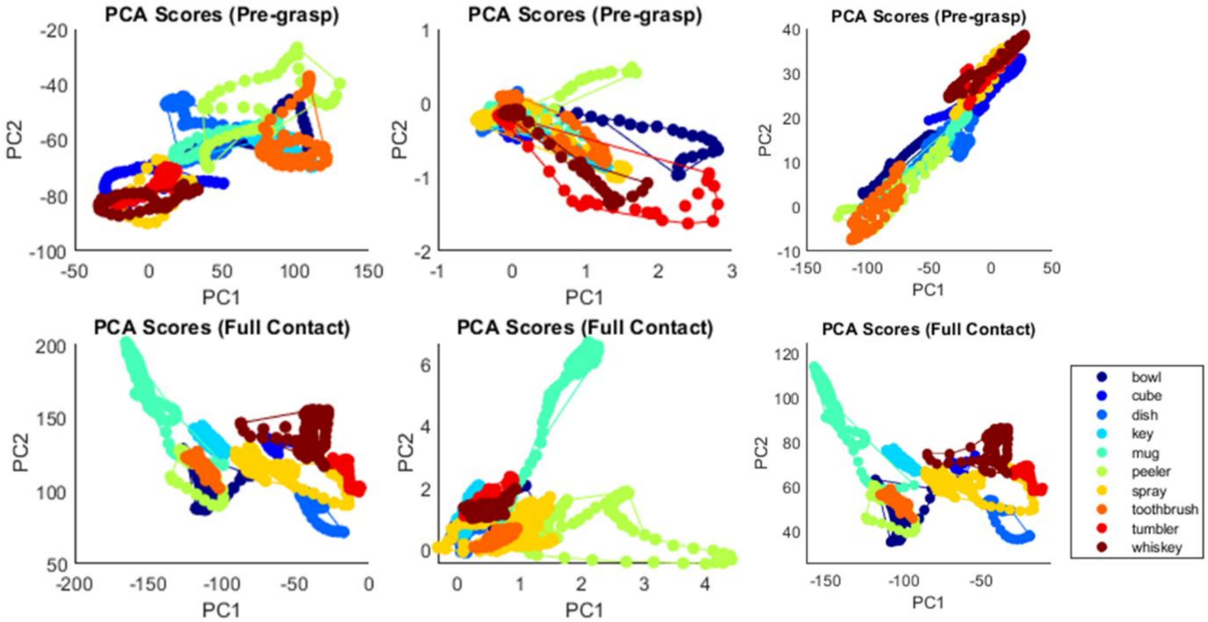

Position data only **Force data only** **Combined (Force + Position)**

Figure 8: Principal component analysis of grasp data for Subject 6. Principal components are plotted for two different phases of grasp, where **(left)** show PCA performed with position data only, **(middle)** performed with force data only, and **(right)** performed with combined position and force data. Each axis in the PCA plot represent variance from the means for each dataset, and more separation from the means indicate better separability between each group (object).

matrix gives the m-by-n score matrix. The first two columns of the score matrix are the two principal components. To account for the difference in variable units, one in millimeters and the other in Newtons, each variable is normalized by its mean value and standard deviation of that variable using the equation:

$$z_{ij} = \frac{x_{ij} - \bar{x}_j}{s_j} \tag{2.1}$$

By utilizing PCA to represent data in the 2D plane, we aim to demonstrate 1) this study's credibility with statistical validation by showing that different grasp poses lead to its mapping at different spaces in the latent space (Starke), and 2) demonstrate that adding force components to the grasp dataset yield better isolation of different grasp poses, which we plan to argue by using the Calinski-Harabasz (CH) Index, as it is known to be an effective method for estimating clusters with principal component analysis [28][29][30]. One such analysis is shown in Figure 8, where the principal components are plotted in 2D for different phases of grasp. Evaluation of the percent variance of the principal components has shown that the first two components comprise 56.5% of the total variance in a full force enclosure stage. PC analysis with only kinematic data showed that the first two components comprise 67.2%, and analysis with force data only showed a composition of 70.7%, where literature suggest that the rule of thumb for choosing the number of components should be such that the cumulative percentage of variance should be 70 – 95% [31]. This leads us to believe that two-dimensional representation of grasps may suffice for isolated grasp data (kinematic or dynamic), but higher-order principal components are not negligible for the combined data. This result is comparable to previous works as principal components analysis of joint positions reveals that the first two principal components comprise 84% of total variance [20]. Greater dominance of the first two components from previous works is observed as joint angle features within a digit are more closely linked to each other than are features from Cartesian coordinates as used in this study. Lesser dominance of the first two components using the combination of position and force features is predictable as two different qualities (kinematic and kinetic properties) are being analyzed simultaneously.

Representations of multiple grasp configurations are shown in two-dimensional plots using the first two principal components in Figure 8 for the two grasp phases. Clusters formed by grasp components for each object type are visibly less separated in the pre-grasp phase than during the full-contact phase, which concurs with previous works. Use of position data only shows better isolation of grasps in the pre-grasp phase understandably as most contact between the hand and the object occurs only within the last few seconds of the pre-grasp phase. Grasps for different

Table 2: Calinski-Harabasz (CH) Indices for all Subjects. Higher values indicate better isolation between different types of grasps formed

	Position data only		**Force data only**		**Combined Data**	
Subject Number	Pre-grasp	Full Contact	Pre-grasp	Full Contact	Pre-grasp	Full Contact
1	36.7	1712.1	17.2	1820.9	23.5	2362.2
2	70.3	950.5	40.6	406.2	63.7	1328.4
3	90.9	1016.6	67.5	710.6	96.3	2064.1
4	51.8	209.6	13	1134.6	24.3	587.1
5	39.3	438.2	37.9	657.6	39.7	804
6	143.5	792.5	24.1	401.4	82.8	807.5
7	559.1	2253	66.1	1108.2	379.4	3037.5
8	133.6	1048.6	40.9	1065.5	110.3	1605
9	413.7	1313.1	105.9	407.8	360.2	798.2

objects are better isolated in the full contact phase, with some objects like the mug and the peeler being much more isolated than other objects as grasp poses and pressure distributions are less uniform with specific digits being more utilized than the other (i.e. index and thumb apply higher pressure with the hand grasping the handle of the mug). The limitations of the PCA analysis are that it is a non-supervised learning method and that it does not take into consideration the separability of data points between clusters.

To compare the informativeness of data between combined and isolated grasp data, the level of compactness and separation of clusters formed by the latent representation of data was evaluated using the Calinski-Harabasz (CH) Index, which evaluates clusters by the ratio of between-cluster sums of squares (SSB) and within-cluster sums of squares (SSW),

$$CH_k = \frac{SS_B}{SS_W} \times \frac{N-k}{k-1} \tag{2.2}$$

given the number of observations N and number of clusters k. In other words, a high-value CH index argues that different grasps are well-isolated with respect to each other, and the data points are densely populated in each grasp type. The CH indices for all subject trials for each stage of grasp (pre-grasp vs full contact) as well as for the utilization of data types (combined vs. isolated) are shown in Table 2. CH indices at the full contact phase seem to be on average 13 to 30 times greater than those at the pre-grasp phases, as we have observed visually with the 2D representation. We are also able to observe that the combination of position and force data yields CH indices on average 1.5 times greater than that from position data and 2 times greater than that from force data in the full contact phases, supporting our hypothesis that the addition of kinetic information to grasp analysis allows better distinction between different poses. However, during the pre-grasp stage, CH indices from position data were 1.4 times higher on average than that of the combined data. This can also be expected as the pre-grasp phase provides little information about the contact forces being involved, and only a fraction of the grasp phase exists between the start of contact and the full force closure. High variability of the CH indices from subject-to-subject results from the randomness of the object sets for different subjects; for one subject, the set of objects may require similar grasp poses and contact forces, resulting in a lower CH index. For a different subject, one may be provided with a set of objects that require a wider range of grasp poses and forces, resulting in a higher CH index. For example, subject 4 in Table 2 had five objects in the same column (power grasp with opposing palm, column 2-5) in Feix et. al.'s grasp taxonomy chart whereas subject 7 had no more than two objects that require grasps in the same column (Refer to Appendix A & B) [25].

2.3.4 Grasp classification

In addition to representing data with PCA on a 2D plane, we have also utilized linear discriminant analysis (LDA), which is also a dimensionality reduction technique like PCA, but instead classifies data with given labels whereas PCA is an unsupervised learning technique [32]. We use linear analysis rather than quadratic analysis under the assumption that covariance between each object class is roughly the same. We have designated 50 random observation values from each object set for test data, and the remaining observations were used to train the classifiers. Classifiers are trained using labels for each observation and by finding the means ($\boldsymbol{\mu}$) and covariance matrix ($\boldsymbol{\Sigma}$) for each class using the equations:

$$\mu_k = \frac{\sum_{n=1}^{N} M_{nk} x_n}{\sum_{n=1}^{N} M_{nk}} \tag{2.3}$$

$$\Sigma = \frac{\sum_{n=1}^{N} \sum_{k=1}^{K} M_{nk} (x_n - \hat{\mu}_k)\,(x_n - \hat{\mu}_k)^T}{N - K} \tag{2.4}$$

where M is the class membership matrix with M_{nk} = 1 for the nth observation belonging to class k, given N observations and K number of classes. Classifiers in the pre-grasp phase were trained separately from those in the full contact phase. Using the pre-trained classifiers, objects were identified from the test samples using prediction classification that minimizes cost:

$$\hat{y} = \underset{y=1,\ldots,K}{\arg\min} \sum_{k=1}^{K} \hat{P}(k|x) C(y|k) \tag{2.5}$$

For $\hat{y}$ the predicted class, $C(y|k)$ the cost of placing observation as y for its true class k, and $\hat{P}(k|x)$ the probability that observation x is in class k, where P is a function of the mean and the

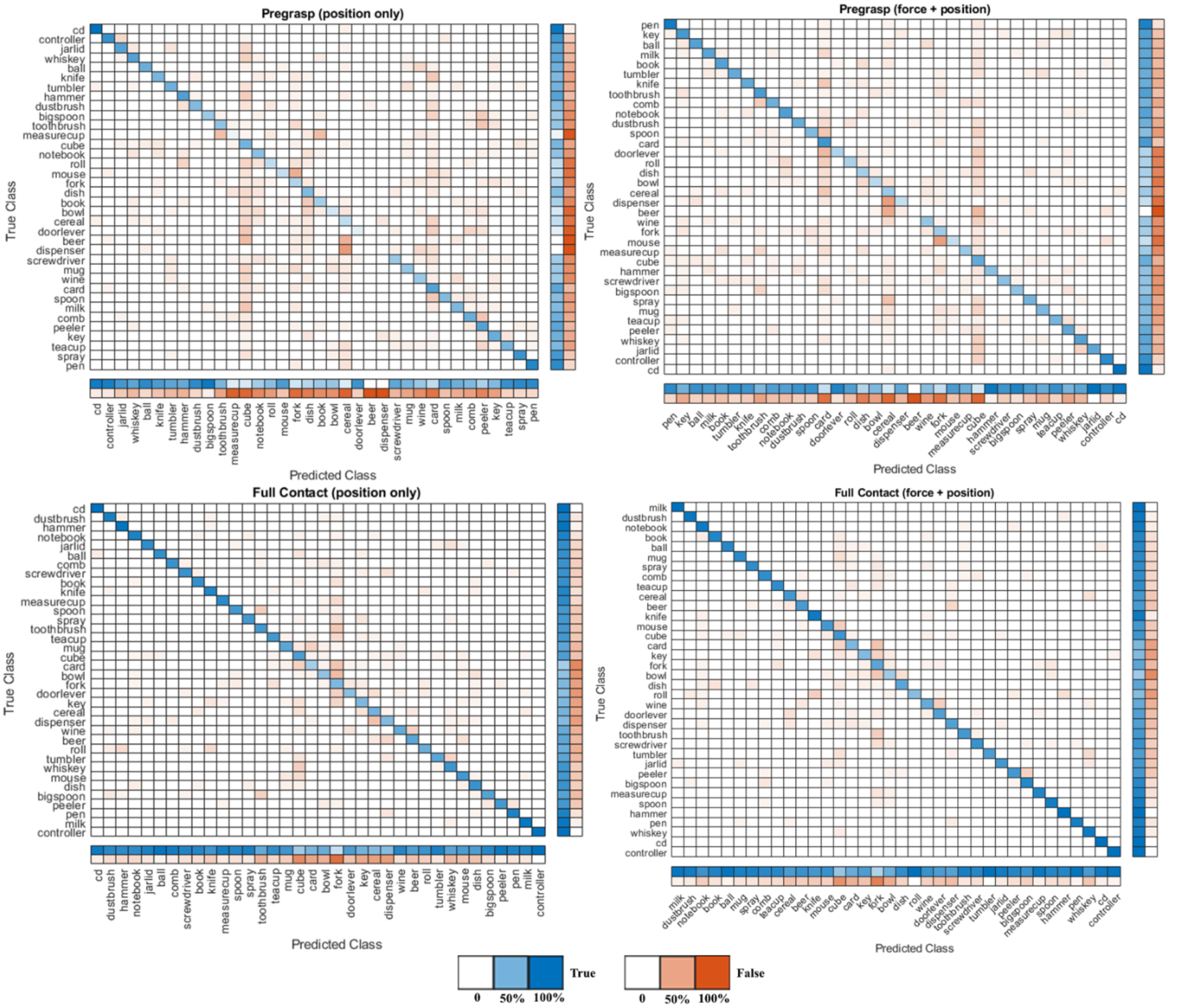

Figure 9: Confusion matrix of object identification using LDA. Object categories are sorted such that similar classes are clustered together (minimizing distances of the off-diagonal elements). In general, the diagonals of the matrix with the combined data have thicker colors (high true positives), and the off-diagonals have thinner colors (low false positives).

covariance matrix. Using the means and covariance matrices from the trained classifiers, we have generated confusion matrices of object identification using combined or isolated grasp data and compared the performances of each.

To further compare the informativeness of the combined kinematic and dynamic grasp data, three discriminant analysis classifiers have been trained to fit all subject trials with 36 total object labels: one with only position data, one with force, and the last with the combination of both. We have generated confusion matrices for all three for the pre-grasp phase and the full contact phase as shown in Figure 9. The orders of the objects in the confusion matrix have been sorted such that similar classes are clustered together by minimizing the off-diagonal elements of the matrix. Assuming that our hypothesis is valid, the addition of force features to grasp analysis should improve the classifications made by the combined dataset. As demonstrated in Figure 9, confusion matrices generated with different datasets in the full grasp phase further affirm the benefits of using combined kinetic and kinematic analysis of grasp poses for the characterization of daily grasping tasks. Data also show that the addition of force features to grasp analysis in the pre-grasp phase, however, does not benefit grasp characterization, if not degrade the classifier's performances. The accuracy of the classifier is evaluated using the F1 score:

$$F_1 = \frac{tp}{tp + \frac{1}{2}(fp + fn)} \tag{2.6}$$

where tp is true positive, fp is false positive, and fn is false negative.

1) **Analysis of confusion matrices in the pre-grasp phase:** Comparison of the confusion matrices on the top row (data in the pre-grasp phase) to the ones on the bottom row (full grasp phase) demonstrates that predictions made by the LDA classifier have shown to be much more inaccurate in the pre-grasp phase than in the full contact phase as grasps are premature in their development, making it harder for the classifiers to predict each grasp type. The dataset with only kinematic data is able to categorize the objects with an accuracy of 58.16% based on the F1 score. Unlike the other objects, the pen, CD, game controller, and spray bottle appear to require pre-grasp poses that are somewhat characteristic in nature (like stretching all digits widely to grasp a CD, making a wide tripod shape before grabbing the spray bottle), making it easier for the classifier to

place its predictions correctly. Data from the combined dataset predict the objects with an accuracy of 64.86%. Confusion may have arisen from the brevity of contact in the pre-grasp phase before the formation of full contact with the spray bottle. The cube, roughly the size of one’s fist, has the highest number of false positives from both position-only data and the combined data, presumably due to frequencies of objects requiring the same sphere finger-type grasp taxonomy, involving similar grasp pose and contact forces. Overall, however, the combined dataset improves classification with a 6.7% increase in accuracy.

2) **Analysis of confusion matrix in the full contact phase:** Confusion matrices generated with dataset in full contact also provide evidence that kinetic information is additive to grasp characterization and classification of grasp types. Again, the cube seems to create the most confusion among groups, and the fork yields the second-most false positives for all data types. With the position-only data, 82.66% accuracy is attained based on the F1 score. The confusion matrix with the combined force and position data shows an improvement in classification with 87.50% accuracy, an improvement of 4.84%. It can also be observed that adjacent objects have somewhat similar grasp pose and contact dynamics in ADL, such as fork and spoon, tennis ball and cube, or hammer and lint roll. It can also be seen that higher false positives and negatives occur between two more similar objects than others. The frequencies of case matches between combined data (force and position data) and position-only data are compared in detail as shown in Figure 10. The LDA classifier using the combined data has significantly more case matches throughout most object categories, and the classifier trained with position data has better case matches for only 5 objects out of 36. Overall, the combined data are able to achieve 4 more case matches on average for each object than the kinematic data. Objects with higher case matches with

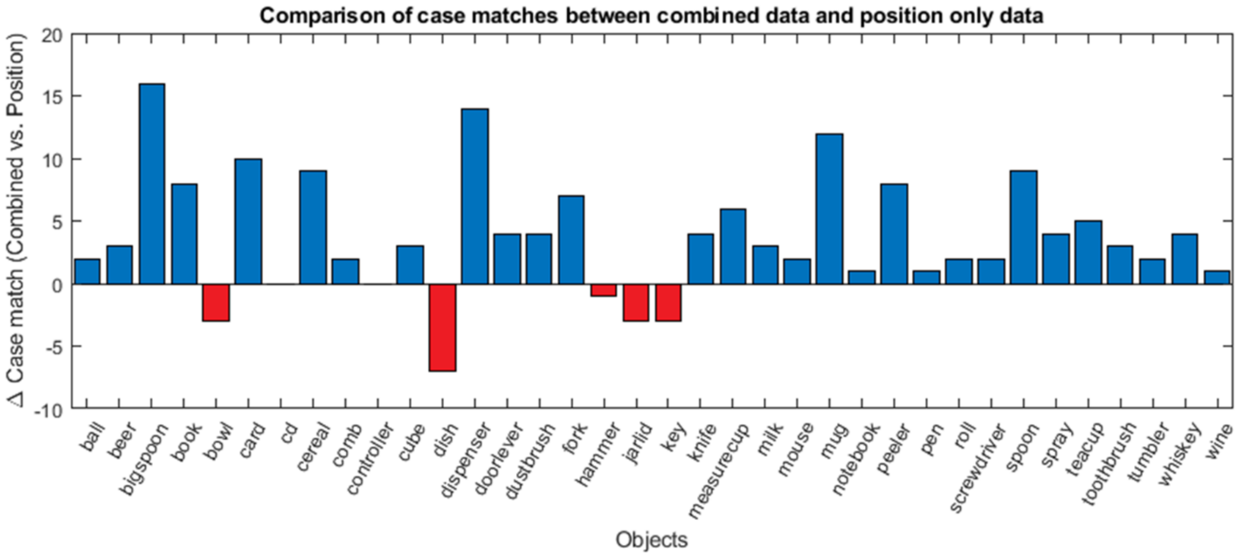

Figure 10: Comparison of case matches between combined force and position data and position only data in the full contact phase. The y-axis corresponds to the difference between case matches with combined data and matches with position data. There are 50 cases for each object.

the position-only data have a commonality, with the exception of the key, that there is a somewhat equal distribution of forces across the fingertips, possibly adding confusion between these objects.

3) **Comparison of results to previous works:** LDA classified with position data only is comparable with previous works performed by Santello et. al., as using the combination of LDA and fuzzy clustering technique has yielded 40 to 50% prediction probability, and the classifier using position data collected from this experiment, although a direct comparison is difficult due to difference in the experimental setup and apparatus, yields a mean of 82.66% accuracy. On the other hand, the combined force and position data show a mean case match probability of 87.5%.

Comparing this result to a more recent study performed by Sundaram et. al. [13], where a scalable tactile glove was fabricated, and instead of taking a kinematic and kinetic analysis approach, they have chosen to utilize a convolution neural network from tactile sensor inputs for object classification. The accuracy of posture-based classification without applying neural networks is lower than the study performed by Sundaram et. al., with a mean accuracy of 83.5%.

With the augmentation of force data, however, our classifier is able to achieve higher accuracy results. Liu et. al. have attained 94% accuracy from grasp posture with 3 large profile objects; however, their results had 43% accuracy on thinner objects (book, disk, cylinder) [33]. Li et al. used a 3D convolutional neural network to classify gestures with 65.35% [34]. Finally, Zhang et. al. obtained 91.96% accuracy with CNN and data augmentation and 72% without [35]. With rigorous machine learning, classification results greater than 87.5%, as observed from our results, are shown to be obtainable without the contact force information. However, a hopeful prediction can be made that the combination of simultaneous kinetic and kinematic grasp analysis with the convolution neural network learning techniques may yield greater object classification results than any other methods.

CHAPTER 3

DESIGN OF UPPER-LIMB PROSTHESIS WITH REDUCED DIMENSIONALITY

3.1 Background

3.1.1 Demand for upper-limb prosthesis and adoption rates

6 million people in the U.S. suffer from impaired upper-limb function due to a variety of medical conditions including congenital defects stroke-induced neurological injury, blunt physical trauma, and various diseases that require surgical modification of the hand anatomy [36]. The disruption or loss of upper-limb function can, depending upon the severity, prevent a person from performing everyday grasping and manipulation tasks, and can significantly impair development and diminish the quality of life. Conventional physical rehabilitation is very often an effective means of restoring function to the upper limbs of patients suffering from moderate neurological injury [37]. However, for patients suffering from severe neurological injury or disfiguration by disease or physical trauma, body-powered or electrically powered assist devices and robotic prostheses are often the only means of recovering the functionality required for activities of daily living (ADL) [38][39].

3.1.2 Factors leading to rejection of prosthetic devices

Consequently, an increase in demand for upper limb prostheses is observed as they are often the only means of recovering functions of activities of daily living (ADL) [40][41]. However, rates of prosthesis adoption are low due to lack of functionality, high cost, weight, and lack of sensory feedback [2][42][43]. Most common forms of prostheses include body-powered split hook devices and electrically-powered anthropomorphic arms as shown in Figure 11 [44][45], where many share the problem of diminished dexterity and functionality [2][47][48]. Examples of non-

Figure 11: Examples of prosthetic devices readily available in market. **(left)** The Vari-Pinch Prehensor^{TM} split hook-type prosthesis is developed by Toughware Prosthetics. **(right)** The Bebionic myoelectric prosthesis is developed by Ottobock.

anthropomorphic designs of upper-limb prosthesis include body-powered split hook devices, where most share the problem of diminished dexterity and functionality. One of the most common forms of body-powered prostheses is split-hook prosthetic devices like the Vari-Pinch prehensor, powered by motion from the shoulder joint [44]. While it poses benefits of being lightweight and inexpensive for its capability of generating 5 pinch patterns and high pinch force, its functionality is still limited to grasping a narrow range of objects, and an even narrower range of utilizing the grasped objects.

Some have explored the use of myoelectric prostheses with anthropomorphic designs [49][50][51][52]; these, however, are economically prohibitive and also suffer from control complexity due to increased cognitive load on the user, resulting from a dimensional reduction of a 27 degrees of freedom system of the hand to an eigenspace of grasps from a combination of inputs of 8 or less from the myoelectric sensors [46][50]. Most of the listed solutions share problems that may arise from the tendency to use anthropomorphic hand models to design devices. Thus, deriving a design from the functions of the human hand, not its anatomical configurations, may alleviate some of the aforementioned problems.

The efficacy of upper-limb prostheses is predicated upon several factors including (1) the functional improvement availed by the assistive device prescribed for treatment and (2) the patient's level of engagement in rehabilitation and treatment [53][54]. Device functionality can be described as a function of its manipulation capabilities (e.g. dexterity, strength, response time), while patient engagement can be seen as a product of human-device interface quality and device adaptability [55]. Thus, this thesis work aims to develop a utility-oriented design of a robotic upper-limb prosthesis that enables easy of control with high dexterity while maintaining a user-friendly form factor.

3.1.3 Motivation to explore alternative designs

While the anthropomorphic prosthetic designs pose the advantage of taking the most natural form in terms of appearance and increase the likelihood of adoption for aesthetic reasons, there are logical reasons to explore other non-anthropomorphic designs for upper-limb prostheses. First, the human hand is designed to accommodate various biological conditions that constitute the manipulation of the hand, which should not be a limiting factor for designing a synthetic upper-limb prosthetic device. Also, imitating the anatomical configuration of the hand poses challenging and expensive problems in terms of control as the human hand has 24 degrees of freedom, and reduced-complexity design often results in reduced functionality and mechanically trivial components. Finally, with the technological advancements that the scientific community has accomplished within the past decades, it is logical to take advantage of the mechanical power and the computational strength of human-synthesized products for the design of prosthetic devices. Thus, this study proposes to develop a data-driven prosthetic design framework that aims to replicate the dexterity and force output capabilities of the human hand while performing activities of daily living (ADL), without requiring the prosthesis to take the anthropomorphic design. Using grasp datasets from human subject studies, an optimal design of upper-limb prosthesis will be explored, and the design with optimal force distributions and joint configurations for various activities of daily living will be selected for human subject tests.

3.2 Introduction

The grasp data sets attained from human subject experiments were utilized for the development of a grasp function-oriented robotic upper-limb prosthesis. By studying the essential mechanics of healthy grasps such as the joint and torque limits and the grasps quality measures, it is possible to explore other design methods of upper-limb prostheses by focusing on its functional performance before considering the structural component of the design. Current designs of upper-limb prostheses are either motivated by the anatomy of the human hand (anthropomorphic designs) or by simplistic functions of daily tasks like grasping and holding objects at steady-state. For example, the Bebionic Hand by Ottobuck and i-Limb by TouchBionics are representative designs of myoelectric prostheses motivated by the anatomy of the human hand [56][57]. While these designs enable 20-30 different grip patterns with fast digit speed and high actuation torques, the efficiency of their performance of dynamic tasks is yet unexplored as these device designs are optimized for stable, steady-state grasps. However, studies show that a large portion of the activities of daily living involves relative motion of digits during the tasks, such as writing with a pen or turning a doorknob [58][59][60].

To design a prosthesis motivated by the dynamics and kinematics of daily tasks involving grasp and tool use, two fundamental questions need to be addressed: **1) "how does one map healthy human grasps to a robotic prosthesis?"** and **2) "how does one implement dimensional reduction for actuation of the components of a prosthesis?"** The first question is addressed by first extracting the core kinematic/contact elements of grasps from the human grasp database and finding a rigid body tree structure that encapsulates those elements. For example, from the grasp characterization study, we have found that the kinematic and contact dynamic correlations of the thumb and index fingers are relatively low, inferring both fingers' functional independence in daily grasps. Such analyses are to be performed for efficient and reliable mapping of human grasps to robotic prostheses. The second fundamental question will be addressed by utilizing synergistic actuation of the individual joints—in terms of joint displacements and torques—to minimize the number of degrees of control. Combinations of the robotic digits' displacements are determined using the linear combinations of eigenvectors obtained from the dimensional reduction methods mentioned previously such as principal component analysis and linear discriminant analysis. The validity of the synthesized grasps formed from combinations of eigenvectors is verified using grasp classification of the synthesized grasps and comparison of the grasps' ergonomics and contact dynamics to the actual grasps.

3.3 Methods

Grasp data attained from human subject experiments in Chapter 2 have revealed the range of grasp and contact forces, grip aperture, and position and orientation of contact points required in daily grasping tasks. Roboticists have made efforts to quantify the quality of grasps by finding a correlation between stable grasps and the location of contact points on the object and the configuration of the hand [61][62][63]. Since the position and orientation of the contact points and the objects' center of mass can be determined from the electromagnetic trackers, the grasp matrix G can be easily determined for the evaluation of the hand-object Jacobian J_h, hence enabling some of the grasp quality measures minimum singular value of G, the volume of the grasp ellipsoid in wrench space, and the grasp isotropy index [61][64]. Other methods of determining the quality of grasps that require the geometric properties of the contact polygon may also be easily determined from the positions of the contact points from the EM trackers. Also, since the grasp quality takes a quasi-static approach, which works for some of the daily tasks, but not for others (like writing with a pen or throwing a ball), the forces and torques involved in dynamic tasks will be used as references to determine the power and torque requirements for developing prototypes of robotics prostheses.

3.3.1 Synthesis of reduced dimension grasps

Determining the control scheme of the robotic prosthesis, however, is a much more complicated task as there is a limited number of control signals an amputee can generate (via methods like electromyography or electroencephalogram) without inherence to the opposing healthy hand. Thus, a reduced dimensional dataset of combined kinetic and kinematic grasps is formed by extracting the principal eigenvectors generated by the LDA classifiers. By solving the eigenvalue problem from between-class covariance matrix Σ_B and within-class covariance matrix Σ_W obtained from the linear discriminant analysis, one can attain an m-by-m matrix V formed by columns of eigenvectors where m is the number of features used in LDA (in our case, m = 26 with 18 position features and 7 force features). The equation to this eigenvalue problem is given by:

$$\Sigma_B V = \Sigma_w V D \qquad (3.1)$$

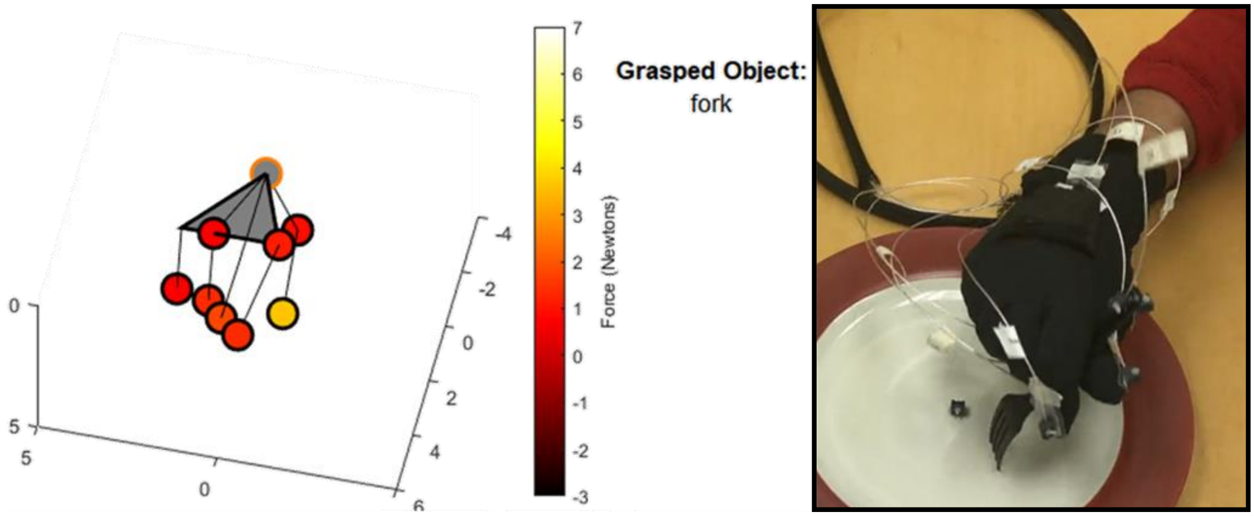

Figure 12: Grasp generation using the first four eigenvectors from LDA in descending scales of corresponding eigenvalues. The figure on the left shows a grasp of a fork synthesized from the principal eigenvectors, and the image on the right is the grasp pose formed by one of the subjects grasping a fork.

with *D* diagonal matrix of corresponding eigenvalues and *V* sorted in order of decreasing eigenvalues. The linear combination of the eigenvectors spans the spectrum of grasp poses that could be synthesized with data from 36 objects, where the grasp pose is computed from:

$$P = \sum_{i=1}^{n} a_i v_i \tag{3.2}$$

where *P* is the n-by-1 grasp pose with 26 position and force features and a_i is the scalar multiplier for the *i*-th eigenvector adjusted by the sliders (varied between -20 to 20). v_i is the *i*-th grasp eigenvector, termed the **eigengrasp**, and was first ideated by Ciocarlie et. al. for developing a low-dimensional method for modulating high-dimensional grasps [5]. To demonstrate this, a graphical interface was developed that uses the first four eigenvectors that account for 56% of total variance to generate daily grasps analogous to those formed by human subjects. By adjusting the sliders that act as multipliers to the principal eigenvectors, one could form a variety of grasp poses that

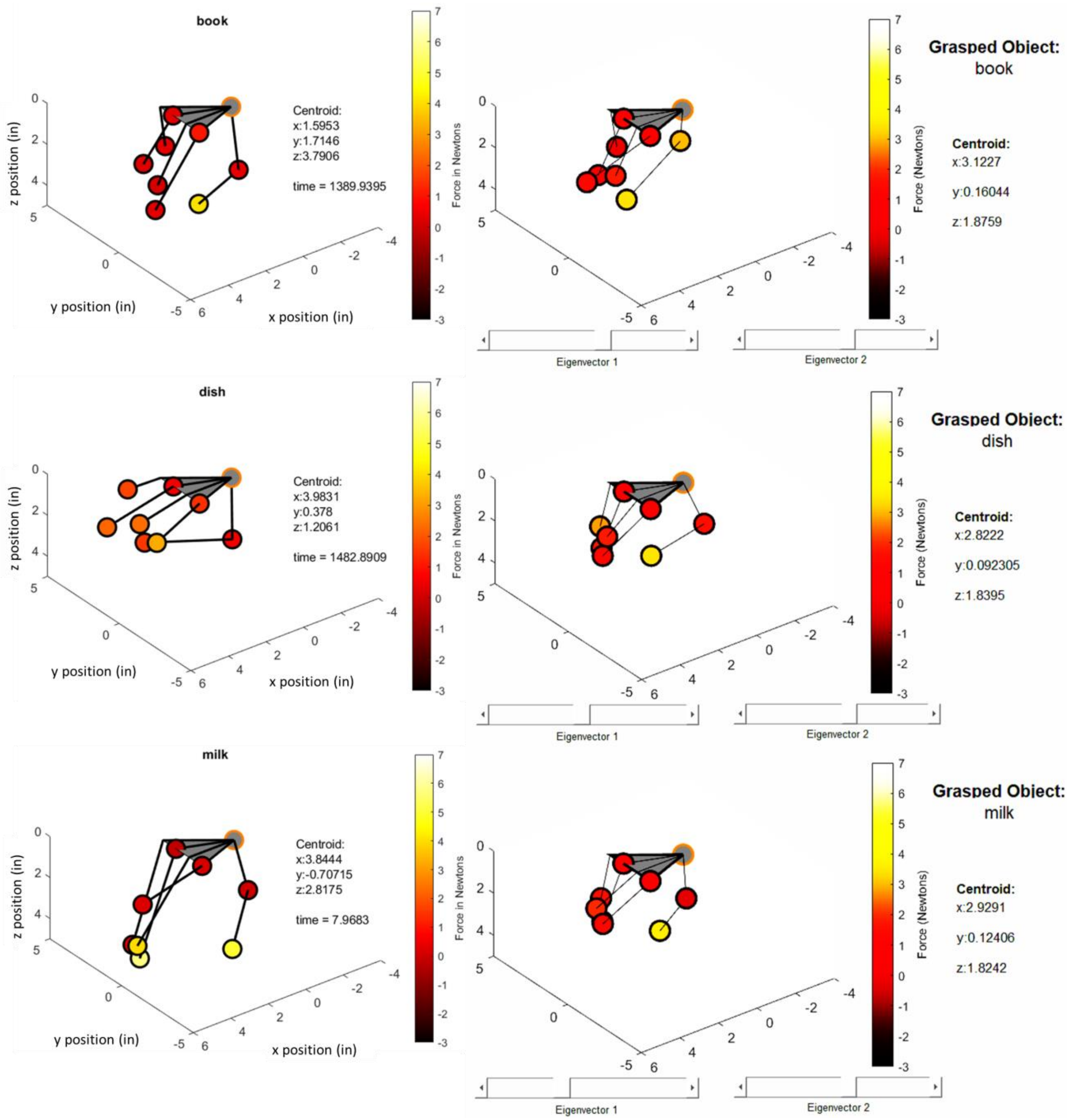

Figure 13: Examples of synthesized grasps from the graphical interface. Plots on the left show grasp poses formed by human subjects; plots on the right are synthesized grasp poses based on linear combinations of eigenvectors.

emulate the poses and contact forces of anthropomorphic grasps. Just like we have generated animations of grasp replicating tasks performed by human subjects, a skeletal representation of the hand would represent the grasp poses and color infills at the contact locations represent the contact force magnitudes as shown in Figures 12 and 13. The position and force features were also utilized to make a prediction for the closest type of grasp that the simulated grasp is trying to achieve. For example, the resemblance of the finger poses and the contact forces generated by the simulated grasp to the actual grasp of the fork can be seen in Figure 12. The thumb, index, and middle fingers are clustered more closely together than the other two fingers, and pressure output is significantly higher at the thumb; its resemblance can be seen in one of the subject studies where the subject also has the three fingers closely together, and the fork is in full contact with the thumb. More examples of the simulated grasps are shown in Figure 13.

Multiple synergy mapping strategies from the human hand to the robotic hand have been proposed; using the kinematic hand pose synergies proposed by Santello et. al. [20], three major mapping techniques have been used:

1. **Joint-to-joint mapping**: a one-to-one direct mapping of human joints to robot joints has been employed by Asada et. al. and Xu et. al. [65][66]. It is the simplest correspondence mapping method; however, this type of mapping only works for an anthropomorphic robotic hand.
2. **Cartesian mapping**: a mapping of human hand fingertips to robot fingertips has been employed by Ficuciello et. al. [67]. This type of mapping enables the mapping of synergies with dissimilar robot and human hand joints and configurations. However, the discrepancies in the contact dynamics are not negligible, and anthropomorphism is still required in terms of the number of digits.
3. **Object-based Mapping**: Gioioso et. al. have suggested the use of a virtual sphere placed on the human and robot hand where the kinematic and kinetic transformations and deformations of the sphere are transferred [4].

For our purposes, the object-based mapping is optimal for our combined kinematic/kinetic grasp study as: 1) we collected the position data at different positions at the hand, 2) we are interested in the contact dynamics of grasps, and 3) we want to develop prosthetic hand with dissimilar kinematic structures. Thus, we investigate the mapping of kinematic synergies of the human hand to the robotic hand as proposed and motivated by Gioioso et. al. Then, we will expand the analysis to incorporate dynamic synergies as discovered in our previous human subject study.

The kinematic mapping strategy as suggested by Gioioso et. al. can be summarized as the following:

1. Choose the initial configurations of human and robot hands.
2. Place reference points on the human hand to generate a virtual sphere.

$$\dot{p}_{ih} = \dot{o}_h + w_h \times (p_{ih} - o_h) + \dot{r}_h (p_{ih} - o_h) \tag{3.3}$$

where the sphere is parameterized with center o_h and radius r_h, with referent points at p_{ih}. By rearranging the equation above, we could attain:

$$\begin{bmatrix} \dot{o}_h \\ w_h \\ \dot{r}_h \end{bmatrix} = A_h^{\#} \dot{p}_h \tag{3.4}$$

where $A^{\#}$ is the pseudo-inverse of A, derived from the motion equation above. Combining with the synergy equation, we get:

$$\begin{bmatrix} \dot{o}_h \\ w_h \\ \dot{r}_h \end{bmatrix} = A_h^{\#} S_h \dot{z} \tag{3.5}$$

3. Use the virtual sphere to describe the kinematics and dynamics of the human hand.

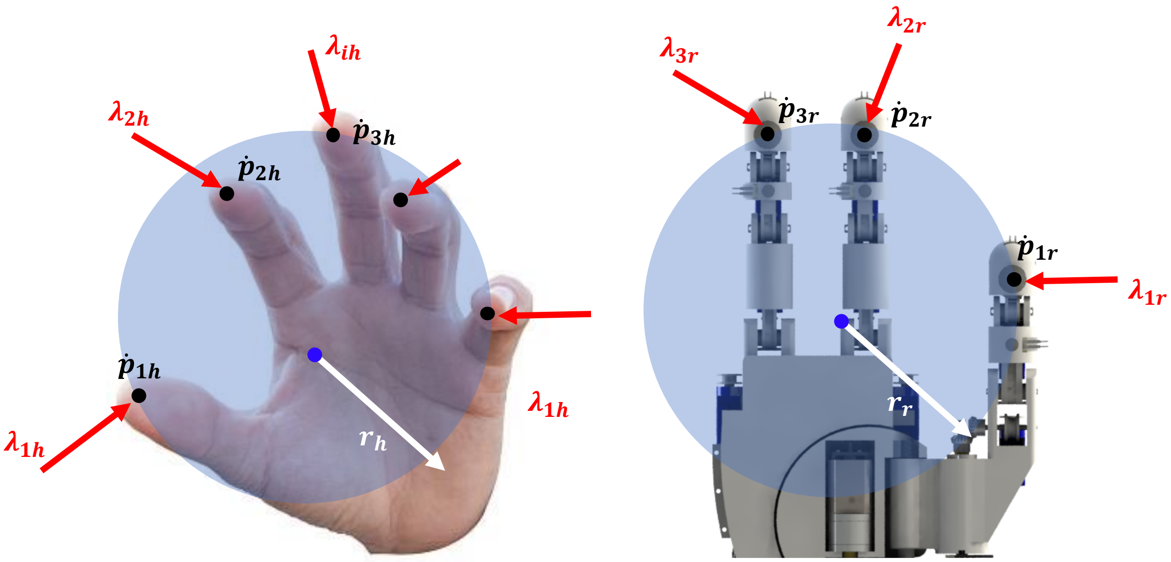

Figure 14: Visualization of the mapping method from **(left)** anthropomorphic grasps to **(right)** robotic grasps, inspired by the works of Gioioso et. al. The virtual sphere (blue circle) is estimated by computing the minimum bounding sphere of the reference points p. The normal contact forces $\boldsymbol{\lambda}$ are mapped with the synergy matrix $\boldsymbol{S_{fh}}$.

With the robot and the hand having different aperture sizes, the differences are scaled by a scaling factor

$$k_{sc} = \frac{r_r}{r_h} \tag{3.6}$$

Thus, a mapping of the spheres can be obtained:

$$\begin{bmatrix} \dot{o}_r \\ w_r \\ \dot{r}_r \end{bmatrix} = K_c \begin{bmatrix} \dot{o}_h \\ w_h \\ \dot{r}_h \end{bmatrix} \text{ with } K_c = \begin{bmatrix} k_{sc} I_{3,3} & O_{3,3} & O_{3,1} \\ O_{3,3} & I_{3,3} & O_{3,1} \\ O_{3,3} & O_{3,3} & 1 \end{bmatrix} \tag{3.7}$$

where the virtual sphere changes orientation & size independently of that of the human hand.

4. Set a new virtual sphere on the robot hand with its own reference points.

$$\dot{p}_r = A_r \begin{bmatrix} \dot{o}_r \\ w_r \\ \dot{r}_r \end{bmatrix} \tag{3.8}$$

5. Compute and apply the joint velocities of the robot using steps 1 to 4.

$$\dot{q}_r = J_r^{\#} A_r K_c A_h^{\#} S_h \dot{z} \tag{3.9}$$

By referring to the works by Gioioso et. al., we were able to develop a mapping method from the grasp data obtained from the human subject study to a robotic prosthesis with dissimilar form factors. We generated animations of three-fingered robotic grasping by transferring grasp data from all nine subjects.

Our next step to the three-fingered grasp generation is to apply the force synergies as attained from the human subject study. We can apply our combined synergy matrix

$$S_{ch} = \begin{bmatrix} S_{ph} \\ S_{fh} \end{bmatrix} \tag{3.10}$$

where S_{ph} is the kinematic/pose synergy and $S_{fh}$is dynamic/contact force synergy and compute the contact forces of the hand once the grasp reaches full contact with the object:

$$\begin{bmatrix} p_{ref} \\ \lambda_h \end{bmatrix} = S_{ch} z \tag{3.11}$$

where z is the hand synergy and λ_h is the set of normal contact forces on the virtual sphere. From our knowledge of dynamic analysis of a multi-fingered hand, we can compute the required joint torques to generate the external wrench applied to the virtual sphere, given by the set of equations:

$$W = -G_h\lambda_h = -G_r\lambda_r$$

$$\tau = {J_r}^T\lambda_r \tag{3.12}$$

$$\tau = {J_r}^T {G_r}^{\#} G_h S_{fh}\mathrm{z}$$

where G_h is the hand grasp matrix, G_r is the robot grasp matrix, and J_r is the robot Jacobian.

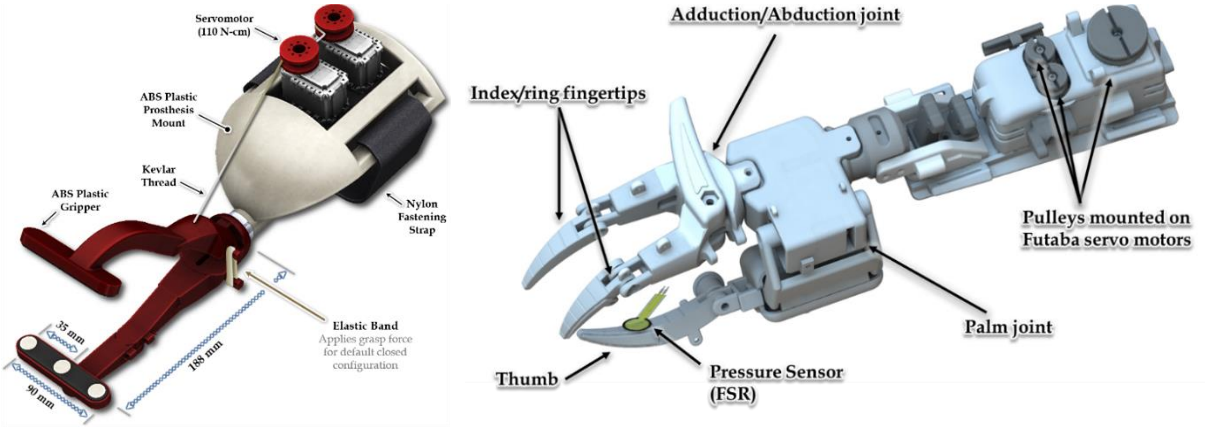

Figure 15: Preliminary designs of upper-limb prostheses/grippers. **(left)** two degrees of freedom gripper with two servo motors at the base controlling the gripper aperture and digit flexion inspired by the split hook prostheses in market. **(right)** Five degrees of freedom gripper with three servo motors at the base controlling the index and middle finger flexions and adduction, one at the palm joint controlling thumb adduction, and one at the base of the thumb controlling thumb flexion.

3.3.2 Computer-Aided Design of a Prosthetic Device

Our preliminary efforts to design and fabricate upper-limb prosthetic devices are arbitrary and rudimentary as our initial aims were to apply a reduced degree of freedom control on any generic robotic grippers. As such, we started with the most simplistic robotic gripper as shown in Figure 15, where two degrees of freedom control on the gripper aperture and digit flexion are employed. We have familiarized ourselves with the generic actuation methods and control schemes of typical robotic grippers at this stage; however, two degrees of freedom actuation is nowhere near sufficient for acquiring dexterous grasps required in activities of daily living as are the split hook devices in the market [37].

Subsequently, a modified design of the prosthetic device was proposed, employing a more anthropomorphic design gripper using three digits: thumb, index, and middle finger, that are controlled using 5 actuators (one each for the finger flexions, one for the index/middle adduction, and one for the thumb adduction) as shown in Figure 15. Again, we had not considered optimizing the design of the prosthetic device for the reduced dimension control scheme, making the design unfounded.

However, these designs are still not practical in terms of dexterity and modulation of contact forces. Thus, a similar design approach is taken, where seven actuators control the fingertip positions and orientations using routed Kevlar fiber threads to apply flexion motions. Modifications of the prosthesis design are primarily focused on:

1. **Enabling multi-joint fingers to allow broader workspaces.**
2. **Routing threads internally within fingers.**
3. **Applying torque control to align fingertip forces within the span of the eigenvectors for a reduced degree of freedom control.**

In addition to these modification goals, our new design of an upper-limb prosthesis is based on literature studies on physiological and psychological limitations on the use of prosthesis as well as our findings on grasp behaviors of subjects during ADL tasks. According to a study performed by Cordella et. al., the natural appearance of a prosthetic hand is a top priority for both passive and active prosthesis users, suggesting that a complete abandonment of anthropomorphism may not be desirable [2]. However, a reduced-anthropomorphic model may be desired to reduce the complexity of both design and control. We base our dimensional reduction method on our grasp study and studies performed by Santello et. al. and Starke et. al [20][28]. We have analyzed the correlation of fingertip poses and contact forces at different locations on the palm as shown in Figure 16, where Sample Pearson correlation coefficient matrices for the mean position of the fingertips and the mean forces at different locations of the hand for all subjects are computed and

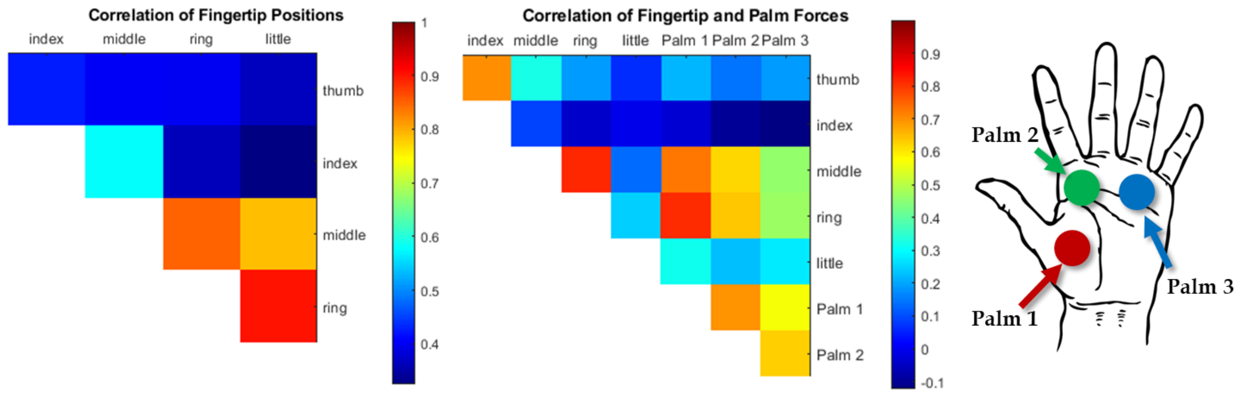

Figure 16: Correlation coefficient relationship between fingertips and positions on the palm. The figure on the left shows correlation pattern of the positions of the fingertips; the figure in the middle shows correlation patterns of forces between the fingertips and the palm, where the locations of palm 1, 2, and 3 are shown on the image on the right.

shown in heat colormaps. The correlation coefficient for a pair of features (i.e. thumb and index finger) equates to:

$$\rho_{x,y} = \frac{\sum_{i=1}^{N}(x_i-\bar{x})(y_i-\bar{y})}{\sqrt{\sum_{i=1}^{N}(x_i-\bar{x})^2\sum_{i=1}^{N}(y_i-\bar{y})^2}} \qquad (3.12)$$

given *N* data points for each feature and two distinct features, *x* and *y* are being compared for their correlation. Brighter colors on a grid of the heatmap of the matrix indicate higher correlations between the corresponding axes. It is notable that there are high correlations between the middle, ring, and little fingers compared to those between the thumb/index fingers and the other fingers, suggesting greater independence of motion of the thumb and the index finger.

The resulting correlation trend agrees with the aforementioned works with the following details:

1. The middle, ring, and little fingers have high position correlations with respect to each other.

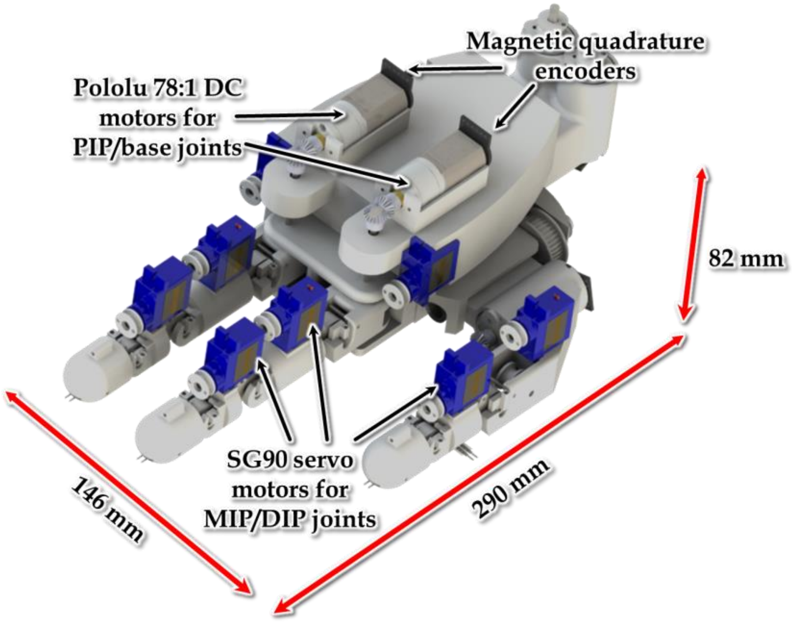

Figure 17: Semi-anthropomorphic three fingered robotic hand. Each finger has four degrees of motion, and each MCP and DIP joints are individually controlled using a servo motors.

2. The middle and ring finger have high force correlations vs. a relatively low correlation from the little finger.
3. The thumb and index fingers have low correlations throughout both pose and force correlations.

The first and second observations suggest that there may be low functional contributions from the little finger. In fact, a study performed by Puhaindran et. al. on the absence of flexor tendon in the little finger revealed no difference in the grip strength measurement [68]. A graph theory-based description of grasps have associated the little finger to be synchronous with the other fingers for all types of grasps [69]. The third observation suggests that the thumb and index fingers have high functional independence. Thus, a reduced digit model of the upper-limb prosthesis can be designed with the following criteria:

1. Includes the thumb with a functional resemblance to those of the anthropomorphic hand

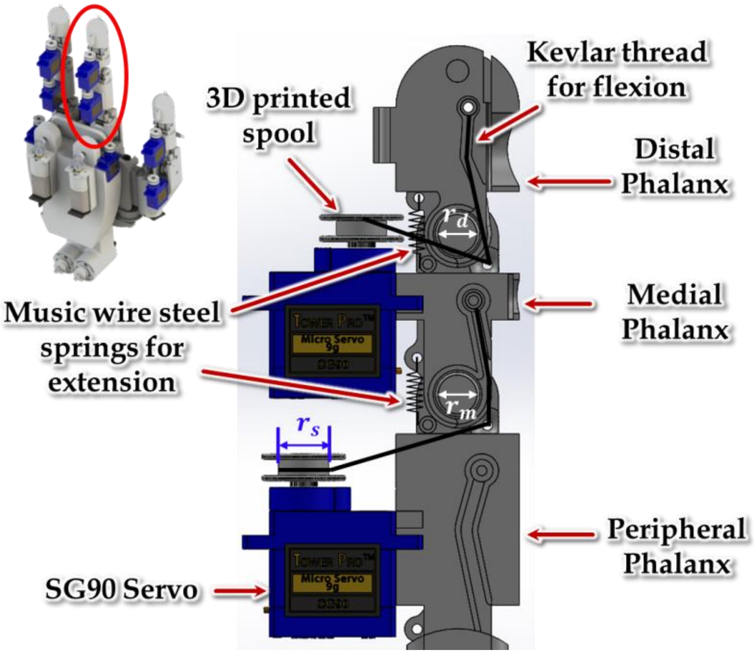

Figure 18: Actuation of PIP and DIP joints with the SG90 servo motors. Joints are flexed as the servo motors pull the linked Kevlar threads, extended passively by the spring forces from the music wire steel springs. Servo displacements and the joint displacements are related by $\boldsymbol{\theta_{medial}} = \mathbf{0.482}\boldsymbol{\theta_{sp}}$ and $\boldsymbol{\theta_{distal}} = \mathbf{0.448}\boldsymbol{\theta_{sp}}$, determined from the arc lengths formed by the phalanxes with radii $\boldsymbol{r_m} = 8.82$ mm and $\boldsymbol{r_d} = 10.09$ mm respectively.

2. Includes two fingers representing the index and middle/ring finger, with a high functional resemblance to that of the index, middle, and ring fingers
3. Full control of all joints can be accomplished, where they all move simultaneously along the span of each synergy eigenvector

Thus, we are able to develop a design of a semi-anthropomorphic upper-limb prosthesis as shown in Figure 17. The design has four degrees of motion for each finger including abduction and adduction of the metacarpophalangeal (MCP) joints, radial abduction and abduction of the thumb MCP joint, and flexion and extension of the interphalangeal (PIP and DIP) joints. Each finger geometry is designed based on the size and proportion of the average adult hand geometry as provided by the works of Buryanov and Kotiuk [70]. The design is first developed in a virtual setting so that we could generate realistic simulations of robotic grasping of daily objects using synergy-based motions.

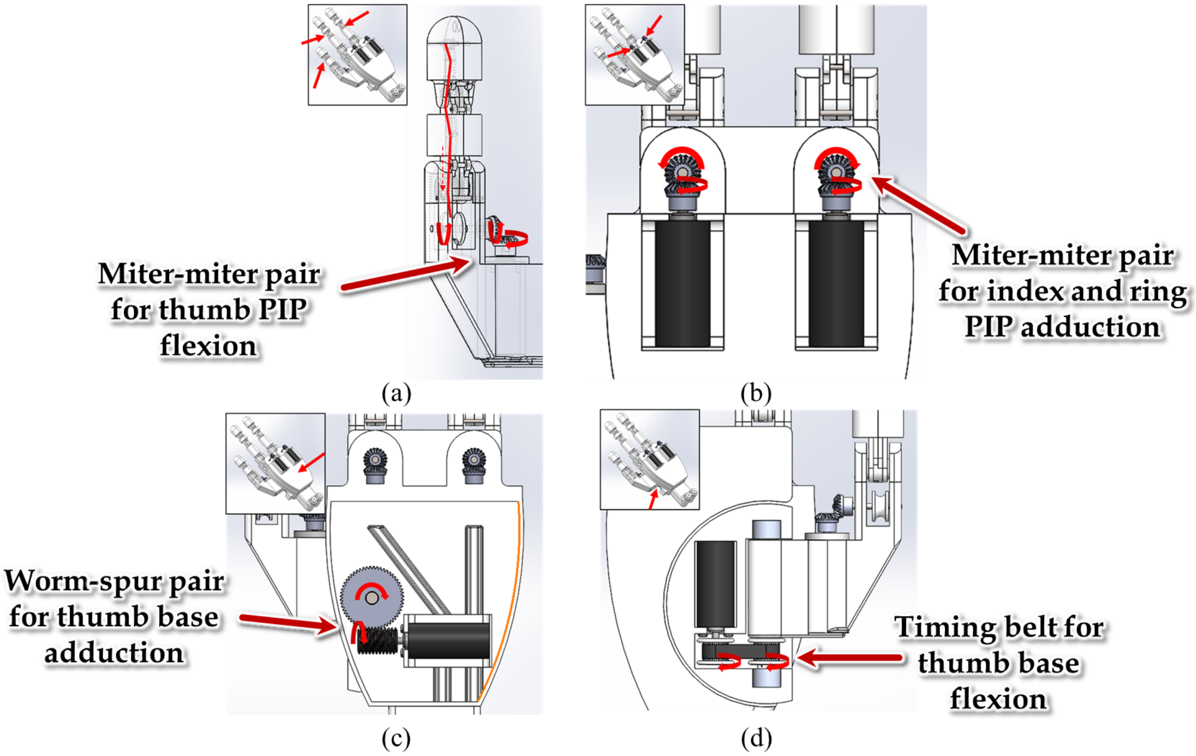

(a) (b) (c) (d)

Figure 19: Power transmission at multiple joints of the prosthetic hand. **(a,b)** The abduction and adduction motions at the base of the index and ring finger as well as the flexion and extension of the pip joint of the thumb require miter gear pairs. **(c)** For greater grip strength, power is transmitted by a worm-spur gear pair. **(d)** Timing belt and pulley combination is used for the adduction and abduction of the thumb's base joint.

3.3.3 System specification

The prosthetic hand's mechanical specification is primarily based on the kinematic and dynamic dataset that we have obtained from the human subject study. It has been observed that the average contact force between the trials was 3.15 N, and the maximum fingertip force applied was 40.63 N compared to the average maximum pinch force of 58-81 N based on literature [71]. Also, the average fingertip velocity was 39.62 mm/s, and the maximum fingertip velocity was 104.18 mm/s. The specifications require our motors to have the following specifications: nominal torque of 5.25 mN·m, maximum torque of 15.7 mN·m, nominal speed of 57 rpm, and a maximum speed of 150 rpm. For this reason, the Pololu 78:1 6V Metal Gearmotor was chosen as our main mode of actuation as it has a nominal torque of 74.53 mN·m and a stall torque of 432.49 mN·m. Its speed at maximum efficiency is 150 rpm, and its no-load speed is 180 rpm. Additionally, to minimize modes of control and power consumption, we actuate the PIP and DIP joints with the lower capacity SG90 servo motors as in Figure 18.

The power specifications of the prosthetic hand system require the ability to power seven total 6V DC motors with a nominal current pull of 0.63 A, which require power of at least 3.78 watts each. A total of five 5V SG90 servo motors actuate the interphalangeal joints, requiring a current draw of 250 mA each. Thus, the system requires a power supply that could provide 5.66 A and 10 watts. Thus, we have elected the SHNITPWR adjustable power supply that could provide a maximum of 10A and 120W. Also, four motor drivers are required to control seven total motors simultaneously, where two are stackable on top of one microcontroller. Each driver requires 8 digital pins and 2 analog pins, and the motors require 2 pins for the encoders and 1 pin for the pulse-width modulus (pwm) signal. A total of 51 digital pins and 8 analog pins are required for the entire system; thus, we use two Arduino Mega 2560 microcontroller boards that provide 54 digital pins and 16 analog pins each, having enough pins to power both motors controllers at the same time.

3.3.4 Fabrication of the semi-anthropomorphic prosthetic hand

The majority of materials used to fabricate and assemble the prosthetic hand are 3D printed using PLA filaments, aiding in the reduction of the total weight and cost of fabrication, from typical weight of prostheses in market of 800 to 900 grams to under 700 grams as are previously developed 3D printed prosthesis [72]. The phalanges are flexed using Kevlar threads as tendons wired to the spools mounted to the motors. Each phalanx is passively flexed with music wire steel extension springs with a load of 15.7 N and spring rate of 2.27 N/mm, sufficient enough to recover each phalanx to its passive position, but not as tense as to hinder the flexion motions. Miter gears are used in the adduction and abduction motions of the base of the index and ring fingers as optimal motor placement forces changes in the transmission direction as can be seen in Figure 19. The same applies to the extension and flexion at the base of the thumb, but worm-to-spur gear transmission is used as torque requirements are much greater at the base of the thumb. For the adduction and abduction of the thumb's base, a timing belt with two pulleys having different gear ratios is used to increase the output torque and resolution of the joint displacements. The total weight of the system is approximately 655.96 grams compared to 610 grams for the average hand weight of male adults, and the cost of fabrication is approximately $500 [73]. Considering that the average cost of myoelectric prostheses is $100,000, a low fabrication cost is a definite advantage of the proposed system [74].

3.3.5 Control and characterization of the semi-anthropomorphic prosthetic hand

As the grasp mapping method requires accurate positing of the Cartesian coordinates of the fingertips, building a robotic model that closely resembles the actual device is essential to the synergistic control of the prosthetic hand. As such, we have first characterized the Denavit–Hartenberg parameters, a.k.a. DH parameters, of the device by observing the geometric relationships between each joint in Solidworks. For ease of implementation of the inverse kinematics necessary for fingertip placement, MATLAB's rigid body tree model from the Robotics toolbox was used to build the robotic structure. The robot was modeled as a multi-body system with three sets of serial manipulators—the three fingers—branching off from the main body—the wrist. The DH parameters computed for each finger were used in the robotics model for the rigid body tree using a set fixed transform from the base of the device to each location of the joint using MATLAB's `setFixedTransfrom` function that takes each column (corresponding to the *i*-joint) of the DH parameters as input. The limits of each joint were chosen such that collisions are avoided,

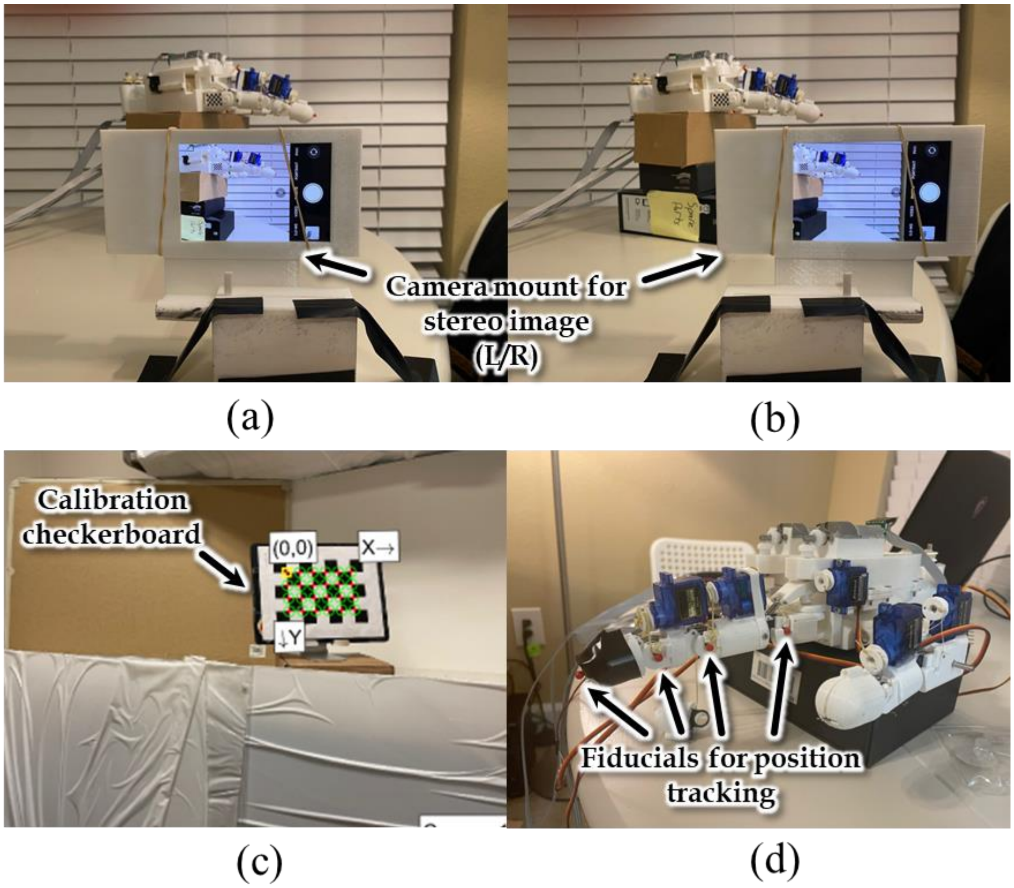

Figure 20: Stereo camera calibration system for parameter optimization of the prosthetic hand. Images on the top row **(a,b)** show locations of the camera on the left and the right respectively. **(c)** A black and white checkerboard image is used the calibrate the camera and the rail. **(d)** Red fiducials are placed on the points of interest on the prosthetic hand.

and motions lie within a reasonable range without causing damage to the structure. Inverse kinematics is also computed using MATLAB using the `inverseKinematics` function that takes in the rigid body tree model and the desired homogeneous transformation matrix (HTM) as inputs. The solver algorithm used was the Levenberg-Marquardt algorithm, which uses the damped-least squares method to approximate the joint configuration solutions. This algorithm is used as synergistic control requires real-time communication with the slave device, and fast computation is critical for our control method. The weights of the pose tolerances are 0's for the orientations and 1's for the XYZ coordinates as the orientations of the contact points are not critical in obtaining the desired grasp pose based on the virtual sphere method.

The accuracy of the model is improved using parameter calibration with a stereo camera system. Figure 20 shows the setup of the calibration system that is composed of a rail that moves the camera to two different positions for a stereo image, a black and white checkerboard to calibrate the camera, and red fiducial markers placed at multiple points of interest on the prosthetic hand. The stereo camera system was calibrated with MATLAB's Stereo Camera Calibration app, which requires 10 to 20 training images of the checkerboard to determine the camera parameters such as the fundamental matrix, rotation and translation of the second camera location, and radial and tangential distortions. To ensure the accuracy of the camera-based calibration system, the camera was calibrated such that the reprojection errors are less than 1 pixel. The 3D coordinates of the fiducials were determined using triangulation that uses the camera coordinates of the fiducial in the two stereo images and the translation and rotation matrices of the second location of the camera from the optical center of the first. To automate the process, the camera coordinates of the fiducials were found using red Gaussian filters and circular Hough transform to find the centers of the circular blobs. Transformation between the world coordinates of the fiducial points with respect to camera 1 to the hand coordinates with respect to the location of origin of the prosthetic hand (the wrist) is performed by attaching a 4-by-4 cm checkerboard piece parallel to the y-axis of the coordinate system of the prosthetic hand and computing the coordinate transformation using the following relation:

$$\begin{bmatrix} X \\ Y \\ Z \end{bmatrix}_{hand} = \begin{bmatrix} X \\ Y \\ Z \end{bmatrix}_{world} \times R_{HW} = \left(\begin{bmatrix} X \\ Y \\ Z \end{bmatrix}_{cam} - T_{WC} \right) {R_{WC}}^{-1} R_{HW} \tag{3.14}$$

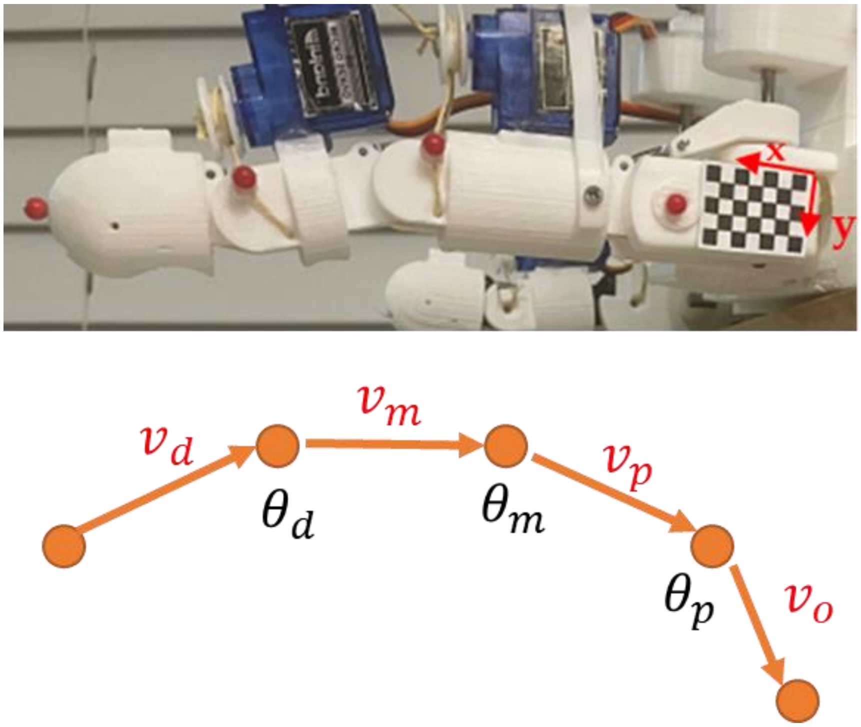

Figure 21: Four fiducial markers placed on the fingertip and dip, mip, and pip joints. A 4x4 cm checkerboard is placed at the base of the finger to reduce the analysis to 2D. The orange arrow denotes the vectors between the fiducial markers used to compute the joint angles.

where R_{WC} and T_{WC} is the rotation and translation from the camera coordinates to the world coordinates, and R_{HW} is the rotation from the world coordinates to the hand coordinates. The rotation and translation matrices can be found using MATLAB's `extrinsics` function that takes in the camera coordinates of the checkerboard and their corresponding 3D coordinates.

The first parameter to optimize was errors in the joint displacements between those commanded in the rigid body tree versus the actual joint angles formed by the device. Measurements of the abduction/adduction joints of the fingers were relatively simple to obtain as the base of angle measurement is stationary. For the PIP, MIP, and DIP joints, 3 or 4 fiducials (3 for the thumb, 4 for the index and ring finger) were placed at each joint and fingertip as shown in

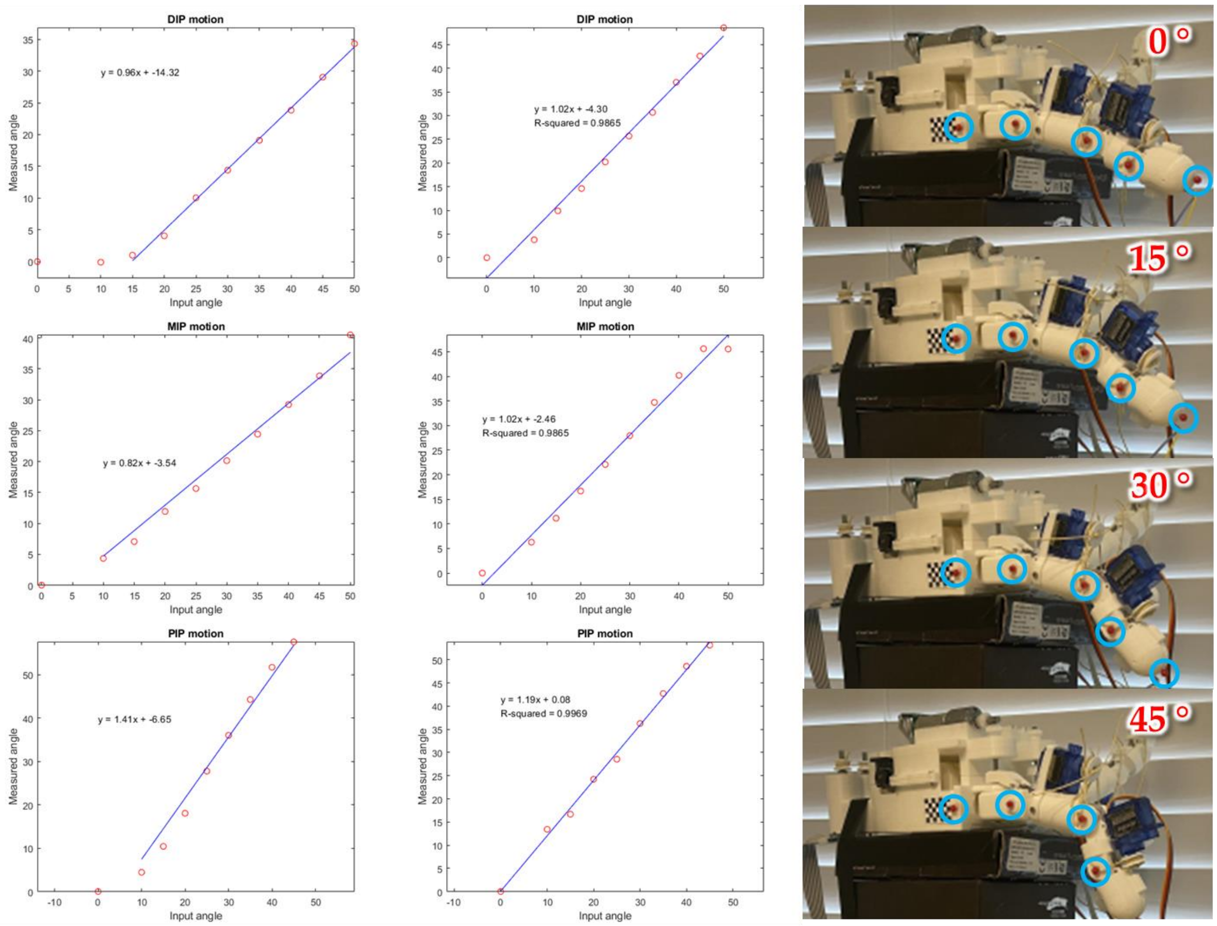

(a) (b)

Figure 22: Comparison of the joint angle mapping between the input and the measured. **(a)** Before the correction, the highly variant slopes and offset values suggest that the relations are not one-to-one. **(b)** After parameter adjustments, the offsets are much smaller and the $\boldsymbol{R^2}$ values are greater than 0.98. Frames taken during calibration of the MIP joint are shown on the right.

Figure 21, and the relative angles were measured by computing atan2 values between the vectors forms between the fiducial markers using the following equations:

$$\theta_d = atan2(v_{d,y} - v_{d,x}) - (v_{m,y} - v_{m,x})$$

$$\theta_m = atan2(v_{m,y} - v_{m,x}) - (v_{p,y} - v_{p,x}) \tag{3.15}$$

$$\theta_p = atan2(v_{p,y} - v_{p,x}) - (v_{o,y} - v_{o,x})$$

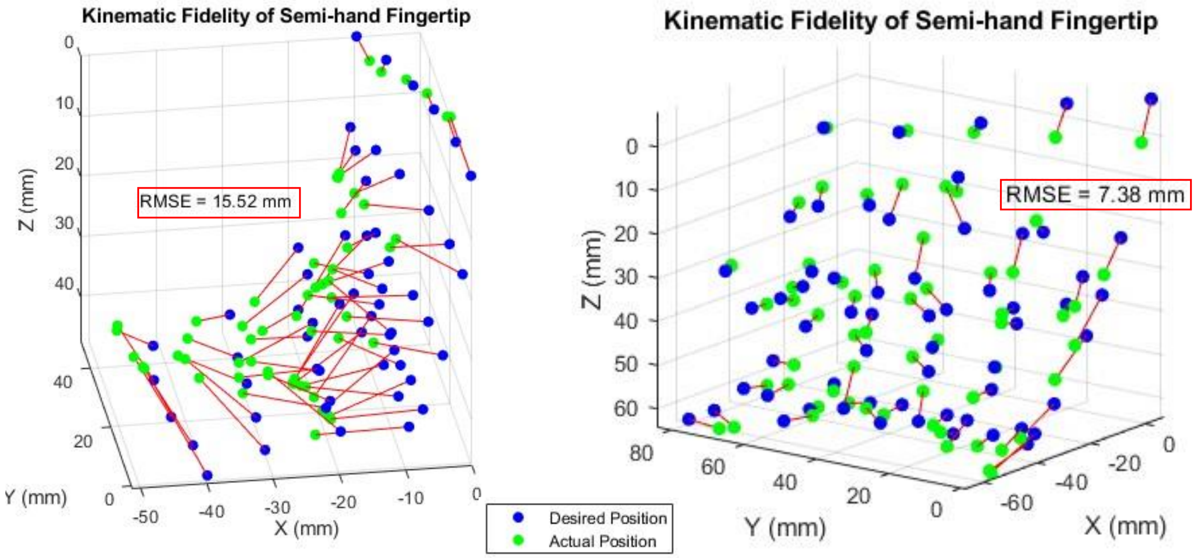

Figure 23: Comparison of the position mapping between the input and the measured. **(left)** Position mapping at the first iterations yields a root mean square error of 15.52 mm. **(right)** Position mapping at the first iterations yields a root mean square error of 7.38 mm a reduction of 52.4%.

where the subscripts *d*, *m*, *p*, and *o* denote the location of the fiducial markers of joints with *o* being the base of the finger, and *v* represents the vectors formed. As expected, we did not observe a one-to-one mapping between the input and the measured joint angles; thus, parameter adjustments were made to ensure a one-to-one mapping. The joint angle calibration steps were repeated four more times until a reliable, linear mapping was observed as in Figure 22.

After correcting the joint angle scaling, the only remaining source of error that can be minimized is the modeling parameter or the DH parameter. As such, an optimization problem was designed such that the error between the commanded and the measured Cartesian coordinates of the fingertips is minimized while using the DH parameters as adjustable inputs to the cost function. The optimization problem statement is as follows:

$$\text{Objective function: } \underset{DH'}{\min} E = \sum_{j=1}^{k}\left(\left|X_j - X_j'(DH')\right|\right)$$

$$\text{Constraint: } |DH' - DH| \leq e_d$$

where X_j is the measured coordinates of the fingertip, X'_j is the computed coordinates of the fingertip, DH is the 4-by-4 set (four joints per finger and four parameters) of previous parameters, DH' is the modified DH parameter, and e_d is the matrix of allowed deviations. MATLAB's `fmincon` function was used to compute the local minimum—where it uses the finite differences to approximate the Hessian—and it takes in the objective function and the constraints as inputs. The optimization strategy was implemented by capturing images of the prosthetic hand at 50 different points scattered within the workspace for each finger. Prior to optimization, a root mean square of the errors was greater than 18 mm. After repeating the trials for six total iterations, a root mean square error of 7.38 mm was achieved—a reduction of 52.4% from the first iteration at 15.52 mm as shown in Figure 23. Further iterations did not yield a meaningful reduction in the positional errors.

CHAPTER 4

SIMULATED EVALUATION OF TASK PERFORMANCE OF DATA-DRIVEN PROSTHESIS

4.1 Introduction

The design performance of the data-driven upper-limb prosthesis for accomplishing synergy-based grasps is first evaluated with a physics-based robotic simulation platform—CoppeliaSim. Before the dedication of extensive resources into developing the actual prototype, a validation that the reduced-dimension robotic hand can attain daily grasps with functionality close to that of the human hand was attained with relative ease with a virtual testing platform. By applying the combined grasp synergy to control the joint configurations of the hand and fingertip forces, we demonstrate the establishment of stable grasps with the proposed design of the prosthetic hand in a virtual setting.

After validating the formation of stable grasps with the simulation, we have built and assembled the prototype of our design and applied the forward/inverse kinematics to control the joint positions as well as a strategy to vary the fingertip forces of each digit with synergistic torque modulation. Then, similar synergy-based grasps were formed with the combination of eigengrasps as we've established in previous studies and have analyzed the stability of robotic grasps. The performances of grasps were measured with the grasp quality metrics and were compared to grasps in simulation and those from actual grasps from human subject studies.

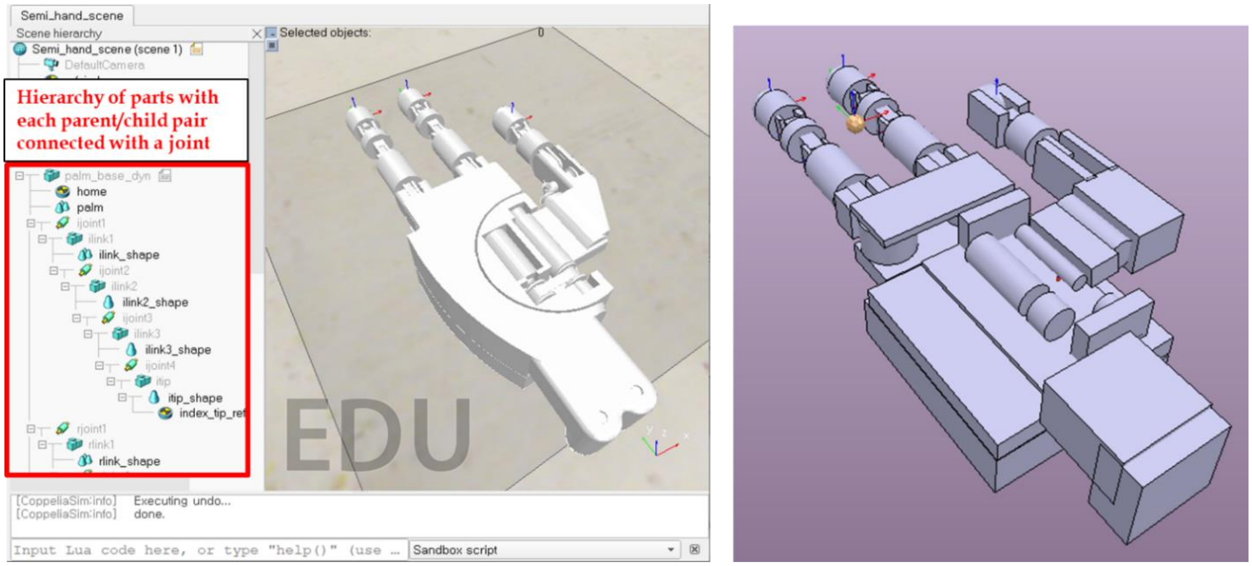

```
[CoppeliaSim:info]   Executing undo...
[CoppeliaSim:info]   done.
```

Figure 24: Importation of robotic structure from prototype design into CoppeliaSim. Left shows the robot hierchery with each parent/child pair connected with a joint. Right shows the simplified geometric representation of the robot parts to improve accuracy of dynamic simulation

4.2 Methods

4.2.1 Implementation of prosthetic hand model in CoppeliaSim

We chose to utilize the CoppeliaSim robotics simulation software developed by Coppelia Robotics, as it is reputed for having a fully integrated robotics API, allowing for fast prototyping and hardware control and allows users to choose between four physics engines: Bullet Physics, ODE, Newton, and Vortex Dynamics, where we utilize Newton Dynamics for a realistic simulation of rigid body motion and contact modeling [75]. While CoppeliaSim is a powerful simulator for robotic applications, it does provide adequate tools for algebraic computations, thus we utilize its remote API for broadcasting variables between MATLAB and itself. The first task in utilizing CoppeliaSim was to build a robotic architecture from the prototype design models (STL) that we have developed with a 3D CAD software, Solidworks. This involved placing robotic objects in

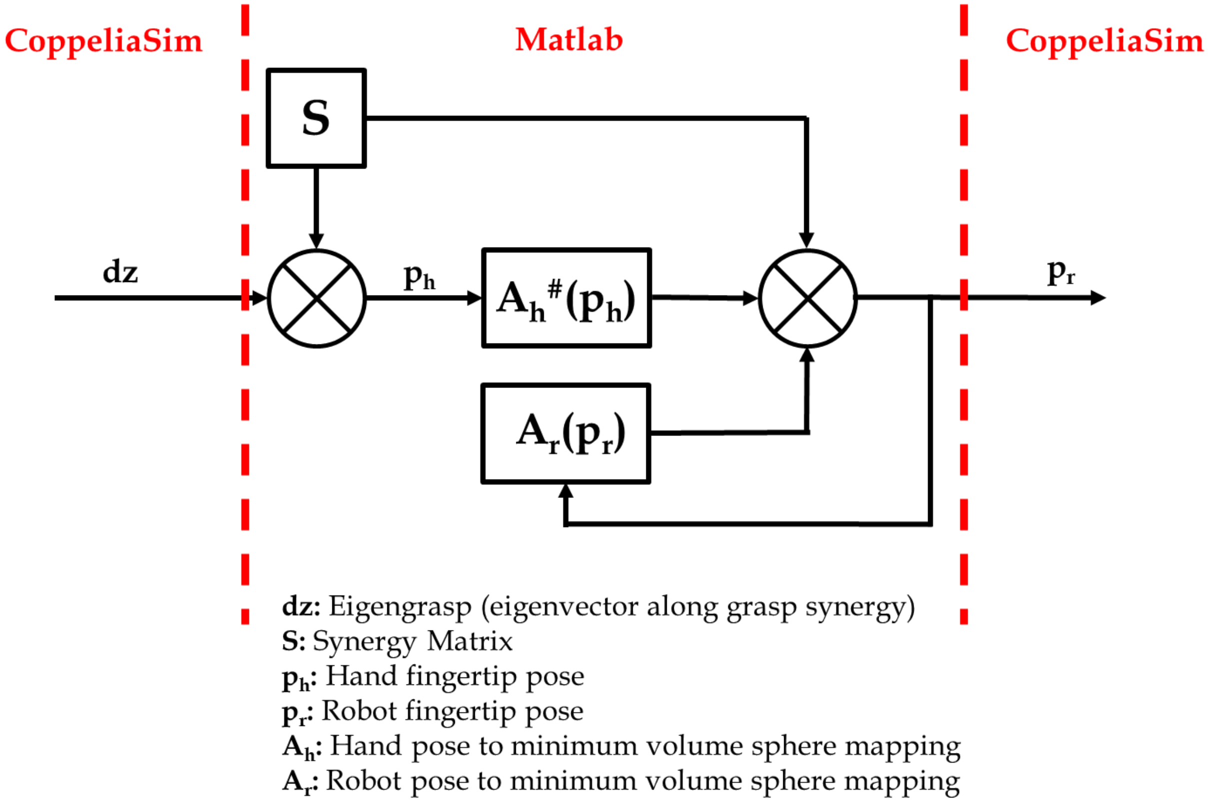

Figure 25: Block diagram of variable input from CoppeliaSim to pose generator in Matlab. The robot pose and virtual hand pose are updated in real-time to compute the virtual spheres form by the two to compute the new desired pose.

hierarchical structure from base to tip, orienting virtual joints and setting the correct joint limits, creating dynamic boundaries of objects for contact modeling, and creating kinematic loops for each kinematic chain for inverse kinematics. Successful importation of the robotic structure to CoppeliaSim can be found in Figure 24. Once this is established, we have access to fully kinematic control of the fingertips within the boundaries of its workspace.

4.2.2 Control loop between CoppeliaSim and MATLAB

Although CoppeliaSim is a tool for physics-based simulation, it does not have a well-established data storage and processing platform, thus, data such as eigengrasp combination, joint position, and Jacobian matrices were broadcasted from CoppeliaSim to Matlab as shown in Figure 25. Then, as established in Equation 3.9, the product of the synergy matrix and the eigengrasp combination

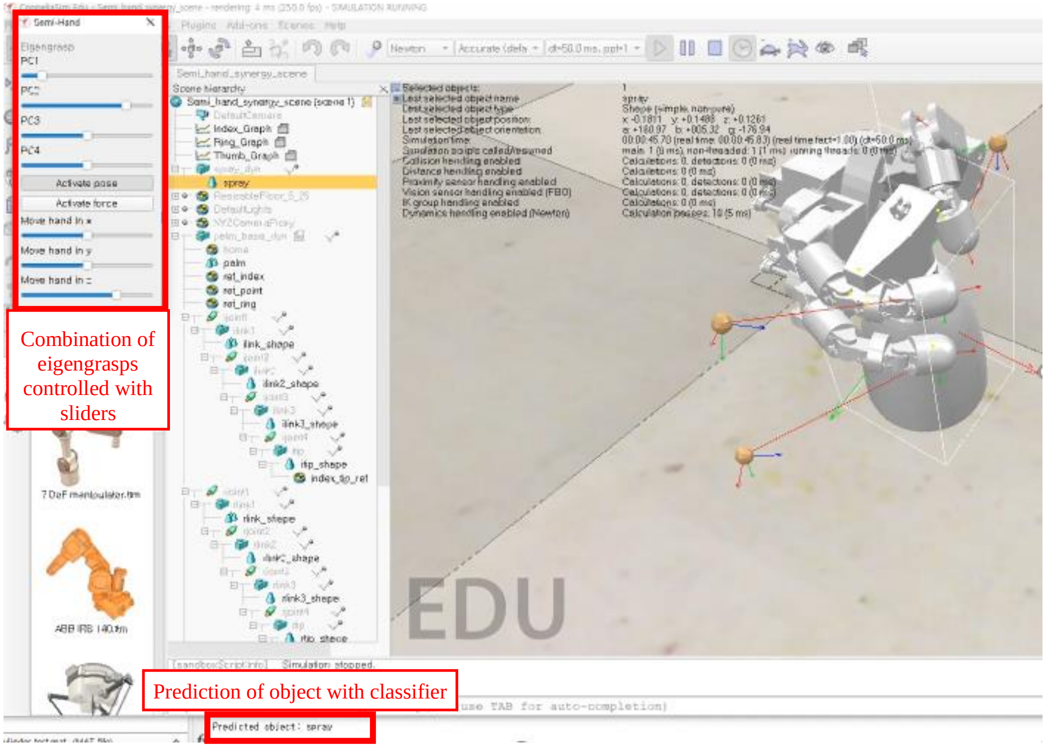

Combination of eigengrasps controlled with sliders

Prediction of object with classifier

```
Predicted object: spray
```

Figure 26: Robotic hand forms a grasp that corresponds to the eigengrasp combination for grasping a spray bottle. The formulated grasp is maintained while holding the spray bottle above ground.

yields the hypothetical configuration of the human hand, which then is used to compute the corresponding robot fingertip configuration. Then, the desired robot configuration is broadcasted back to CoppeliaSim, completing the loop of Matlab/CoppeliaSim. Communication.

The closed-loop system allows us to generate myriads of robotic grasps as we vary the scales of each eigengrasp element using sliders as shown in Figure 26. As the robotic hand changes its pose that corresponds to the eigengrasp set with the sliders, our classifier previously built-in Matlab predicts the type of object being held by the robotic hand for a given set of eigengrasps. This allows us to explore multiple combinations of eigengrasps with the knowledge as to the types of grasps the hand is trying to achieve. This is especially powerful when we compare the grasps being achieved by the robot to the grasps formed by the human subjects during the experiments.

4.2.3 Contact force modulation with joint torque control of prosthetic hand

To implement the contact force synergies of grasps, we utilized CoppeliaSim's contact modeling API to attain the positions of all points of contact that are of interest. To validate the force measurements taken by CoppeliaSim, we designed a virtual experiment where the robotic hand grasps and lifts a uniform cylinder with varying masses. In theory, the magnitude of the weight of the cylinder should be equivalent to the sum of all contact forces exerted by the hand in the vertical direction. As such, the virtual experiment involved varying the surface friction quality from 0 to 2 (arbitrary values where 0 is completely slippery and 2 has no slippage) and the weight of the cylinder from 100g to 1kg in the range where grasp failure due to slippage did not occur. Measurements of the contact forces for each trial were taken for 60 seconds. The results comparing the sum of contact forces to the weight of the cylinder are plotted in a 3D surface plot in Figure 27. The plot suggests that the CoppeliaSim has high fidelity estimates of the contact forces as the root mean square error of the sum of contact forces is 1.343×10^{-3} N (0.000575% error on average) for both sums of contact points on the cylinder and that on the robotic hand.

For the application of the grasp pose synergy, we have implemented Jacobian-based velocity control of joints to attain the desired joint configurations. This involved the simple computation of the pseudo-inverse of the robot Jacobian using the least-damped squares method to compute the desired joint velocity for a given robot tip pose error:

$$\dot{\theta} = J_r^{\#}(p_{r,des} - p_r) \tag{4.1}$$

where $p_{r,des} = A_r K_c A_h^{\#} S_h \dot{z}$, attained in Equation 3.11. The desired tip poses are computed with the set of equations 3.3 to 3.9 in the workflow shown in Figure 25. As the robot hand comes into contact with the object of interest, the contact forces are measured as verified with the cylinder

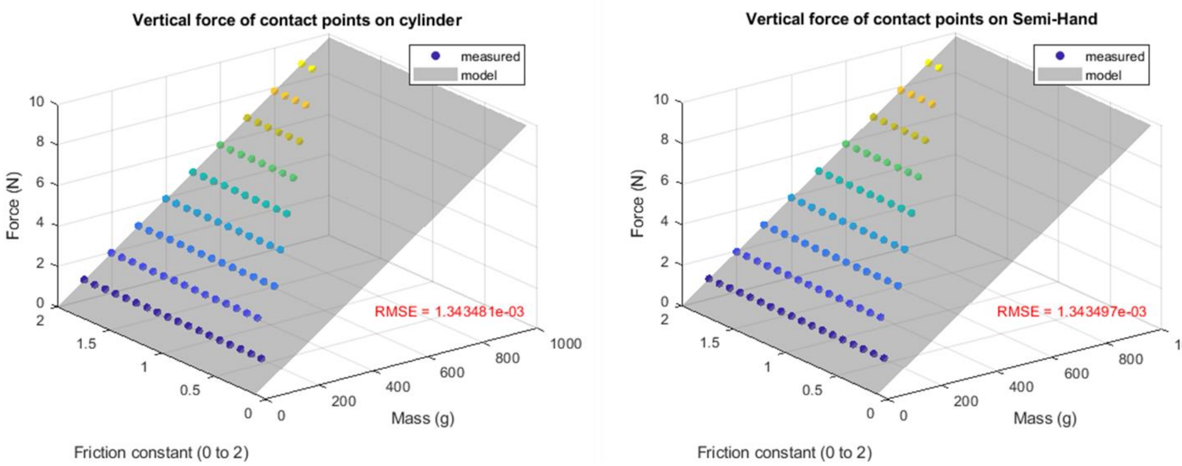

Figure 27: Validation of contact force estimates on the prosthetic hand by Coppeliasim. **(left)** The net contact forces in the vertical axis exerted on the cylinder is compared to the gravitational force due to weight, and a resulting $\mathbf{1.34 \times 10^{-3}}$ N RMSE is observed. **(right)** Similar analysis is performed on the net reaction forces acting on the prosthetic hand, and a resulting $\mathbf{1.34 \times 10^{-3}}$ N RMSE is observed.

experiment after the desired pose is determined. We reference the desired contact forces from our grasp database for a given eigengrasp combination. From Coppeliasim's contact force modeling, we can determine the normal forces applied to each point of interest ($f_{n,i}$) of the robotic hand. To attain the desired contact force, we apply torque control of the robot fingers with the following equations:

$$e_{P,i} = f_{des,i} - f_{n,i}$$

$$e_{I,i} = \sum_{i=0}^{N} e_{t-i}$$

$$e_{D,i} = e_t - e_{t-i} \tag{4.2}$$

$$U_i = K_P e_{P,i} + K_D e_{D,i} + K_D e_{D,i}$$

$$\Delta\tau = {J_r}^T {G_r}^{\#} G_h U_i$$

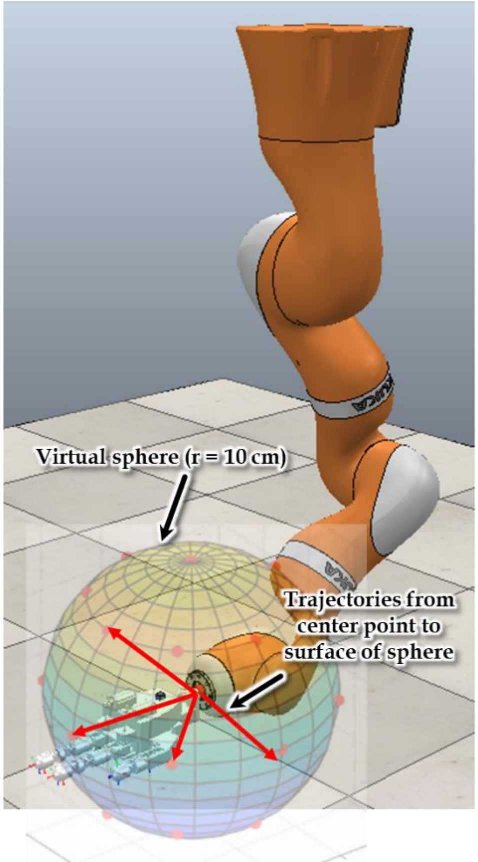

Figure 28: Semi-anthropomorphic prosthetic hand mounted at the tip of KUKA IIWA 14 end-effector. Trajectories starting from the center of the sphere and to the points on the outer surface of the sphere are generated.

where $f_{des,i} = S_{fh}\text{z}$ is attained in Equation 3.12. These equations allow us to determine the modifications to the joint configurations to maintain the force output from the robotic hand at the desired levels.

4.3 Experimental Setup

4.3.1 Problem statement

We aim to test the previously mentioned hypothesis on improving stability and robustness of grasps with the augmentation of synergistic contact force modulation to the synergic grasp poses. Thus, as a proof of concept, a set of experimental tasks was designed within the

CoppeliaSim/MATLAB environment. We compare the proposed method to previous works by varying the strategy for modulating output joint torques. In previous works, for example, the synergy-based three-fingered robotic hands developed by Grioli et. al. or Chen et. al., are very effective in forming a stable grasp given a design grasp configuration; however, there are none to our knowledge that explores the stability/robustness of synergistic grasps with consistent perturbations to the grasps [76][77]. Thus, the experiment explores two hypothetic situations where both apply synergistic grasp poses to grasp various objects, one applies non-strategic uniform torques over the joints responsible for maintaining the grasp forces, and the other applies a contact force synergy-based torque distribution over the control joints. We only control the flexion and extension of the proximal interphalangeal (pip) joints of the index and ring fingers and the first two joints of the thumb for torque modulation for simplification for contact force modeling as with the previous works with underactuated robotic hands [78][79][80]. In these experiments, the prosthetic hand grasps a subset of daily objects characterized by the human subject experiments in Chapter 2, and the prosthetic hand and the held object undergo a set of linear perturbations. In theory, superior grasps have better grasp robustness when the object is less prone to failure from different combinations of external forces, which is also experimentally measurable by applying a set of perturbation sequences to robotic grasp and measuring the duration of grasps sustained within a trial [81][82][83][84]. Grasps have higher stability when the magnitudes of relative acceleration of the held object with respect to the hand are lower [85][86][87]. Grasp duration for a single trial is computed by taking the ratio between the duration that a successful grasp is maintained and the duration of an entire trial. To measure the grasp stability, we attach a pair of virtual accelerometers, one on the wrist of the prosthetic and the other on the held object.

4.3.2 Experimental method

The following summarize the logistics of the experimental setup:

Objective: To experimentally verify that the addition of a synergy-base force control of the prosthetic hand enhances grasp stability and robustness

Method: Two methods of modulating joint torques are compared: 1) non-methodical, uniform distribution of joint torques, and 2) contact force synergy-based modulation of joint torques. For a fair comparison, the net torques applied by the two methods are equal with the following relation:

$$\sum_{i}^{n} \tau = n\tau_j \tag{4.3}$$

Where τ_i: synergy − based torques $(\tau = {J_r}^T {G_r}^{\#} G_h S_{fh} \mathrm{z})$

τ_j: uniformly applied torques $(\tau_{j,1} = \tau_{j,2} = \tau_{j,3} = \cdots)$

Procedure: The prosthetic hand is attached to the KUKA IIWA 14, a serial manipulator available in the Adaptive Robotic Manipulation Laboratory, and is exposed to motion between the starting position and 32 different points that surround it in a sphere. The KUKA arm starts from the center of the sphere, moves to one of the points on the surface of the sphere, returns back to the center, and repeats the process until all the points have been reached. The hand grasps each object with the eigengrasp set of grasp poses associated with each object. Once the grasp pose is applied and is in contact with the object, the fingers close in on the objects with one of the two following methods: 1) synergy-based force

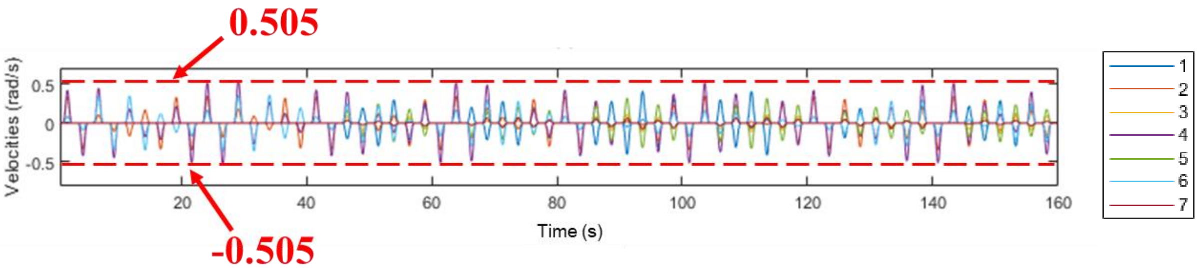

Figure 29: Joint trajectory profile of the KUKA serial manipulator for generating the perturbation motions for the simulated experiment as shown in Figure 28. The maximum joint velocity for any joint does not exceed ±0.505 rad/s, resulting in an average end-effector velocity of 40 mm/s.

control and 2) non-methodical, uniform closure. For comparison for grasps with a spectrum of net torques, the joint torques are distributed from a net torque of

$$c\sum_{i}^{n}\tau = cn\tau_j \tag{4.4}$$

where c is a torque multiplier from 0.1 to 1 in 0.1 increments. The joint torques from the synergistic method are determined by the results from equation 3.12 multiplied by the torque multiplier c. The expected change for varying c is an increase in grasp stability/robustness.

4.3.3 Grasp perturbation trajectory

The points along the perturbation trajectories were generated using spherical coordinates about a designated sphere's center. A radius of 100 mm was chosen to follow similar protocols to previous works involving experiments using perturbations to robotic grippers, ranging from 50 to 100 mm [88][89]. For each spherical axis, an increment of 45° within an interval from 0 to 90° was chosen to generate the objective points, resulting in 32 different points total. This results in an average of 40 mm/s per path from the center of the sphere to the surface. The joint trajectory profile for generating the planned paths can be seen in Figure 29, where the maximum joint velocities do not exceed 0.51 rad/s. Such trajectory was chosen based on previous works that have performed experiments on grasp stability and adjustability using induced perturbations. A study on slip and grip force on prosthetic grasp by Damian et. al. chose velocity profiles of objects ranging between 10 mm/s to 50 mm/s [90]. Naceri et. al. have investigated the responses of human participants' grasps to object force and torques perturbations, and the position-time response of held object provided in the study shows velocity profiles of approximately 15 to 30 mm/s [91]. A study on the control of prosthetic hand grasp and slip prevention uses velocity profiles of range 20-40 mm/s [92]. As such, the values chosen for the trajectory profiles are acceptable as they lie in the proximity of the values adopted in previous works.

4.3.4 Grasp modulation protocols

The following were observed for each perturbation trial to ensure repeatability and consistency:

1. The prosthetic hand starts at a default pose configuration p_0 using the mean of the class means μ_k to ensure as much span as possible along the synergy matrix [93][94][95]. The pose formed by the mean of class means is classified as the cubic prism using the LDA learner identified in Chapter 2. The initial joint configuration q_0 is computed using CoppeliaSim's inverse kinematics module, and the corresponding eigengrasp z_0 is computed with Equation 3.11. They are used as base values before applying changes Δz for the different types of objects.

3. The object class name (e.g. spray bottle) is prompted to MATLAB, which then computes

$$\Delta z_i = S^{-1}\mu_i - z_0 \tag{4.5}$$

where μ_i is the mean pose configuration of object i and Δz_i corresponds to the change in eigengrasp to be applied to the prosthetic hand for object i. Simultaneously, the corresponding object is placed within the hand's grasp in CoppeliaSim, where its coordinates and orientations are chosen from the grasp dataset.

4. The joint configurations and the fingertip coordinates of the prosthetic hand are broadcasted from CoppeliaSim to MATLAB for computing A_r, where the radius and center of the sphere are computed by approximating the minimum bounding sphere with the three coordinates of the fingertips and the two fixed contact points at the palm. Details on the computation method for finding the minimum bounding sphere can be found by the works of J. Ritter [96]. The virtual sphere for the hand kinematics A_h is computed using the mean fingertip coordinates μ_i for object i from the grasp database.

5. The updated pose is computed using a modified version of Equation 3.11; for implementation on a discrete system, we use:

$$\Delta q_r = J_r^{\#} A_r K_c A_h^{\#} S_h \Delta z \tag{4.6}$$

where $A_h^{\#}$ is computed with Moore-Penrose pseudoinverse

$$A_h^{\#} = (A_h^T A_h)^{-1} A_h^T \tag{4.7}$$

and where $J_r^{\#}$ is computed with the damped least square method to avoid singularities and smoothing trajectories

$$J_r^{\#} = (J_r^T J_r + \lambda^2 I)^{-1} J_r^T \tag{4.8}$$

with the damping factor $\lambda = 0.1$ computed empirically. The desired joint configuration is updated to $q_r = q_0 + \Delta q$ and is broadcasted back to CoppeliaSim. This results in the prosthetic hand closing its grip on the object; however, the world dynamics are not enabled at this point, and the pose is maintained for 20 seconds for motion stabilization.

6. After motion stabilization, torque control is enabled by applying the method as discussed in Chapter 2 and Equation 3.12. Individual joint torques are distributed with two different methods as articulated in the previously mentioned procedure and equation 4.4. The grasp matrices G_h and G_r are computed with the fingertip coordinates from the grasp database and those of the prosthetic hand, and both share the coordinates of the object center from the grasp dataset. Orientations of

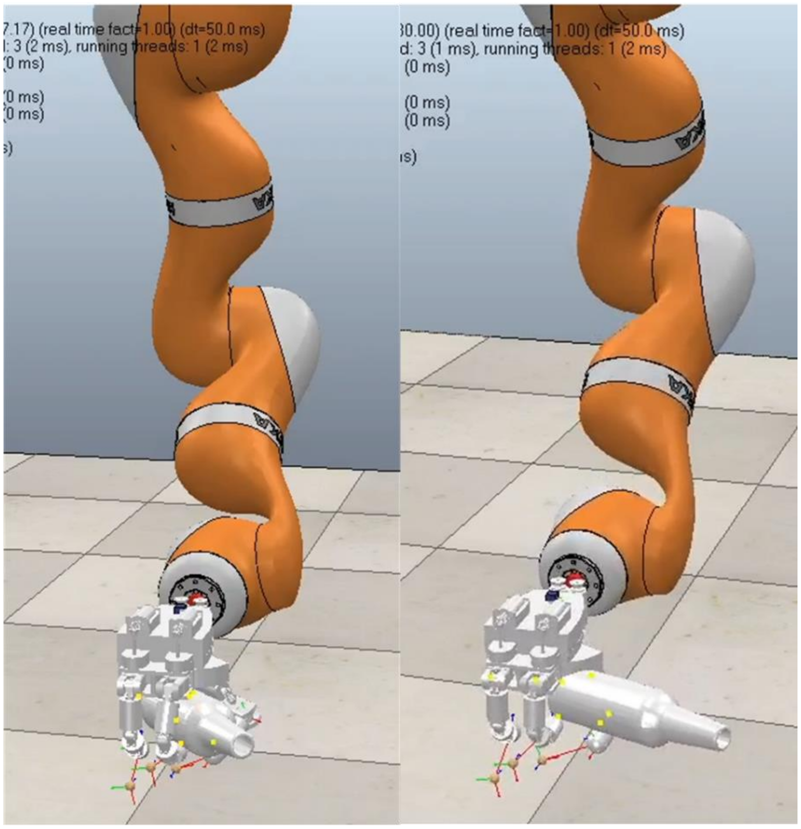
(a) (b)

Figure 30: An experimental trial of grasping a glass bottle. **(a)** For one trial with the force synergy-enabled grasp (t = 86 s), grasp is maintained relatively well. **(b)** For one trial without the synergistic torque control, the glass bottle starts to slip out of grasp at the same grasp duration (t = 86 s)

the contact points are all set to be orthogonal to the surfaces of the fingertips as our dataset is confined to the normal forces only. The procedures for computing the grasp matrices are relatively straightforward with these inputs using the computation method first introduced by Prattichizzo et. al. [97]. After the target joint torques τ_i are set, the motions that accompany the desired torque are designated such that the contact points reach towards the centroid of all contact points. Torque levels are maintained using a manually tuned PID controller. After all the joints are set to motion, world dynamics are enabled, and grasp is maintained for 20 seconds before the last phase.

7. The perturbation trajectory is enabled for the rest of the trial. Processes from 1 to 6 are repeated for each torque multiplier from 0.1 to 1 for each method of torque modulation. The acceleration

magnitudes from each accelerometer are archived to separate Excel files for each multiplier. All the processes are automated including object selection, object placement, variation of torque multipliers, and choice of torque modulation method to eliminate trial-to-trial variation and intervention from the observer.

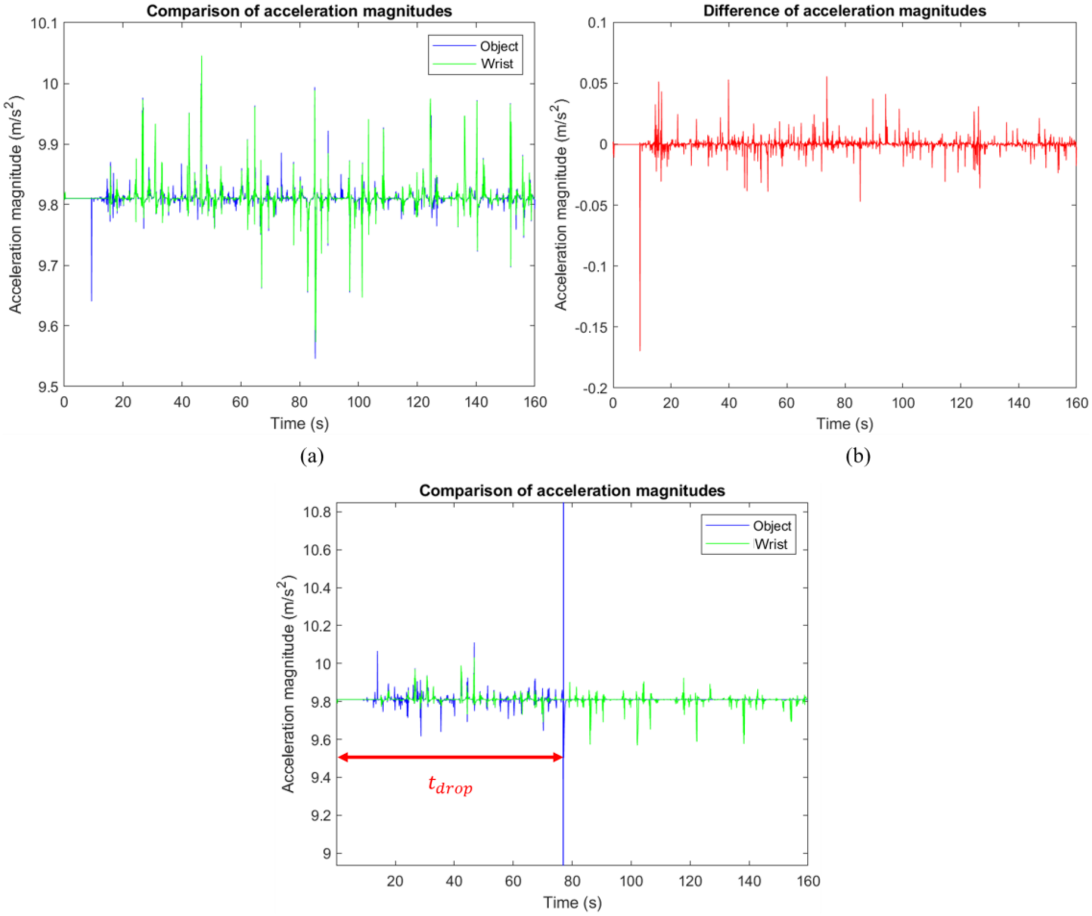

(a) (b)

(c)

Figure 31: A sample plot of the showing the magnitudes of accelerations at the wrist (green) and the object (blue). **(a)** For the case when grasp is maintained 100% of the trail, **(b)** the root mean square value of the differences between the wrist and the object is computed. **(c)** In the case when grasp fails, the grasp duration is computed by visually inspecting the instance of grasp failure, and the ratio of time when grasp is maintained is archived.

4.4 Results

4.4.1 Summary of results

A total of five objects have been grasped for the experimental trials: a glass bottle, ketchup dispenser, spray bottle, cereal box, and cubic prism. Simulation for each trial lasted 160 seconds, and 5 trials were performed for each torque multiplier for each object. The entire length of the simulation for one object summed to 416.67 minutes, totaling 2083.33 minutes (34.72 hours, 500 grasp trials) worth of data. For each trial, the magnitudes of accelerations were computed at the

Table 3: The average of the root mean square values of the differences in acceleration magnitudes throughout the experiment. The values are measured in m/s^2. The magnitudes of acceleration is less for all objects, indicating more stable grasps with the synergy-based torque control enabled.

	Glass bottle	**Ketchup dispenser**	**Spray bottle**	**Cereal box**	**Cubic prism**
Synergy enabled	**0.1815±0.0463**	**0.6336±0.1168**	**0.6441±0.2044**	**0.8040±0.3991**	**0.4677±0.0421**
Uniform torques	**0.3890±0.0848**	**0.8920±0.1960**	**1.1200±0.4339**	**1.0086±0.3506**	**0.4733±0.0440**

wrist and the object and were plotted with respect to time for analysis as can be seen in Figure 31. Grasp duration was measured by visually inspecting the perturbation plots and marking the instances where an irregularly high spike in the acceleration magnitude is observed and no response from the accelerometer attached to the object can be observed, which response indicates that the object was dropped. The relative acceleration magnitudes were computed by measuring the differences between the values obtained from the two accelerometers and the root mean square error within the timeframe that the grasp was maintained was computed. Literature suggests that it is desirable for the grasped objects to follow the same trajectory led by the grasping device [85]. The study also demonstrates that grasps with lower differences in the acceleration magnitudes result in higher quality grasps. Thus, we evaluate the stability of grasps based on the criteria of the differences in the magnitudes of relative acceleration. Grasp robustness was measured with the percentage of grasp maintained throughout the trials.

A simplified summary of the results from the experiments is summarized in Table 3, and the resulting root mean square differences in accelerations of objects are plotted in Figure 32-36. Results from Table 3 suggest that the synergistic torque modulation may lead to a more stable grasp compared to that of the non-methodical uniform torque modulation. It is interesting to note that the differences are most drastic with the spray bottle. This may be accountable to the fact that the spray bottle has the most complex shape of all five objects, and slight changes in the forces at the contact points may lead to larger motions than others.

As the sample size for comparing the two methods are small (n = 6 < 30), paired t-tests were performed for each torque multiplier throughout the trials at a 5% significance level to evaluate statistically significant differences between the two methods as they are known to be reliable even for extremely small sample sizes ($2 \leq n \leq 5$) [98][99]. Works that compare performances of robotic grasps with two or more different methods have also chosen small sample sizes from 6 to 10 based on the premise of the usefulness of t-tests with small sample sizes [100][101][102]. Thus, the statistical significance of the differences between the two control methods was investigated; resulting p-values were computed as well. T-tests were designed such that negative values indicate lower RMS results with the synergy-based control method and vice versa for positive values:

$$t(6) = \frac{\bar{x}_{syn} - \bar{x}_{uni}}{\sqrt{s^2\left(\frac{1}{n_{syn}} + \frac{1}{n_{uni}}\right)}}$$

where x_{syn} are RMS values from synergy-based grasps and x_{uni} are RMS values from synergy-based grasps. T-tests were designed such that a negative t-value correspond to a lower RMS difference with the synergy-based control method and a positive t-value corresponds to a higher RMS difference measure. The effect sizes of the t-tests were computed using the Cohen's d measure for the student t-test as we are comparing two different methods of torque modulation [103]. An effect size less than 0.2 would indicate that the difference between the two methods is trivial whereas an effect size greater than 0.8 indicates that the difference is large.

Table 4: T-tests performed for all torque multipliers for grasping the glass bottle. Null hypotheses are rejected with 5% significance level, and effect sizes are greater than 0.8 for multipliers 0.3 to 1.0.

	Torque multiplier (c)									
	0.1	**0.2**	**0.3**	**0.4**	**0.5**	**0.6**	**0.7**	**0.8**	**0.9**	**1.0**
$t(6)$	**1.1220**	**-0.4828**	**-4.1667**	**-6.5942**	**-10.4093**	**-17.7365**	**-10.4988**	**-17.5219**	**-4.6567**	**-5.0384**
p-value	**0.32**	**0.65**	**0.014**	**0.0027**	**4.8e-4**	**5.9e-5**	**4.7e-4**	**6.2e-5**	**0.0096**	**0.0073**
Effect	**0.7161**	**0.3763**	**2.3424**	**3.7880**	**5.4061**	**4.7031**	**4.3527**	**8.1512**	**2.6458**	**3.0518**

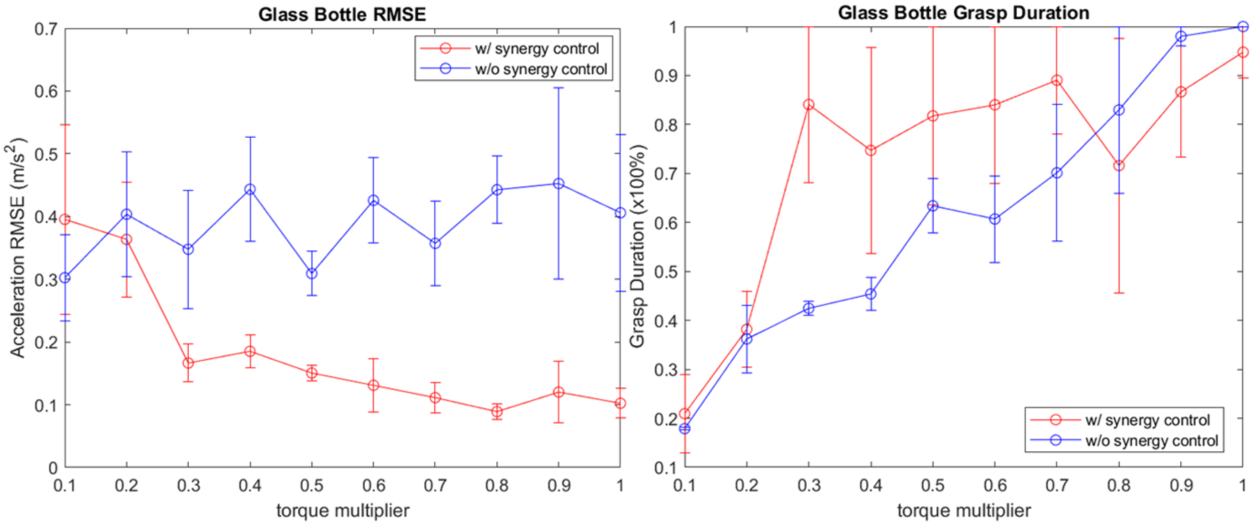

Figure 32: Experimental results for trials with the glass bottle. **(left)** The average root mean square differences for each torque multiplier are plotted with the corresponding standard deviation. **(right)** The average percentage of grasp maintained for each multiplier is plotted with the corresponding standard deviation

4.4.2 T-test analysis of perturbation trials

Figure 32 shows the mean and standard deviation throughout all trials for each torque multiplier for the glass bottle. For the glass bottle, except at the torque multiplier of 0.1, the average root mean square errors were increasingly lower with increasing torque multiplier values. With the glass bottle, increasing the net torque improved the stability of grasps with the synergy-based torque control overall. In the case of uniform torque distribution, increasing the net torque did not improve the stability of grasps with the glass bottle. An explanation for this result could be that increasing the magnitudes in a non-optimal span of contact forces does not aid in improving the

Table 5: T-tests performed for all torque multipliers for grasping the ketchup dispenser. Null hypotheses are rejected with 5% significance level, and effect sizes are greater than 0.8 for multipliers 0.4 to 1.0.

	Torque multiplier (c)									
	0.1	**0.2**	**0.3**	**0.4**	**0.5**	**0.6**	**0.7**	**0.8**	**0.9**	**1.0**
$t(6)$	**-1.8129**	**-0.4477**	**1.9904**	**-3.8369**	**-3.5953**	**-9.6481**	**-10.3120**	**-4.3648**	**-3.0411**	**-15.3164**
p-value	**0.14**	**0.68**	**0.12**	**0.019**	**0.023**	**6.5e-4**	**5.0e-4**	**0.012**	**0.038**	**1.1e-4**
Effect	**0.9449**	**0.3372**	**1.3045**	**1.1172**	**2.2070**	**6.1715**	**6.1702**	**1.9892**	**2.1323**	**3.2859**

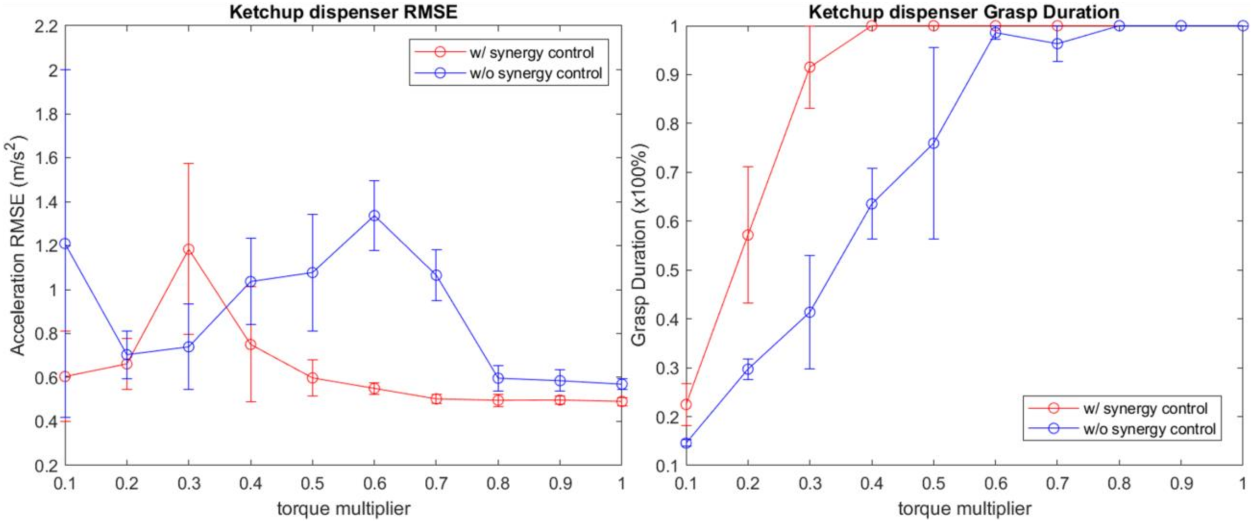

Figure 33: Experimental results for trials with the ketchup dispenser. **(left)** The average root mean square differences and **(right)** the average percentage of grasp maintained for each multiplier is plotted.

stability of grasps. Increases in the grasp durations were observed for both methods with increasing torque multipliers. Table 4 shows statistically significant differences between the two methods at torque multipliers 0.3 to 1.0 with $p < 0.05$, rejecting the null hypothesis with 95% confidence. Also, the effect sizes are greater than 0.8 for multipliers greater than 0.3. Thus, an argument can be made that the stability of grasps improved with the synergy-based torque control definitively for most torque multipliers; for torque multipliers 0.2 and 0.3, no definitive conclusions can be drawn statistically, but lower RMS values were observed, nonetheless. Overall, the grasp duration was higher with the synergy-based torque control; however, the relation reversed with the higher net torques at $c = 0.8$ to 1. Although the differences are not significant, it may be argued that increasing the magnitudes of contact forces along a non-uniform span increases the risk of grasp failure with slippery objects like a glass bottle.

For the case of the ketchup dispenser, the root mean square differences are also lower in general with the synergistic torque control as can be seen in Figure 33. A generally decreasing trend in the magnitudes with increasing torque multipliers was observed with the synergistic method, although an outlying spike is observed with a torque multiplier 0.3. A decreasing trend is not observed with the non-synergistic method except at higher torque multiplier values ($c > 0.8$). Like the case with the glass bottle, increasing the magnitudes in a non-optimal span of contact forces does not aid in improving the stability of grasps. Table 5 shows statistically non-trivial differences between the two methods at torque multipliers 0.4 to 1.0 with $p < 0.05$, rejecting the null hypothesis with 95% confidence. Also, the effect sizes are greater than 0.8 for multipliers greater than 0.4. Thus, an argument can be made that the stability of grasps improved with the synergy-based torque control definitively for most torque multipliers. For torque multipliers 0.1 and 0.2, lower RMS values were observed; however, RMS is greater on average with the synergistic method at multiplier 0.3, possibly due to irregular behavior from certain trials, explained by the high variance at $c = 0.3$. An increasing trend in the grasp duration was observed with increasing torque multipliers, and grasps were maintained longer for all cases using the synergy-based torque control.

For the case with the spray bottle, the root mean square differences are lower with the synergistic torque control with low torque multipliers as can be seen in Figure 34. Decreasing trends in the magnitudes with increasing torque multipliers were observed for both methods. Table

Table 6: T-tests performed for all torque multipliers for grasping the spray bottle. Null hypotheses are rejected with multipliers 0.4, 0.7, 0.8, and 1.0 at 5% significance level, and marginally significant results are observed at 0.2, 0.5, and 0.6 torque multipliers with 10% significance. Effect sizes are greater than 0.8 except at multiplier 0.1 and 0.9.

	Torque multiplier (c)									
	0.1	**0.2**	**0.3**	**0.4**	**0.5**	**0.6**	**0.7**	**0.8**	**0.9**	**1.0**
$t(6)$	-1.0083	-2.4271	-2.0947	-3.0582	-2.5528	-2.2563	-4.4607	-4.0021	0.1273	-4.7554
p-value	0.3704	0.0722	0.1043	0.0377	0.0631	0.0870	0.0112	0.0161	0.9049	0.0089
Effect	0.6143	1.3791	1.2187	1.5423	0.8154	0.9171	2.9983	2.7059	0.0668	3.6988

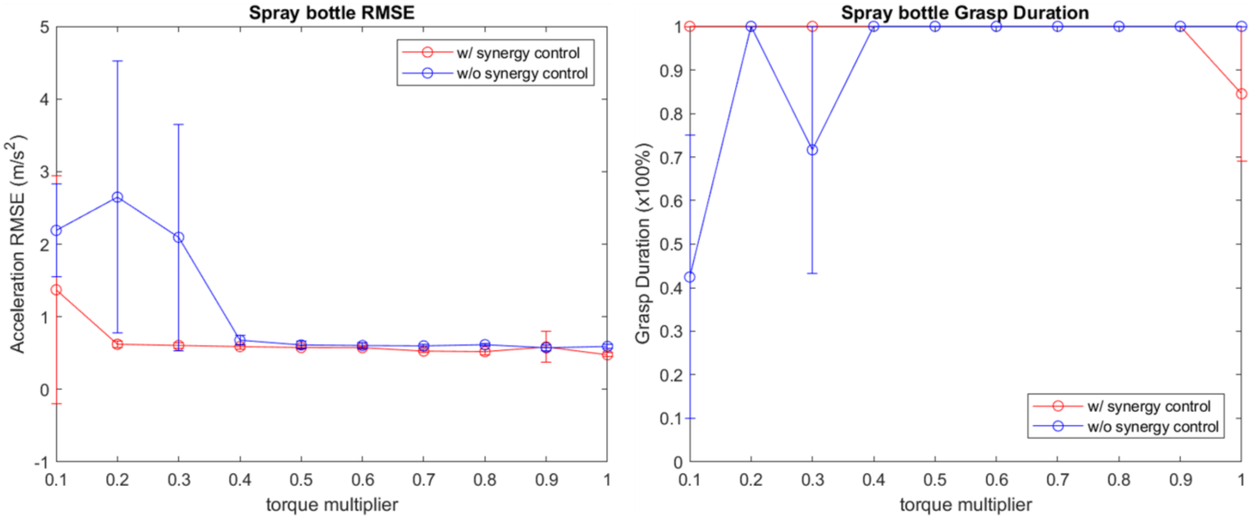

Figure 34: Experimental results for trials with the spray bottle. **(left)** The average root mean square differences and **(right)** the average percentage of grasp maintained for each multiplier is plotted.

6 shows statistically non-trivial differences between the two methods at torque multipliers 0.4, 0.7, 0.8, and 1.0 with p < 0.05, rejecting the null hypothesis with 95% confidence. Marginally significant differences are observed with torque multipliers at 0.2, 0.5, and 0.6 with 10% significance. With the effect sizes greater than 0.8 for all regions except at multiplier 0.1 and 0.9, improved grasp stability with the synergy-based torque modulation is observed in general. An increasing trend in grasp duration was observed with increasing torque multipliers, and grasps were maintained longer for most cases using the synergy-based torque control except at *c* = 1.0.

Table 7: T-tests performed for all torque multipliers for grasping the cereal box. Null hypotheses are not rejected for any multipliers at 5% significance level, and marginally significant results are observed at 0.1, 0.3, and 0.8 torque multipliers with 10% significance.

	Torque multiplier (c)									
	0.1	**0.2**	**0.3**	**0.4**	**0.5**	**0.6**	**0.7**	**0.8**	**0.9**	**1.0**
$t(6)$	**-2.4115**	**-0.1125**	**-2.1951**	**-1.0415**	**-0.0954**	**0.3704**	**-1.5342**	**-2.3327**	**-0.9632**	**-1.2187**
p-value	**0.073**	**0.92**	**0.093**	**0.36**	**0.93**	**0.73**	**0.20**	**0.080**	**0.39**	**0.29**
Effect	**1.3814**	**0.0518**	**0.8687**	**0.6987**	**0.0249**	**0.2795**	**0.5975**	**1.6083**	**0.4715**	**0.6372**

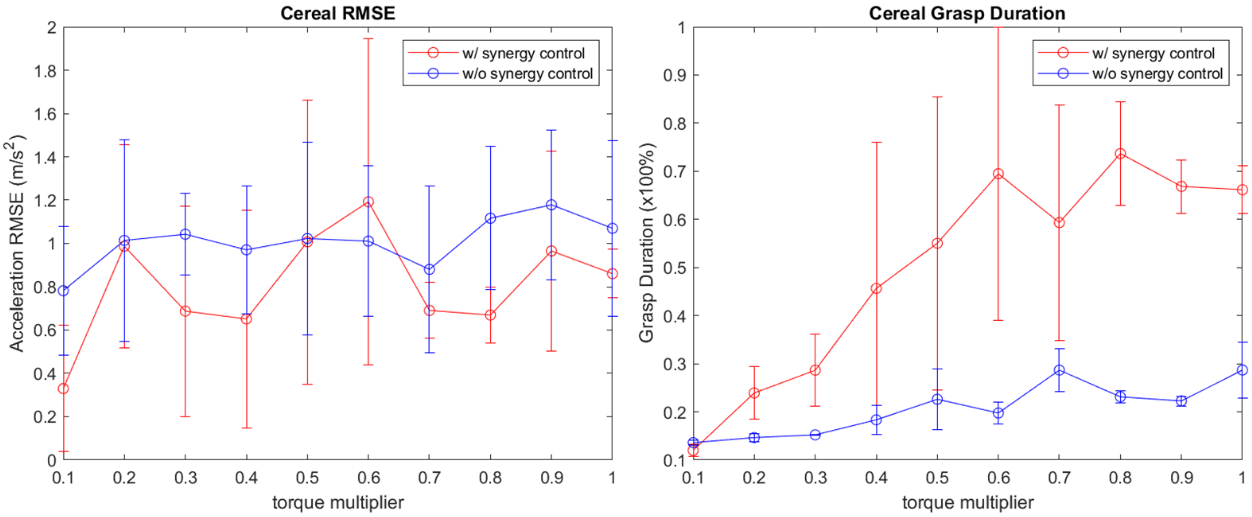

Figure 35: Experimental results for trials with the cereal box. **(left)** The average root mean square differences and **(right)** the average percentage of grasp maintained for each multiplier is plotted.

For the case with the cereal box, the root mean square differences are lower in general with the synergistic torque control as can be seen in Figure 35. However, a decrease in the magnitudes with increasing torque multipliers was not observed. Table 7 shows that the null hypotheses cannot be rejected with 95% confidence for any torque multipliers with $p < 0.05$ throughout. However, marginally significant results are observed at 0.1, 0.3, and 0.8 torque multipliers with 10% significance with negative t-values and effect sizes greater than 0.8. Unlike the case with other objects, the cereal box is held with a lateral grasp, thus relying entirely on the frictional forces; thus, grasp stability may not improve with increasing net torques from the lack of contact points

Table 8: T-tests performed for all torque multipliers for grasping the cubic prism. Null hypotheses are not rejected for any multipliers at 5% significance level.

	Torque multiplier (c)									
	0.1	**0.2**	**0.3**	**0.4**	**0.5**	**0.6**	**0.7**	**0.8**	**0.9**	**1.0**
$t(6)$	**-0.6639**	**0.1797**	**0.0264**	**1.5738**	**-0.0954**	**-1.1053**	**-1.1870**	**0.2084**	**0.8583**	**0.0392**
p-value	**0.54**	**0.87**	**0.98**	**0.19**	**0.93**	**0.330**	**0.30**	**0.85**	**0.44**	**0.97**
Effect	**0.4376**	**0.1392**	**0.0144**	**1.1198**	**0.0615**	**0.8038**	**0.5691**	**0.1292**	**0.4766**	**0.0261**

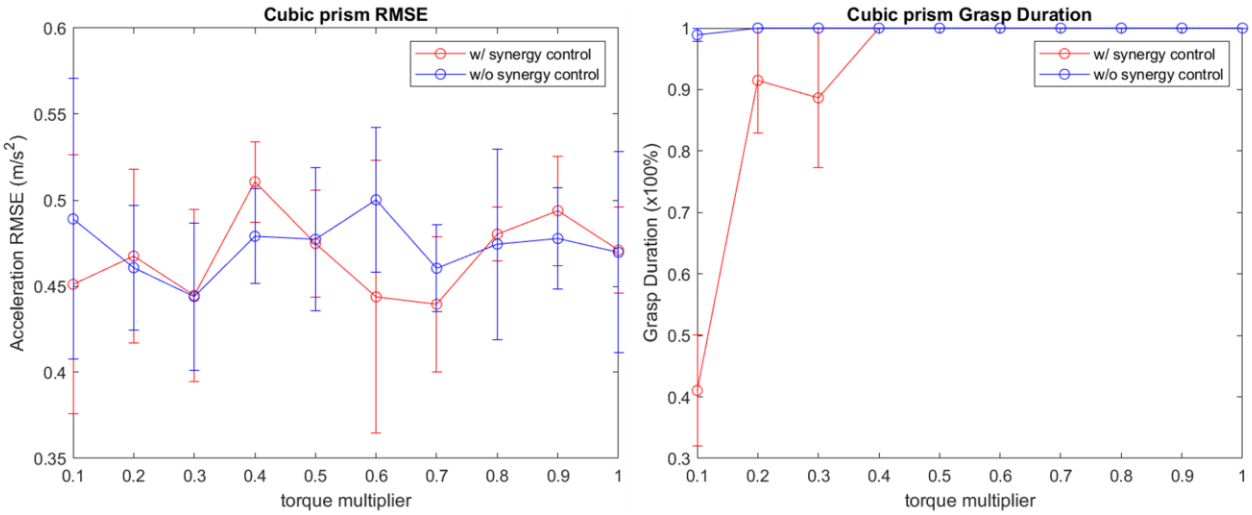
Cubic prism RMSE

Cubic prism Grasp Duration

Figure 36: Experimental results for trials with the cubic prism. **(left)** The average root mean square differences and **(right)** the average percentage of grasp maintained for each multiplier is plotted.

that constrain the object's perpendicular motion. On the other hand, an increase in the grasp duration was observed with increasing torque multipliers, and grasps were maintained longer for all cases using the synergy-based torque control. There was high variability in grasp duration with the cereal box, however, which may have also been caused by the lack of contact points constraining perpendicular motion.

For the case with the cubic prism, lower root mean square differences are not observed with the synergistic torque control as can be seen in Figure 36. A decreasing trend in the magnitudes with increasing torque multipliers was also not observed. Table 8 shows that the null hypotheses cannot be rejected with 95% confidence for any torque multipliers with $p < 0.05$

throughout. For the case of the cubic prism, the effects of using synergy-based torque modulation may not be apparent with its shape being the most geometrically uniform, thus differences between the two methods may be the most difficult to differentiate. Additionally, more frequent failures in grasps are observed at low torque multipliers with the synergistic method.

Overall, the root mean square values are visibly lower using the synergy-enabled torque control compared to the uniform control method, except for the case with the cubic prism. Statistical validation shows a strong improvement in the grasp stability with the glass bottle, ketchup dispenser, and spray bottle. This suggests that a synergistic control of torques for a uniformly shaped object like a cubic prism may not be optimal. On the contrary, the more complex the shape becomes, such as the spray bottle and the glass bottle, the differences in the root mean square error tends to become larger.

CHAPTER 5

EVALUATION OF TASK PERFORMANCE OF DATA-DRIVEN ROBOTIC PROSTHESIS

5.1 Introduction

The results from the virtual experiment via CoppeliaSim give a good validation that a synergy-based approach to grasp force modulation could generate more stable and robust grasps compared to those generated with non-methodical uniform torque modulation. As such, the last step in this thesis work is to evaluate the performance of the data-driven upper-limb prosthesis by designing and testing a physical experiment similar to the one performed via simulation using CoppeliaSim. Thus, we need the semi-anthropomorphic robotic hand developed in Chapter 3 to be able to 1) generate synergy-enabled pose and 2) generate motions with joint torque control. Also, the KUKA IIWA 14 should generate repeatable perturbation trajectories with the prosthetic hand attached to the end-effector. Finally, the prosthetic should be able to perform reach-to-grasp sequences to the object location and maintain the grasp reliably without human intervention.

5.2 Methods

5.2.1 Graphical user interface for control of prosthetic hand

To enable synergistic pose modulation of the prosthetic hand, first, a graphical user interface (GUI) to interact with the device from a computing device was created. Figure 37 shows the GUI for controlling the prosthetic hand, developed using MATLAB apps, where it allows front-end interfacing such as adding buttons, sliders, spinners, and interactive figures and back-end

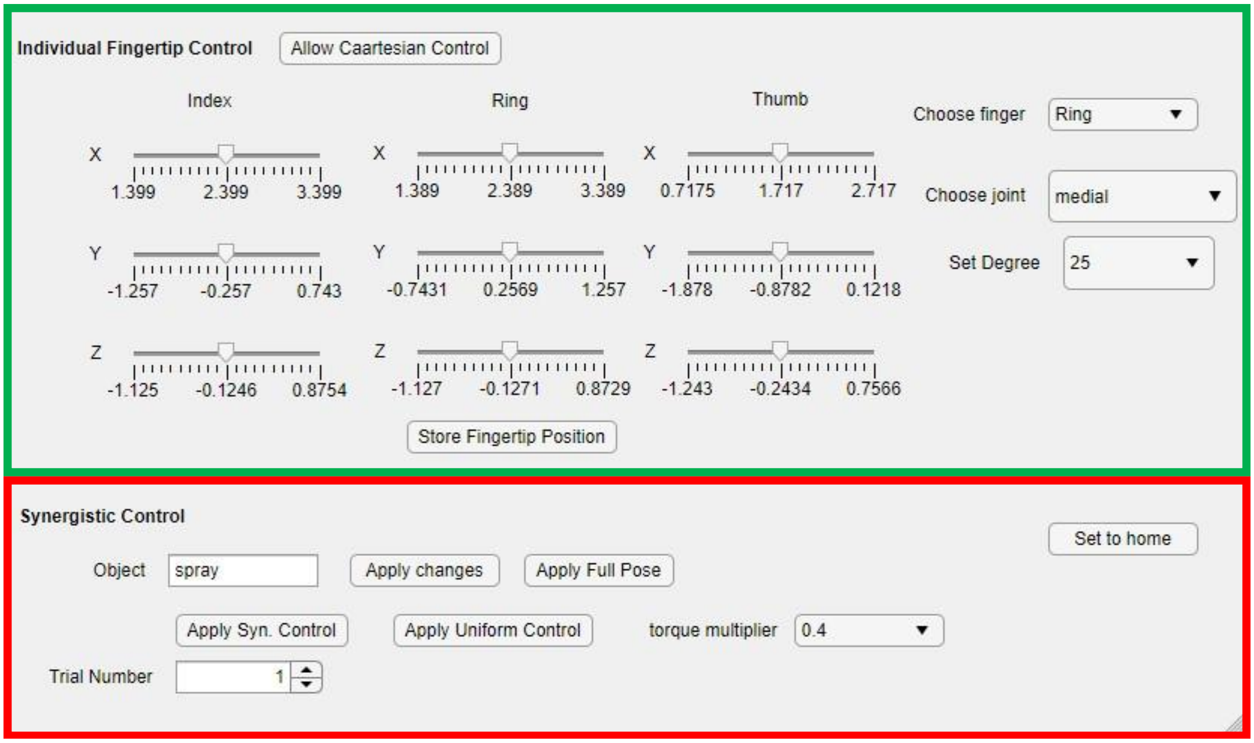

Choose finger: Ring
Choose joint: medial
Set Degree: 25
Object: spray
torque multiplier: 0.4
Trial Number: 1

Figure 37: GUI for interfacing with the prosthetic hand from the computing device via MATLAB app. The boxed area with the green borders is used for diagnosing with the device. The area bordered in red is used for the actual experimentation.

programming that creates system blocks for each component element automatically. We want two modes of interfacing with the prosthetic hand for ease of switching from diagnostic mode to experimentation mode. The upper area as shown in Figure 37 is used to vary the positions of the individual fingers and joints to verify the validity of interfacing and actuation of the prosthetic hand. This was extremely useful in diagnosing issues with either the robotic device or communication in case of mechanical, electrical, or software issues. The lower area is used for the actual experimentation with the perturbation trial; it allows the user to input the object name and trial number, select different grasp actuation modes during the grasp sequences, select the torque multipliers, and choose between the two torque modulation modes.

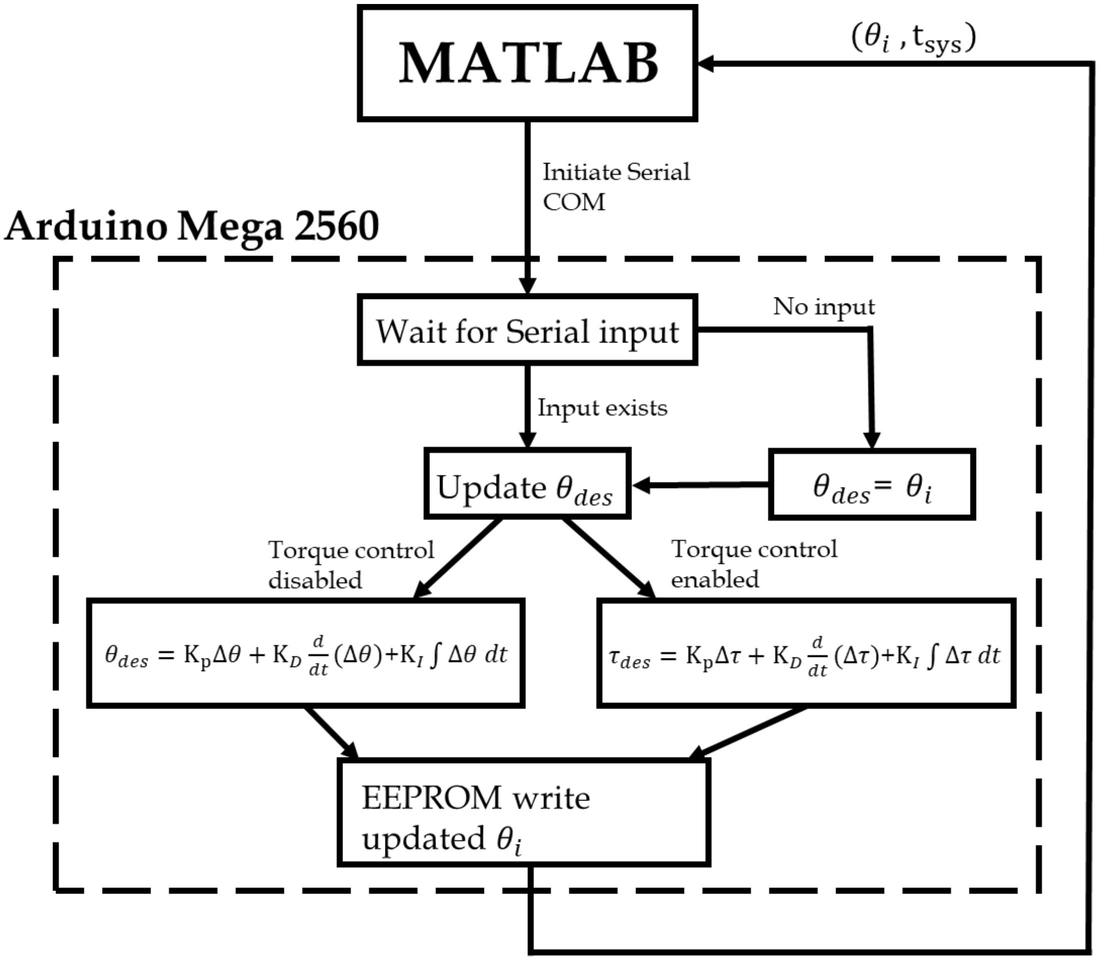

Figure 38: System diagram of communication with MATLAB app and each Arduino Mega 2560 microcontroller.

5.2.2 Synergistic control of prosthetic hand with MATLAB

Control input to the prosthetic hand from MATLAB was executed using two Arduino Mega 2560 microcontrollers: one for the ring and index fingers and the other for the thumb. MATLAB acts as the master device with the main clock, and the two microcontrollers function as slaves, thus synchronization of the microcontroller clock was not a concern. The system diagram showing communication between each microcontroller and MATLAB is shown in Figure 38. MATLAB initiates serial communication with the microcontroller upon the startup of the GUI. The microcontroller loops indefinitely while executing PID control of the joint poses with or without

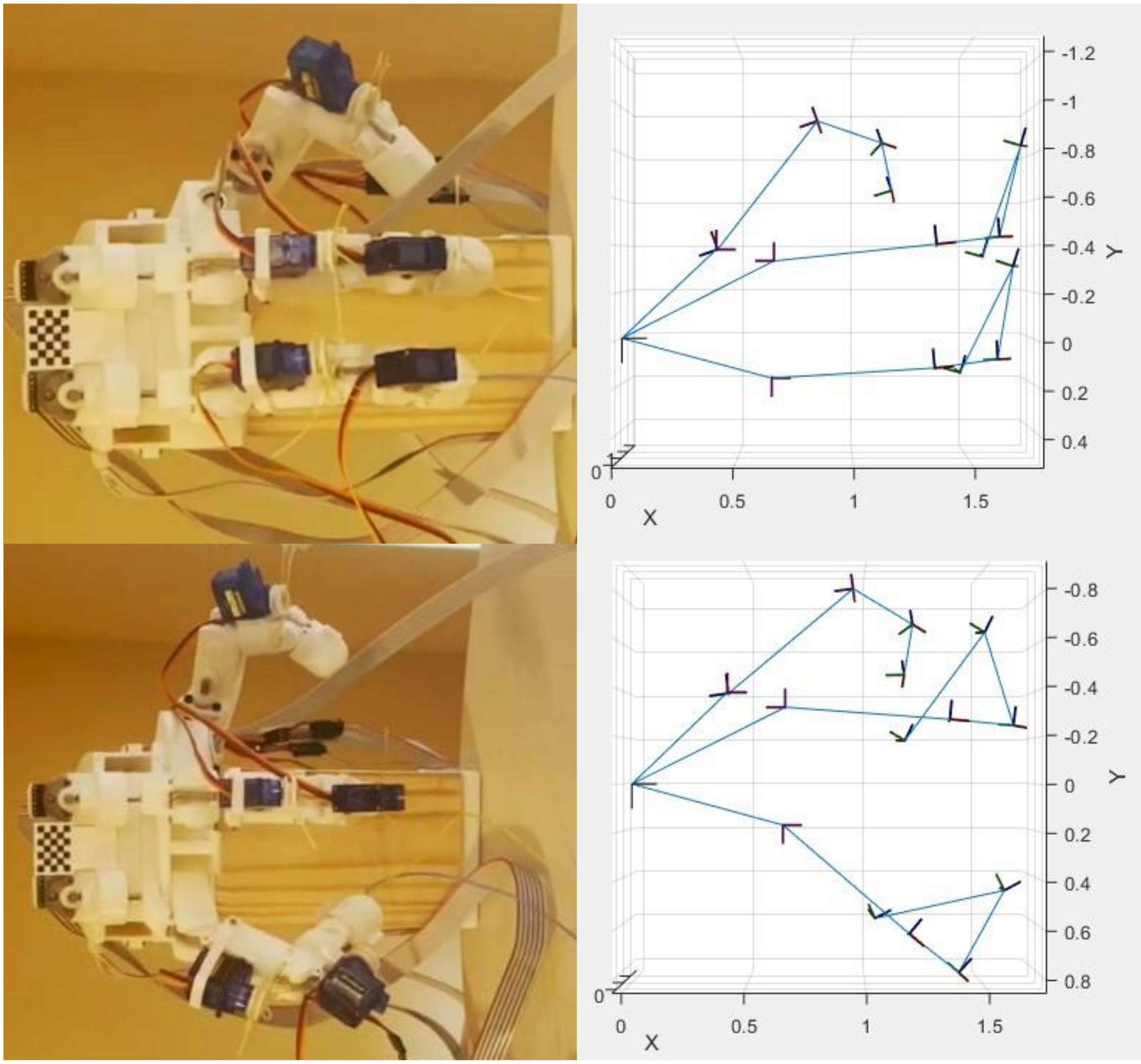

Figure 39: Comparison of the actual prosthetic hand configuration vs. skeletal model generated by MATLAB Robotics Toolbox. The skeletal model reflects the actual joint-to-link motions characterized with the DH parameter optimization, resulting in medial and distal linkages being seemingly skewed.

input from MATLAB. The user chooses the control mode using the GUI interface and applies the desired joint configurations by pressing the “Apply Changes” button as shown in Figure 37. Once input is prompted from MATLAB, the microcontroller updates the desired joint position θ_{des}, and PID control is applied accordingly. The case for torque control is detailed in the section below. For each iteration, the updated joint position θ_i is written into EEPROM memory on the microcontroller. The updated joint positions and timestamp—used in data collection mode only—are communicated back to MATLAB and are stored when the data storage option is selected in GUI.

Steps for applying synergistic grasp poses to the prosthetic hand are straightforward after the setup. The robustness of the generated grasps was validated visually using a skeletal representation of the prosthetic hand using MATLAB's Robotics Toolbox. A separate GUI that allows the user to vary to the first four principal components and show the skeletal representation was created. Figure 39 shows the prosthetic hand mounted on a wooden block, and the joint configurations were recorded with the desired positions computed with MATLAB. Although there may be errors between the actual coordinates of the fingertips and the desired coordinates as demonstrated in Chapter 3, the joint values computed from the encoders matched those prompted by MATLAB.

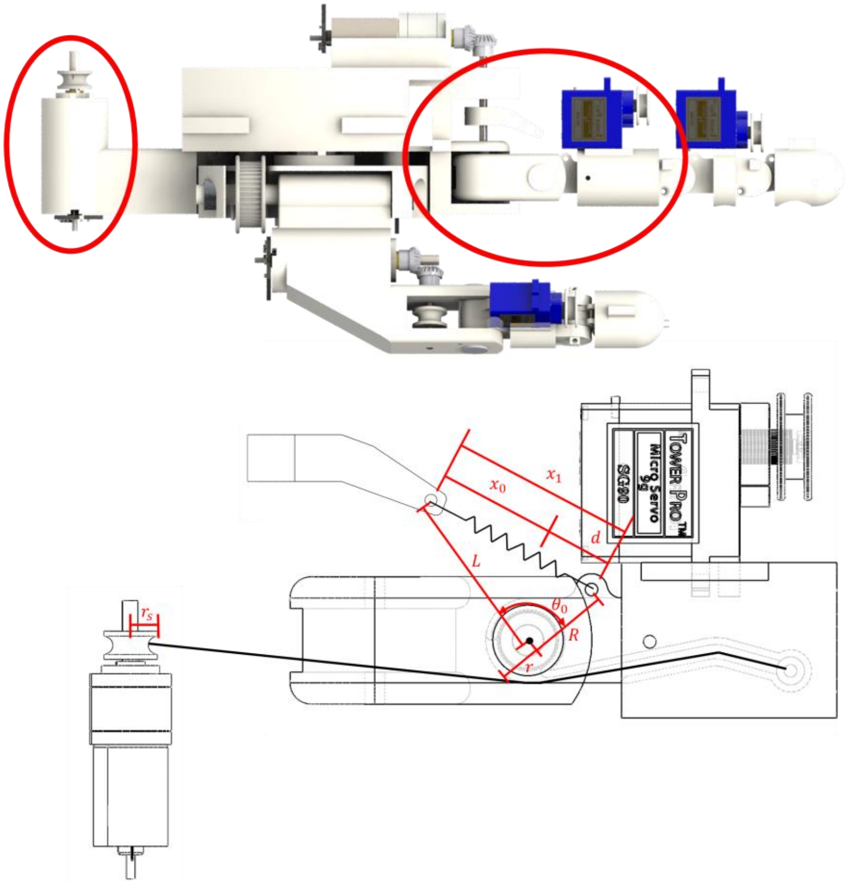

Figure 40: Geometric analysis for computing motor to PIP joint torque transmission. **(top)** The regions for analysis of PIP joint torque modulation are circled in red. **(bottom)** Simplified sketch of the PIP joint of the index/ring finger. Geometric properties necessary to compute the force/torque equilibrium are labeled.

5.2.3 Joint torque modulation with modeling

For accurate torque modulation, as we apply a quasi-static approach in the joint torque/end-effector force control, the static modeling of the prosthetic hand needed to be established. As such, each joint that was to be utilized for torque modulation was modeled accordingly. For example, the PIP joints on the index and the ring finger are flexed and extended with a force/torque balance between the Kevlar tendon thread and the linear spring as demonstrated in Figure 40. As a linear spring is being used for the extension, the relationship between the spring extension and the joint displacement is somewhat tricky. First, the torque equilibrium about the center of rotation of the PIP joint can be written as

$$\sum \tau_{PIP} = \vec{R} \times \overrightarrow{F_{sp}} - \vec{r} \times (\frac{\vec{\tau}_{motor}}{r_s}) \tag{5.1}$$

$$F_{sp} = k(x' - x_0)$$

with $x_0 = 13.2\ mm$ being the equilibrium length of the music wire steel spring and $k = 4.54 \frac{N}{mm}$ with the two springs placed in parallel. $x_1 = 14.67\ mm$ is the pre-extended length between the two pins for holding the spring with joint displacement $\Delta\theta = 0$ with $d = 1.47\ mm$. Changes in the spring length as a function of $\Delta\theta$ can be determined using motion equations like piston-crank mechanisms. The distance between one end of the spring pin attached to the base of the prosthetic hand and the center of rotation of the peripheral phalanx L is constant regardless of the joint displacement as well as R, distance from the center to the other pin. For all $\Delta\theta$, the length of the spring is merely the opposite side of the triangle formed by L, R, and angle $\theta_0 + \Delta\theta$, with θ_0 the base angle formed by the spring and the pins at $\Delta\theta = 0$. Thus, the new length x' can be formulated with the law of cosine

$$x' = \sqrt{r^2 + R^2 + 2rRcos(\theta_0 + \Delta\theta)} \tag{5.2}$$

where θ_0 is computed with

$$x_1 = \sqrt{r^2 + R^2 + 2rRcos(\theta_0)} = 14.67\ mm$$

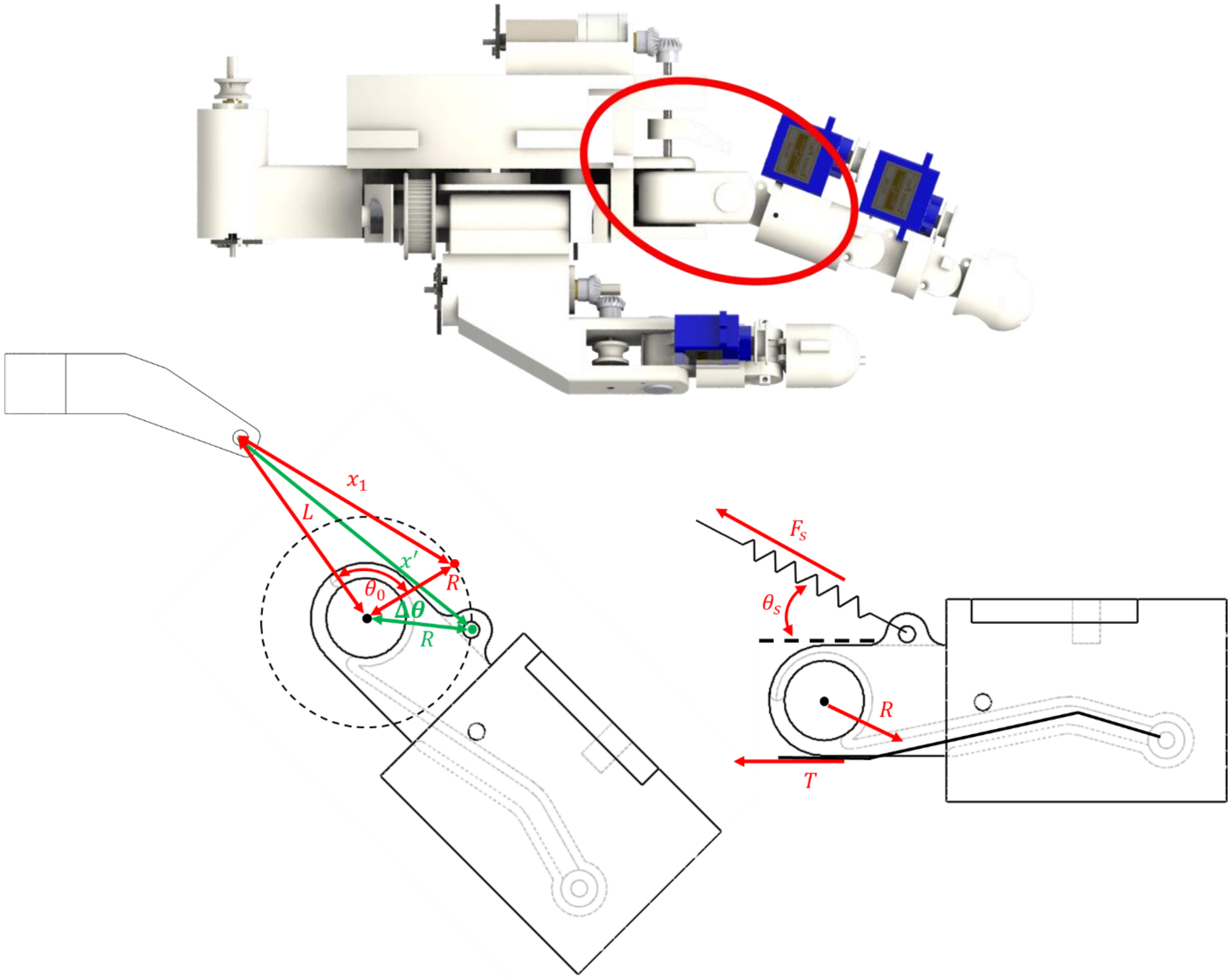

Figure 41: Continued geometric analysis for computing motor to PIP joint torque transmission with joint displacement $\boldsymbol{\Delta\theta}$. **(top)** The regions for analysis of PIP joint torque modulation are circled in red. **(bottom)** Sketch of the PIP joint under displacement $\boldsymbol{\Delta\theta}$. The effects of varying $\boldsymbol{\Delta\theta}$ on the spring lengths and resulting torque equilibrium is demonstrated.

Also, the cross-product terms in Equation 5.1 become

$$\sum \tau_{PIP} = R \cdot F_{sp,\perp} - r \cdot \left(\frac{\tau_{motor}}{r_s}\right) \tag{5.3}$$

$$F_{sp,\perp} = F_{sp} \cos\left(\theta_s - \Delta\theta\right)$$

where θ_s is the base angle formed by the spring and body of the phalanx at $\Delta\theta = 0$. The tension from the Kevlar thread will always act perpendicular to the axis of rotation due to enclosure from the thread guide. Thus, the net torque at the PIP joint as a function of the joint displacement $\Delta\theta$ and input motor torque becomes:

$$\tau_{pip} = R \cdot k(\sqrt{r^2 + R^2 + 2rRcos(\theta_0 + \Delta\theta)} - x_0) \cdot \cos(\theta_s - \Delta\theta) - r \cdot (\frac{\tau_{motor}}{r_s}) \tag{5.4}$$

For the other joints that rely on spur gears, worm gears, and timing belts for flexion and extension, the resulting static torques have a linear, independent correlation with the motor torques and can be easily characterized by the gear ratios associated with each transmission mode.

Modulation of the motor torques was performed with PID control of the supply current to the motors; current monitor capabilities offered by the Pololu Dual TB9051FTG Motor Driver

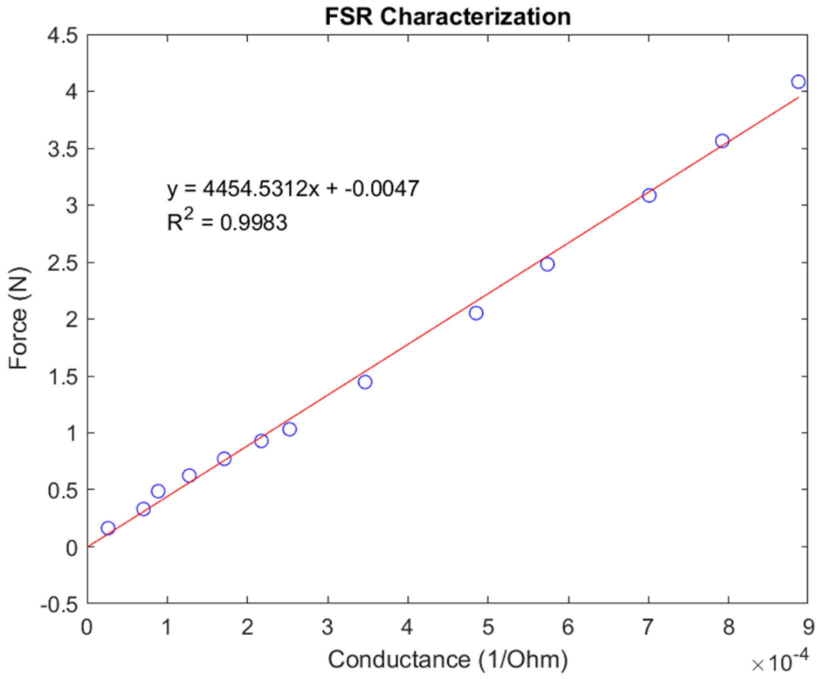

Figure 42: The force profile applied on the force sensitive resistor yields varying conductance measurements. The results show a highly linear correlation with $\boldsymbol{R^2}$ = 0.9983.

Shield for Arduino were utilized as inputs to the PID controller. There are two current monitor outlets for each motor driver for the two motor channels. Each outlet provides a monitor output with a resolution of 500 mV/A, and according to the manufacturer, the torque to current correlation for the 78:1 Gearmotor at 6V is:

$$I(\tau) = 0.12 + 0.061\tau \tag{5.5}$$

with I in amperes and τ in kg-f·mm. The limitations of current monitoring are that it cannot detect current less than 0.14 A—corresponding motor torque at 0.328 kg-f·mm (3.22 mN·m)—and measurements of current greater than 1.6 A—torque at 23.93 kg-f·mm (234.71 mN·m)—become noisy.

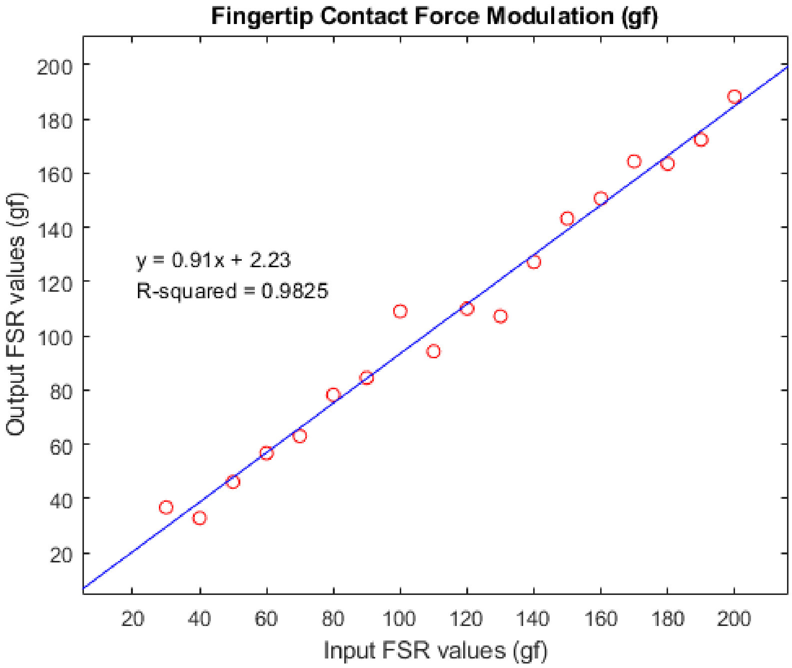

Figure 43: A comparison of the input force levels and the measured results. A highly linear correlation is observed with $\boldsymbol{R^2}$ = 0.9825, but the relationship is not one-to-one due to systematic error.

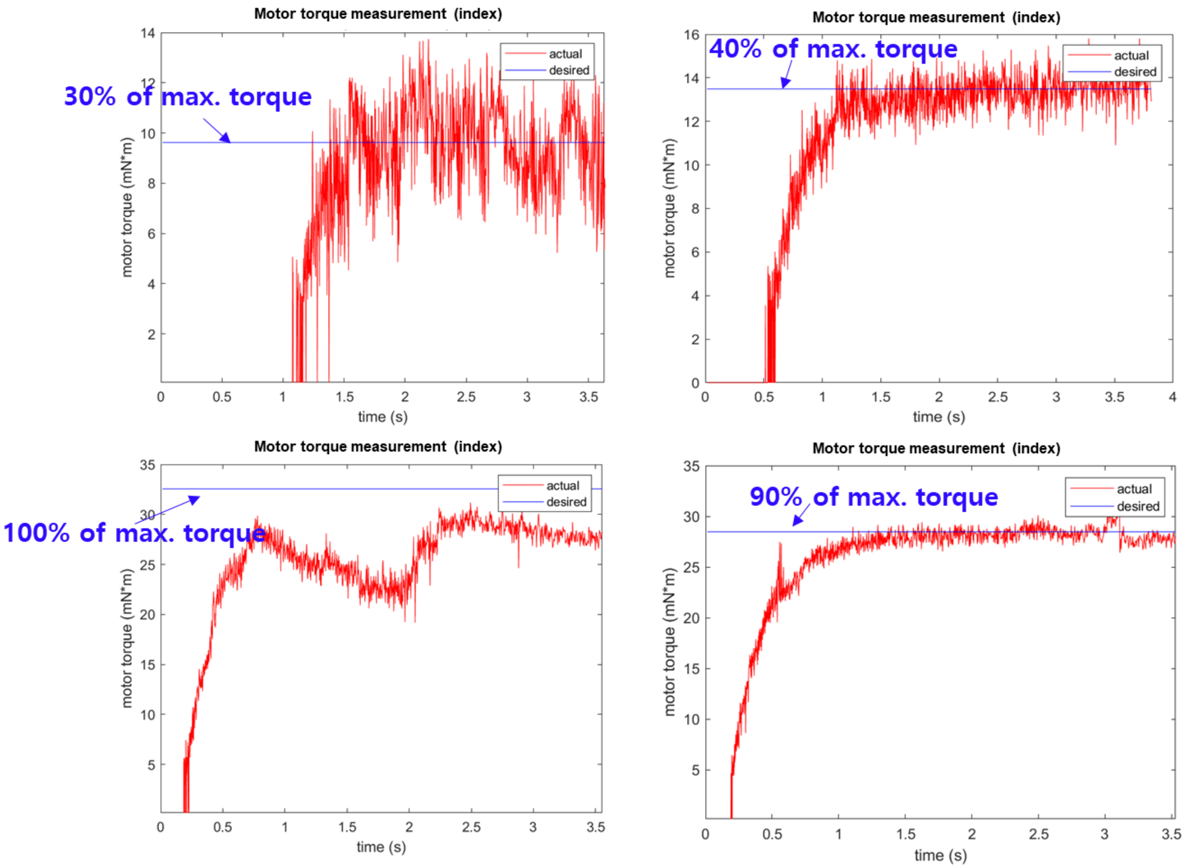

Figure 44: Current monitor outputs after applying a moving average low pass filter with 50 samples are plotted. Dead zones and saturation limits of motor torque controls due to either noise **(top left)** or failure to reach desired torque output **(bottom left)**.

Contact force modulation using current control of motor torques was validated by mounting a calibrated force-sensitive resistor on the index fingertip of the prosthetic hand and commanding it to apply pressure on an elevated mount. The force-sensitive resistor (FSR 402, Interlink Elec.) has a sensitivity range of 0.2 - 20 N with continuous, analog resolution with a 14.68 mm diameter active area and was calibrated using the Instron Force Testing System, where the results from calibrations are shown in Figure 42. The conductance vs. output force correlation is highly linear with R^2 = 0.9983. The prosthetic hand was held on a wooden mount, and the output forces as measured by the force-sensitive resistor were compared to the desired force values. The input forces varied from 0.025 kg·f to 0.2 kg·f, and the resulting plot comparing input-output mapping is shown in Figure 43. Although the mapping is highly linear with R^2 = 0.9829, the mapping is not one-to-one due to systematic error. Candidates for statistical error include internal friction, unaccounted spring deformations, and uncertainty in geometric measurements. Scaling and shifting corrections were made to the command input forces to match the desired force levels.

The dead zone and saturation limits of motor torque control with the current monitor inputs were tested by sequential ramping the output torque from 10% to 100% of maximum torques (3.17 to 31.68 mN·m) of grasping tasks with the five objects chosen from Chapter 4, determined from the grasp dataset. Outputs from the current monitor was smoothed with a moving average low pass filter using 50 samples, resulting in a sampling rate of 100 Hz for the Arduino Mega 2560, an adequate number considering that MATLAB serial communication is executed at 45 Hz. Time responses from the torque monitor for given input torque are plotted in Figure 44. Analysis of the output current levels revealed that the signal noise is greater than 20% for all torque outputs less than 12.67 mN·m, 40% of maximum torque, and the signal reached saturation at output greater than 28.52 mN·m, 90% of maximum torque. Thus, torque output was defined by the relation

$$\tau_{out} = \begin{cases} 0, & \tau_{in} < 12.67\, mN \cdot m \\ \tau_{in} & 12.67 \le \tau_{in} \le 28.52 \\ 28.52 & \tau_{in} \ge 28.52 \end{cases} \tag{5.6}$$

However, the experiment is limited to the range where $\tau_{out} \le 28.52\, mN \cdot m$ as it will be detailed in section 5.3.

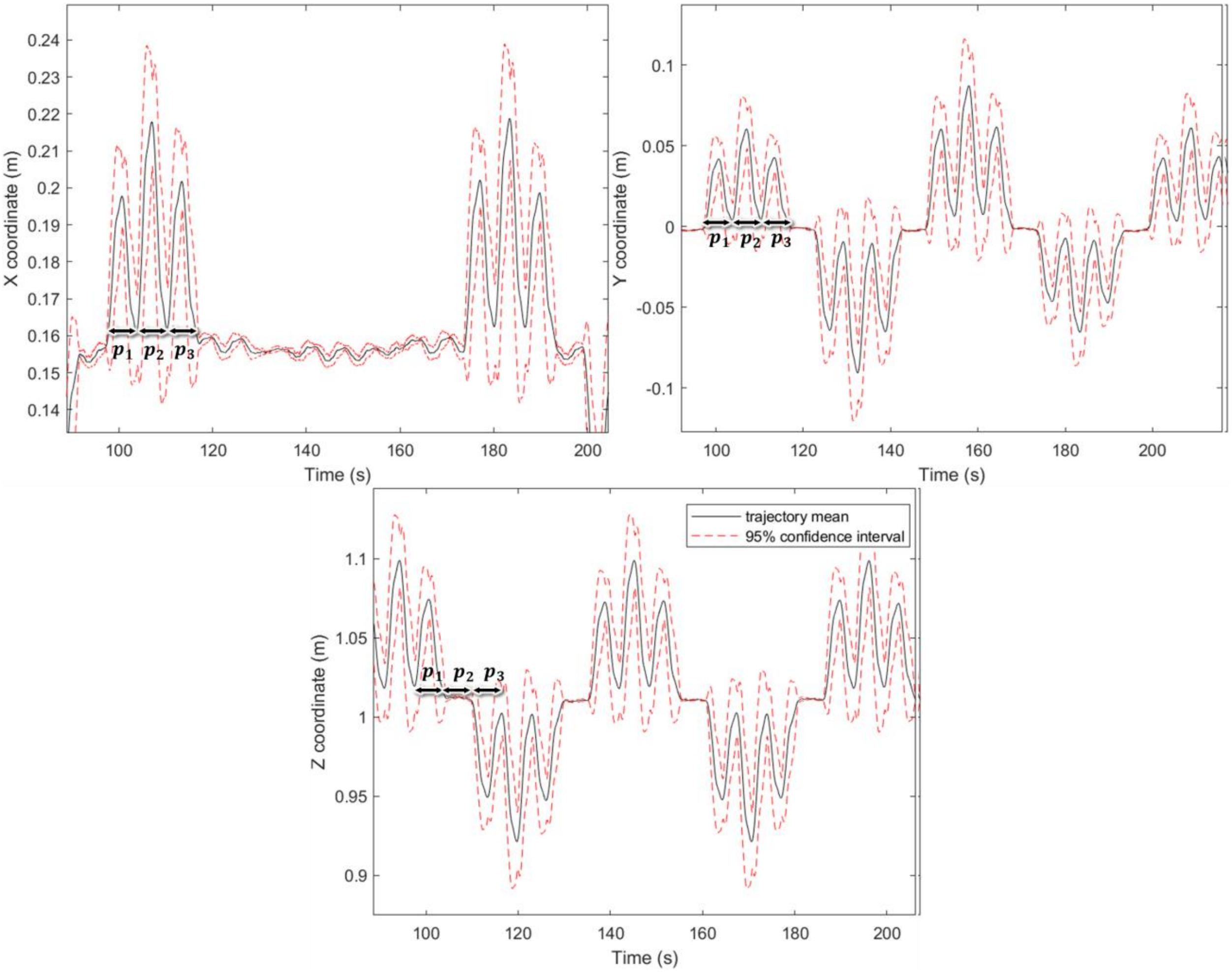

Figure 45: Trajectory means and the 95% confidence intervals of the KUKA IIWA 14 end-effector coordinates for X, Y, and Z axes. Each peaked curves $(\boldsymbol{p_1}, \boldsymbol{p_2}, \boldsymbol{p_3})$ corresponds to a pair of motion to and from the center and surface of the sphere illustrated in Figure 28.

5.2.4 Trajectory generation with KUKA IIWA 14

For generating the perturbation sequences, the KUKA IIWA 14 serial manipulator was programmed to follow the trajectories containing the perturbation waypoints. The Robot Operating System (ROS) and its package for KUKA were utilized to communicate with a Linux Ubuntu device, used as a master to communicate with KUKA. Cubic B-spline trajectories were generated to allow smooth, non-abrupt motions between waypoints. To test the repeatability of the perturbation sequences, the prosthetic hand was mounted to the end-effector of the KUKA IIWA 14 serial manipulator, and the end-effector coordinates were recorded for validation. Figure 45 show sections of the perturbation sequence, where the trajectory means in each X, Y, and Z coordinate and their corresponding 95% confidence intervals are plotted. The deviations were greatest at the Z-axis with the mean deviation of 0.765 cm and were the least along the Y-axis at 0.49 cm. The propagated uncertainty of the absolute distance of the end-effector with respect to the sphere center can be modeled by:

$$f = \sqrt{X^2 + Y^2 + Z^2}$$

$$\sigma_f = \sqrt{\left(\frac{\partial f}{\partial X}\right)^2 \sigma_X^2 + \left(\frac{\partial f}{\partial Y}\right)^2 \sigma_Y^2 + \left(\frac{\partial f}{\partial Z}\right)^2 \sigma_Z^2}$$

$$\therefore \sigma_f = \sqrt{\left(\frac{X}{\sqrt{X^2 + Y^2 + Z^2}}\right)^2 \sigma_X^2 + \left(\frac{Y}{\sqrt{X^2 + Y^2 + Z^2}}\right)^2 \sigma_Y^2 + \left(\frac{Z}{\sqrt{X^2 + Y^2 + Z^2}}\right)^2 \sigma_Z^2} \quad (5.6)$$

Computing for the average standard deviation σ_f yielded 0.800 cm. The margin of error is less 1 cm compared to 10 cm perturbation distance—8% error with 95% confidence interval—thus the perturbations can be assumed repeatable.

5.2.5 Sensor characterization

Previous studies support the use of a set of accelerometers to characterize the stability of grasps using the difference in magnitudes of accelerations between the object and the hand/grasping device [104][105][106]. Thus, characterization of the relative accelerations between the prosthetic hand and the object was achieved with a pair of ADXL 335 3-axis accelerometers. As we have observed a maximum acceleration magnitude of 4.246 m/s^2 throughout the simulation with an average standard deviation of 0.2806 m/s^2, the specifications of ADXL 335 seemed suitable for our experimental setup with an operating range of -3 to 3 g (-29.43 to 29.43 m/s^2). The sensitivity of the device is 300 mV/g, whereas the Arduino Mega 2560 analog input has a 4.9 mV resolution, resulting in the measurement resolution of 0.16 m/s^2. Offset in the differences between the two accelerometers have been characterized and calibrated in each axis, resulting in an average root-mean square error of 0.22 m/s^2 regardless of the relative orientation between the two sensors.

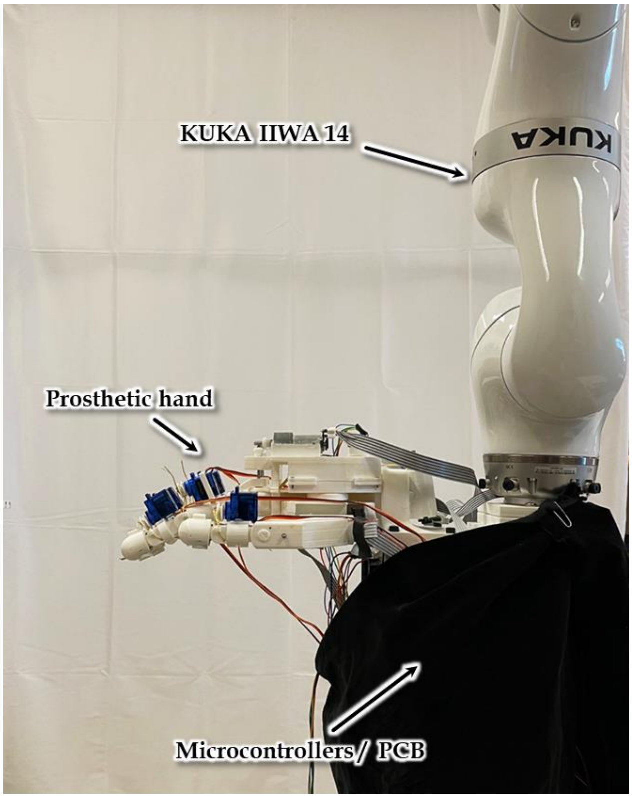

Figure 46: Prosthetic device mounted to the end-effector of the KUKA IIWA 14 serial manipulator. The microcontrollers and the PCB are covered with fabric to attain better view of grasps formed.

5.3 Experimentation

5.3.1 Experimental method

The protocols for conducting the experiments are almost identical to those followed in the simulated experiments detailed in Chapter 4; however, some differences are made to include changes in the perturbation patterns and choice of domain for the torque multiplier inputs. For comparison with prior grasp perturbation studies, a set of rotational perturbations about the wrist was included in series with the linear perturbation from the sphere center to the outer surface points [107][108][109][110]. The rotation sequence begins at 0° and rotates back and forth from 5°, -5°, 10°, -10°, and up to 45° and -45°, increasing orientation by ±5° increments. The order of linear perturbations and rotational perturbations are switched from trial to trial for randomization. Also,

Figure 47: Grasps formed for each of the five objects: **(Top left)** glass bottle, **(Top middle)** ketchup dispenser, **(Top right)** cubic prism, **(Bottom left)** spray bottle, **(Bottom right)** cereal box.

as we determined in section 5.2, the range of torque multiplier *c* is confined between 0.4 to 0.9 in 0.1 increments to maximize the use of intervals that allow efficient torque modulation, avoiding dead zones as much as possible and saturation of torque efforts. The remaining experimental protocols remain the same as those followed in simulation; perturbation trials were performed on the same five objects: glass bottle, cubic prism, cereal box, spray bottle, and ketchup dispenser.

Prior to conducting the perturbation experiments, the prosthetic hand was mounted to the KUKA arm using a custom fabricated mount as shown in Figure 46. The mount encloses all internal wirings, microcontrollers, and custom printed circuit boards, and it is locked to the prosthetic hand and KUKA arm with 21 M6 screws. Power and communication connections were minimized to four lines, three for serial communications from the three microcontrollers to the laptop device and one 6V power source connected to a wall plug, so that all the necessary electrical and signal connections are secured to withstand hours of perturbations. Furthermore, we rely on

MATLAB for all kinematic and dynamic computations as well as storing data and communication with the microcontrollers.

Unlike the case with the simulated experiments, the reach-to-grasp sequence of the prosthetic hand to form a synergistic grasp on an object is unavoidable, especially when human intervention is not desirable throughout the entire perturbation trial. Thus, we used a custom-made table, made with PVC pipes and foam board, to place the objects during the pre-grasp phase, so that the prosthetic hand/KUKA system could perform a reach-to-grasp sequence without intervention from the observer. For each object shown in Figure 47, a customized stand fabricated with PLA is placed at an optimal position to hold the object above the surface of the table. Positionings of the stands are chosen such that the prosthetic hand does not collide with the object, the table, and the stand itself during the reach to grasp phase. The base of the table was placed 40 cm from the center of the perturbation sequences to avoid collision with the prosthetic hand throughout the trial. The trajectories for the reach-to-grasp phases were customized for each object to maximize grasp successes. Factors that were considered in the formation of the trajectories include object geometry, pre-grasp pose geometry, directions of motions formed by the fingers of the prosthetic hand, and locations of the PLA stands with respect to the object and the prosthetic hand. As the main focus of this thesis work is the stability and robustness of held grasps, optimization of trajectories is not performed extensively. However, choices for trajectory selection were limited to avoid any undesired collisions or motions; thus, the effects of systematic errors should be minimized. The different stages in hand transportation from pre-grasp before contact with the object to stable grasp after picking up the object are shown in Figure 48.

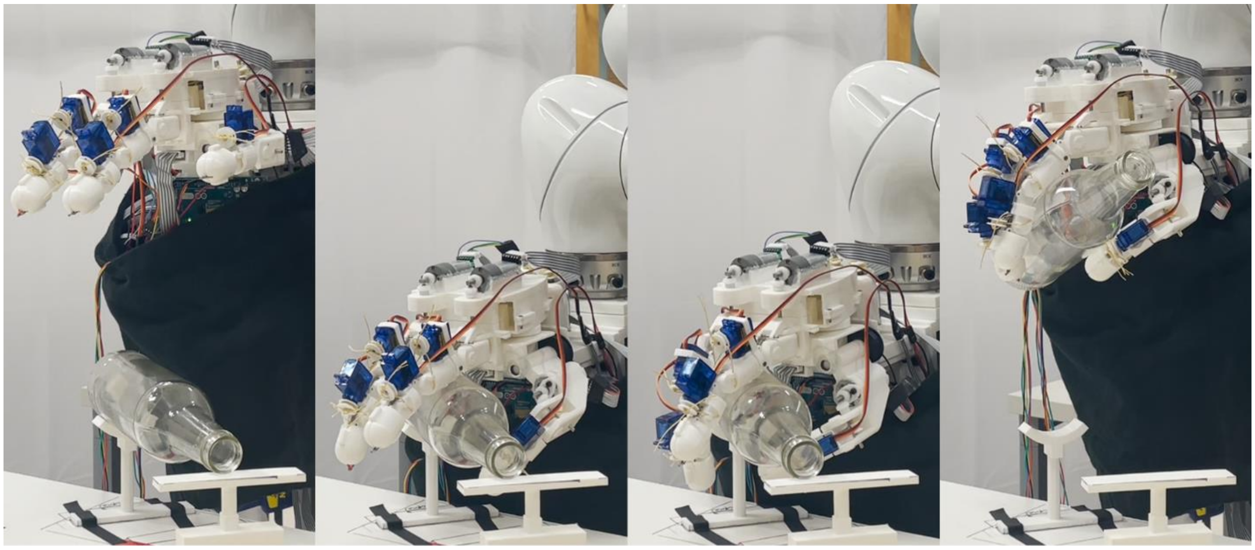

Figure 48: The stages of hand transportation from pre-grasp before contact with the object to stable grasp after picking up the object.

5.3.2 Grasp modulation protocols

The following steps were observed for each perturbation trial:

1. The base of the prosthetic hand starts at a default position away from the target object before the reach-to-grasp phase. The prosthetic hand joints are all configured to their inertial positions in the pre-grasp phase. With the GUI for interfacing with the prosthetic hand (Figure 37), the trial number, torque multiplier *c*, and object name are inputted before proceeding with the trial. The MATLAB app configures the robotics model to the synergistic pose associated with the inputted object, but changes are not applied to the prosthetic hand until *Apply Changes* button is pressed via GUI. The prosthetic hand approaches the object placed on a table as the Ubuntu device initiates the reach-to-grasp trajectory associated with the object for the trial.

2. When the trajectory for the approach is complete, the synergistic pose associated with the selected object is partially initiated. This allows the thumb to reach its goal configuration while the index and ring fingers do not make contact with this object. This step is necessary to avoid

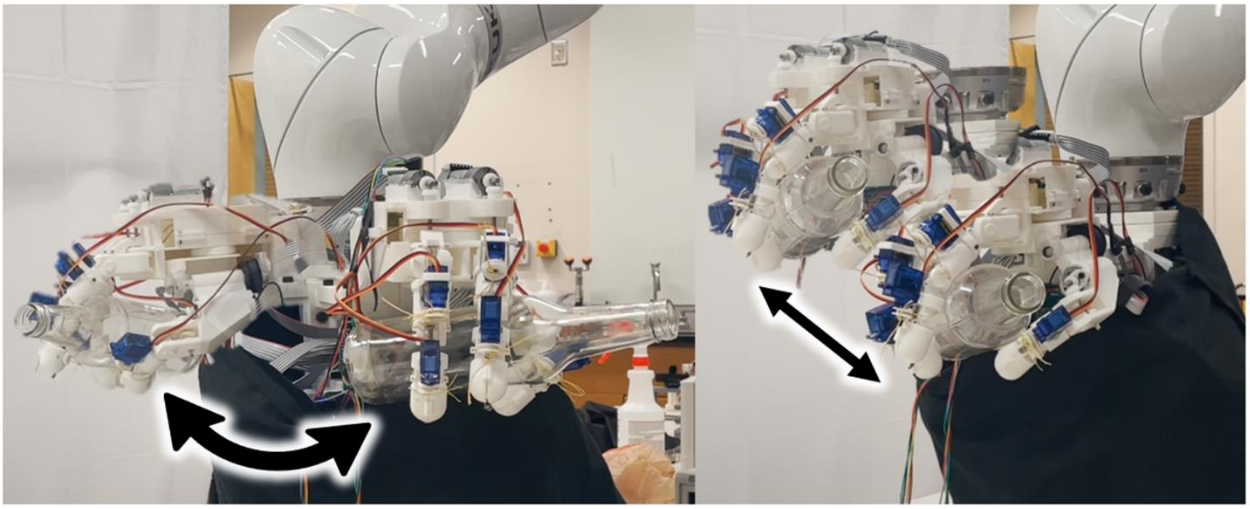

Figure 49: The perturbation sequences while grasping a glass bottle. The left image shows the rotational perturbation sequence, and the right image shows the linear perturbation sequence.

premature contact with some fingers (typically the index and the ring fingers) while the others (usually the thumb) are reaching toward the goal positions. After the thumb's motion is stabilized, the fingers close in on the object by fully enabling the synergistic pose (*Apply Full Pose* on Figure 37). When the synergistic pose is formed, one of the two methods of torque modulation—synergistic or uniform—is selected and applied to the prosthetic hand (*Apply Force Control* or *Apply Uniform Control*). After approximately 20 seconds, the KUKA arm returns to the initial position of the perturbation phase. This step lasts for approximately 60 seconds; Figure 48 shows the motions involved in steps 1 and 2.

3. After the KUKA arm reaches the initial state of the perturbation sequences, data collection of the KUKA joint states, prosthetic hand joint displacements and torques, and measurements from the accelerometers is initiated. The perturbation trajectories are initiated with the ROS terminal, and the order of the perturbation sequences (rotational vs linear) are interchanged for different trials. Figure 49 shows images of the directions of motion for the two different perturbation sequences. The combined perturbation sequences last 310 seconds—160 seconds for the linear perturbation and 150 seconds for the rotational perturbation. While the object is held within grasp,

any changes in joint displacements affect the grasp as the Jacobian matrices and the virtual spheres of the robotics model in MATLAB are updated, thus are the desired output torques. Instances of failed grasps are recorded for analysis on grasp robustness—refer to Appendix C.

4. At the end of the perturbation sequences, data measurements are halted, and the prosthetic hand's joint configurations return to its initial position. Preceding the next trial, two minutes are used to cool the temperature of the DC motors as the accumulation of heat due to prolonged trials causes damage to the motors and the structure of the prosthetic hand.

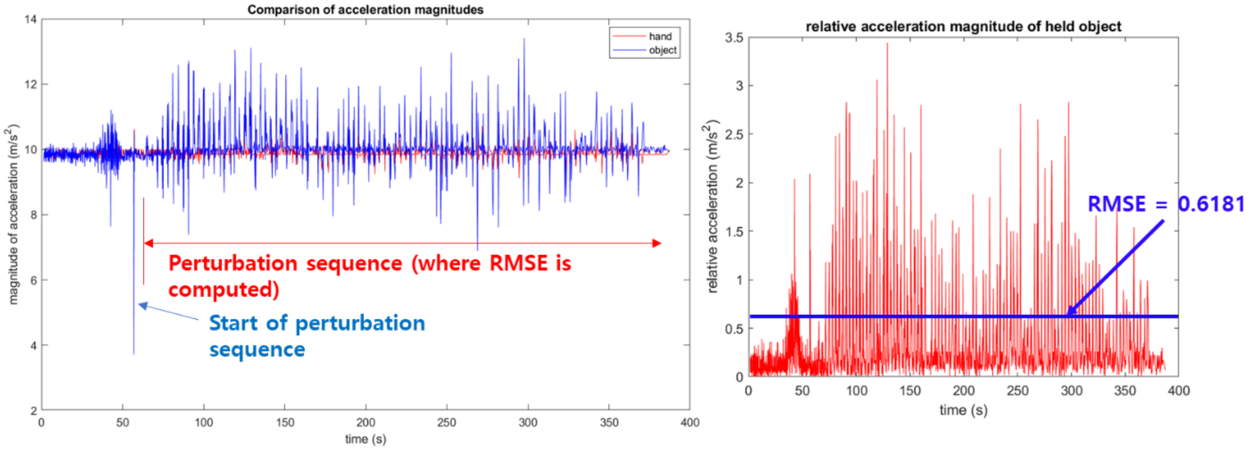

Figure 50: (left) A sample plot of the showing the magnitudes of accelerations at the wrist (red) and the object (blue). The time region corresponding to the perturbation sequences are detected starting from an initial spike in the acceleration magnitude. **(right)** Root mean square of the differences is computed for each trial.

5.4 Results

5.4.1 Summary of results

The differences in the acceleration magnitudes and the percentage of grasps retained within the trials are investigated with the perturbation experiment with the prosthetic hand and KUKA arm system. Again, a total of five objects have been grasped for the experimental trials, and six trials were executed for each torque multiplier, resulting in 360 total grasp trials (2 methods × 5 objects × 6 torque multipliers × 6 trials). Simulation for each trial lasted 310 seconds, resulting in 1860 minutes (31 hours) worth of data. Like the case with the simulated results, the magnitudes of accelerations were measured with the accelerometers at the wrist and the object and were plotted with respect to time as can be seen in Figure 50. Unlike with the simulation, however, the beginning of the perturbation sequence was also determined with the spike in the accelerometer measurements; the time of grasp failure was determined likewise.

Table 9: The average of the root mean square values of the differences in acceleration magnitudes and the standard deviation ($\boldsymbol{\mu_{acc} \pm \sigma_{acc}}$) throughout the experiment. The values are measured in m/s^2. The magnitudes of acceleration are less for all objects except for the ketchup dispenser, indicating more stable grasps with the synergy-based torque control enabled.

	Glass bottle	**Ketchup dispenser**	**Spray bottle**	**Cereal box**	**Cubic prism**
Synergy enabled	**1.3169±0.2575**	**1.1139±0.1288**	**1.5770±0.1387**	**1.2382±0.3558**	**0.8757±0.0530**
Uniform torques	**1.5508±0.1790**	**1.1117±0.3213**	**1.8445±0.1035**	**1.2677±0.3919**	**1.0038±0.0699**

A simple summary of the average root mean square differences in acceleration magnitudes from the perturbation experiments are shown in Table 9. Results from Table 9 somewhat agree with the results attained from the simulation; however, the average RMS value for the ketchup dispenser is higher with the synergy-enable control. Again, the differences are most drastic with the spray bottle. Grasps were retained for all torque multipliers for the ketchup dispenser, spray bottle, and the cereal box; failures in grasps were observed with low torque multipliers (and for some high torque multipliers using the uniform control method) for the glass bottle and the cubic prism. As with the simulation, t-tests were performed, and the corresponding p-values were computed.

Table 10: T-tests performed for all torque multipliers for grasping the glass bottle. Null hypotheses are rejected with 5% significance level, and effect sizes are greater than 0.8 for multipliers 0.6 to 0.9.

	Torque multiplier (c)					
	0.4	**0.5**	**0.6**	**0.7**	**0.8**	**0.9**
$t(6)$	**1.6929**	**-1.3382**	**-3.5049**	**-6.2358**	**-8.7568**	**-177.0846**
p-value	**0.15**	**0.24**	**0.017**	**0.0016**	**3.2e-4**	**1.0e-10**
Effect	**0.9472**	**0.0883**	**1.7733**	**3.3843**	**4.1041**	**80.7603**

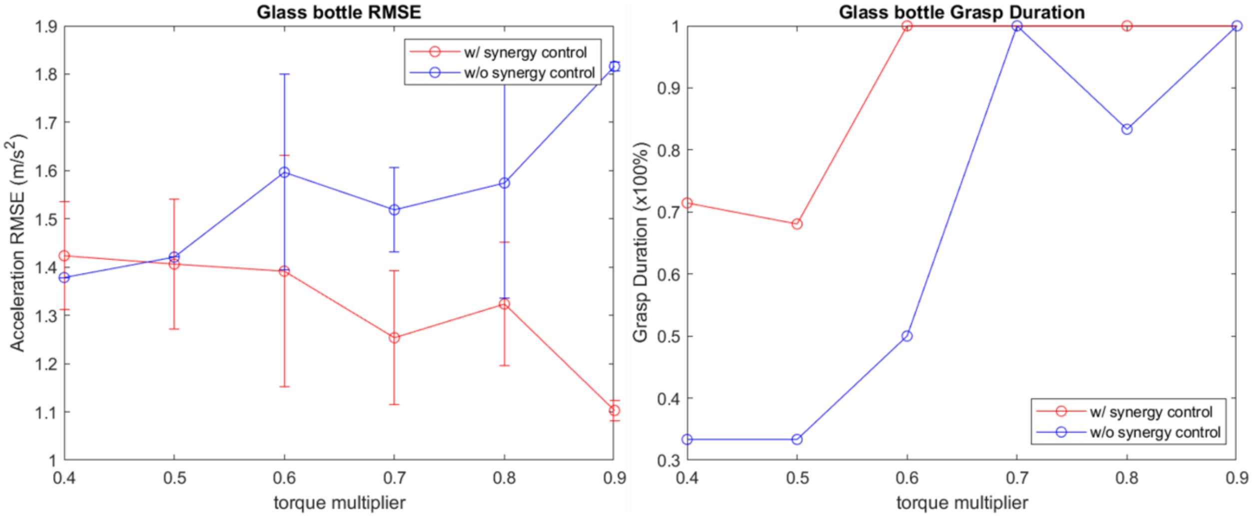

Figure 51: Results from the perturbation trials with the glass bottle. **(left)** Plot of the average root mean square of differences in acceleration magnitudes with error bars. **(right)** Percentage of grasp retained throughout the trials plotted also as failure of grasps did occur with the glass bottle.

5.4.2 T-test based analysis of perturbation trials

Figure 51 shows the mean and standard deviation throughout all trials for each torque multiplier for the glass bottle. For the glass bottle, except at the torque multiplier of 0.4, the average root mean square errors were lower with synergy-based torque control for all other torque multipliers. A generally decreasing trend of the RMSE with increasing torque multipliers is observed except for a slight increase (< 5%) at c = 0.8. Table 10 show statistically non-trivial differences between the two methods at torque multipliers 0.6 to 0.9 with $p < 0.05$, rejecting the Null hypothesis with 95% confidence. Also, the effect sizes are greater than 0.8 for multipliers greater than 0.6. Thus,

Table 11: T-tests performed for all torque multipliers for grasping the cubic prism. Null hypotheses are rejected with 5% significance level, and effect sizes are greater than 0.8 for multipliers 0.4, 0.6, 0.7, and 0.8.

	Torque multiplier (c)					
	0.4	**0.5**	**0.6**	**0.7**	**0.8**	**0.9**
$t(6)$	**-7.0832**	**-1.0596**	**-11.2693**	**-21.9797**	**-2.8871**	**-1.5803**
p-value	**8.7e-4**	**0.34**	**9.6e-5**	**3.6e-6**	**0.034**	**0.17**
Effect	**5.1072**	**1.8547**	**8.0656**	**14.4863**	**2.4290**	**1.9675**

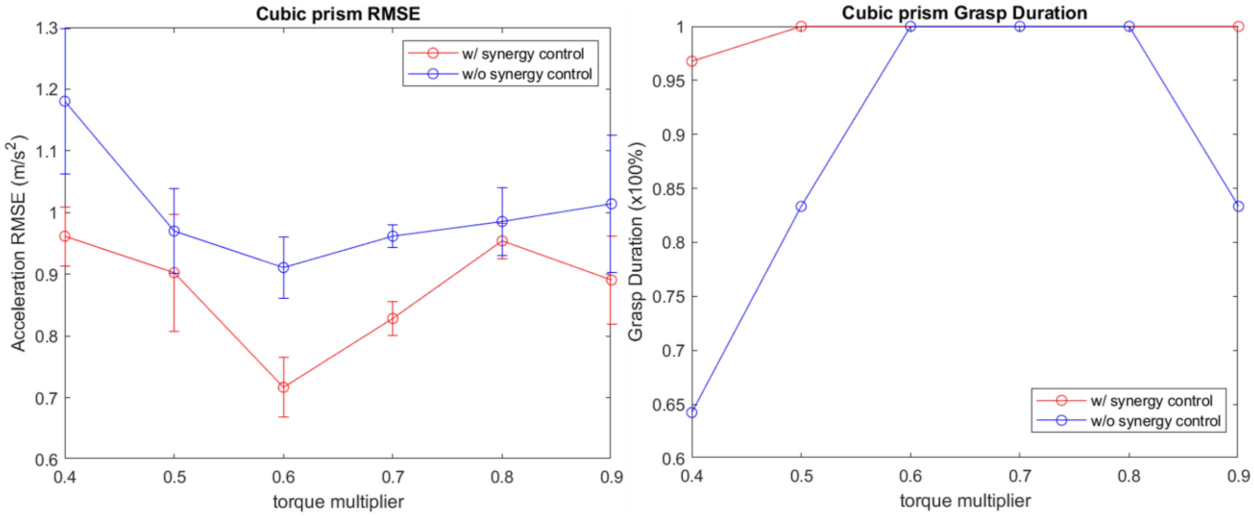

Figure 52: Results from the perturbation trials with the cubic prism. **(left)** Plot of the average root mean square of differences in acceleration magnitudes with error bars. **(right)** Percentage of grasp retained throughout the trials plotted also as failure of grasps did occur with the glass bottle.

an argument can be made that increasing the net torque improved stability of grasps with the synergy-based torque control overall. In the case of uniform torque distribution, increasing the net torque did not improve the stability of grasps with the glass bottle; in fact, an increasing trend is observed with the torque multipliers. This agrees with the observations that were made with the simulated results that a non-optimal span of contact forces does not aid in improving the stability of grasps. As observed in the simulation, a generally increasing trend in the grasp durations was observed for both methods with increasing torque multipliers. Overall, the grasp duration with synergy-based control was greater than or equal to those without synergy-enabled control.

Figure 52 shows the mean and standard deviation throughout all trials for each torque multiplier for the cubic prism. For the cubic prism, the average root mean square errors were lower with synergy-based torque control at all torque multipliers. However, a decreasing trend of the average root mean square errors were not observed with increasing torque multiplier values with the synergy-based method. The lightness of the mass of the cubic prism may account for the fact that increasing the magnitudes of the net contact forces does not affect the quality of grasps as much as with heavier objects. Increasing the net torque with the uniform torque distribution slightly improved the stability of grasps within 0.4 to 0.6 torque multiplier values. Table 11 shows statistically non-trivial differences between the two methods for torque multipliers 0.4, 0.6, 0.7, and 0.8 with $p < 0.05$, rejecting the Null hypothesis with 95% confidence. Also, the effect sizes are greater than 0.8 for multipliers greater than 0.4. Thus, an argument can be made that the stability of grasps improved with the synergy-based torque control definitively for certain torque multipliers; for others, no definitive conclusions can be drawn statistically, but lower RMS values were observed, nonetheless. Increases in the grasp durations were observed for both methods with increasing torque multipliers, but a few cases of grasp failures were observed with the non-synergistic method at torque multiplier 0.9. Overall, the grasp duration was higher with the synergy-based torque control.

Table 12: T-tests performed for all torque multipliers for grasping the cereal box. Null hypotheses are not rejected for all multipliers at 5% significance level.

	Torque multiplier (c)					
	0.4	**0.5**	**0.6**	**0.7**	**0.8**	**0.9**
$t(6)$	**-0.1275**	**-1.5266**	**-0.4265**	**-1.0452**	**-0.6717**	**-0.8174**
p-value	**0.90**	**0.19**	**0.69**	**0.34**	**0.53**	**0.45**
Effect	**0.0707**	**0.4771**	**0.3889**	**0.5354**	**0.0139**	**0.4836**

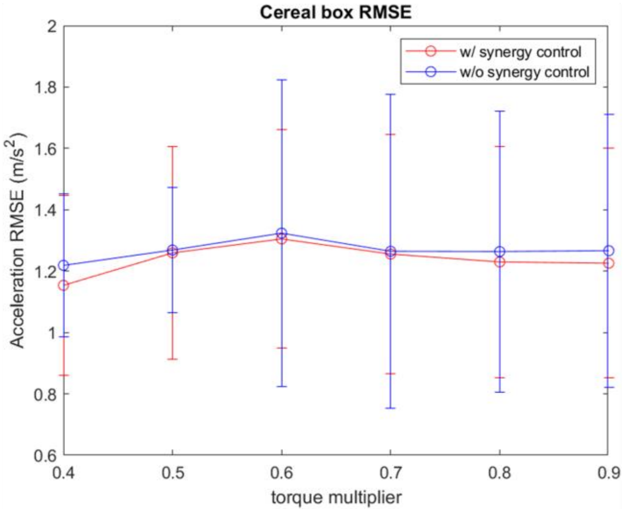

Figure 53: Results from the perturbation trials with the cereal box. Plot of the average root mean square of differences in acceleration magnitudes with error bars.

Figure 53 shows the mean and standard deviation throughout all trials for each torque multiplier for the cereal box. For the cereal box, the average root mean square errors were slightly lower with synergy-based torque control at all torque multipliers. Decreasing trends of the average root mean square errors were not observed with increasing torque multiplier values with both the synergy-based method and the uniform torque modulation method. In the case of the cereal box, Table 12 suggests that statistically non-trivial differences between the two methods at torque multipliers are not observed for all multipliers with $p > 0.05$, failing to reject the Null hypothesis with 95% confidence. The inconclusiveness of the results complies with those observed in the simulated experiments; the lack of contact points that constrain the object's perpendicular motion

Table 13: T-tests performed for all torque multipliers for grasping the ketchup dispenser. Null hypothesis rejected only at torque multiplier 0.5 at 5% significance level; however, the effect size is 0.4433, a less than moderate difference in RMSE.

	Torque multiplier (c)					
	0.4	**0.5**	**0.6**	**0.7**	**0.8**	**0.9**
$t(6)$	**-1.1120**	**-2.8921**	**1.9165**	**0.2040**	**1.6339**	**0.5130**
p-value	**0.32**	**0.034**	**0.11**	**0.85**	**0.16**	**0.63**
Effect	**0.4411**	**0.4433**	**0.8926**	**0.0306**	**0.7792**	**0.1227**

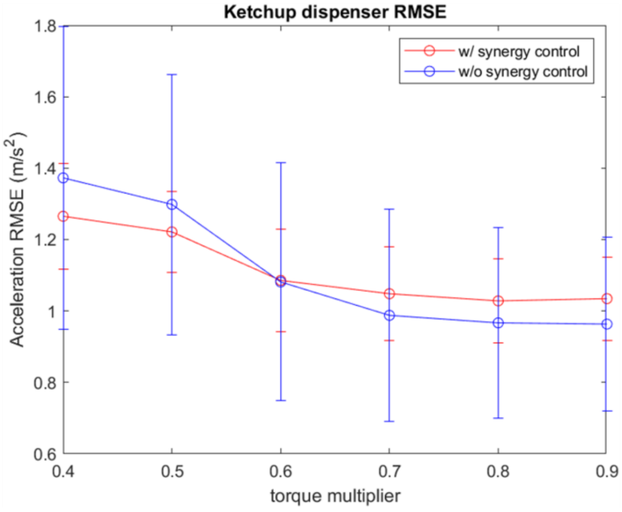

Figure 54: Results from the perturbation trials with the ketchup dispenser. Plot of the average root mean square of differences in acceleration magnitudes with error bars.

does not help with observing improved grasp stability with the synergy-based torque modulation method. Grasps were maintained 100% for all the trials, thus no comparison could be made in terms of the grasp robustness.

Figure 54 shows the mean and standard deviation throughout all trials for each torque multiplier for the ketchup dispenser. For the ketchup dispenser, the average root mean square errors were lower with synergy-based torque control only at torque multipliers 0.4 and 0.5. Also, a decreasing trend of the average root mean square errors were observed with increasing torque multiplier values for both synergy-based and uniform torque modulation method. Table 13 shows

Table 14: T-tests performed for all torque multipliers for grasping the spray bottle. Null hypotheses are rejected at all torque multipliers at 5% significance level. Also, the effect sizes are greater than 0.8 for all multipliers.

	Torque multiplier (c)					
	0.4	**0.5**	**0.6**	**0.7**	**0.8**	**0.9**
$t(6)$	**-8.0871**	**-3.2473**	**-5.2347**	**-9.3539**	**-7.0755**	**-12.0940**
p-value	**4.7e-4**	**0.023**	**0.0034**	**2.4e-4**	**8.7e-4**	**6.8e-5**
Effects	**4.9047**	**0.9071**	**3.0488**	**5.2164**	**5.8112**	**6.1362**

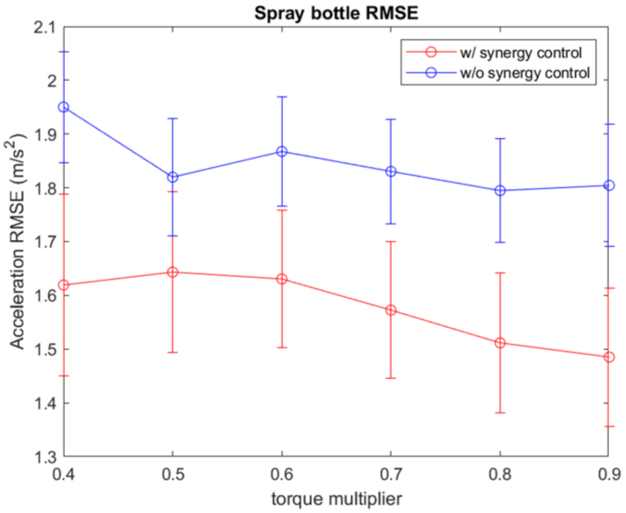

Figure 55: Results from the perturbation trials with the spray bottle. Plot of the average root mean square of differences in acceleration magnitudes with error bars.

statistically non-trivial differences between the two methods only for torque multipliers 0.5 with $p < 0.05$, rejecting the Null hypothesis with 95% confidence; however, the differences are not significant as the effect size is less than 0.5, and less than moderate difference between the two methods is observed. This result somewhat complies with the observations from the simulated experiment as differences in the RMSE in regions 0.4 to 1.0 torque multipliers are small ($< 0.05 \frac{m}{s^2}$), and measurement error with the accelerometers are much higher ($0.22 \frac{m}{s^2}$). Again, for the ketchup dispenser, grasps were maintained 100% for all the trials, thus no comparison could be made in terms of the grasp robustness.

Figure 55 shows the mean and standard deviation throughout all trials for each torque multiplier for the spray bottle. For the spray bottle, the average root mean square errors were lower with synergy-based torque control at all torque multipliers. Also, a decreasing trend of the average root mean square errors were observed with increasing torque multiplier values for both methods. Table 14 shows statistically non-trivial differences between the two methods for all torque multipliers with $p < 0.05$, rejecting the Null hypothesis with 95% confidence. Also, the effect sizes are greater than 0.8 for all multipliers. Thus, an argument can be made that the stability of grasps improved with the synergy-based torque control definitively for all torque multipliers with the spray bottle. Grasps were maintained 100% for all the trials, thus no comparison could be made in terms of the grasp robustness.

Overall, the root mean square values are lower using the synergy-enabled torque control compared to the uniform control method for the glass bottle, cubic prism, and spray bottle. Statistical validation agrees with some of the results attained from simulation with strong improvements in the grasp stability with the glass bottle and spray bottle. Unlike simulated results using the ketchup dispenser, improved grasp stability is not observed in physical experimentation. This is expected as improved grasps were observed at lower torque multipliers with the simulation ($c = 0.1$ to 0.3), where the lowest tested torque multiplier for the physical experiment was 0.4. The performances of grasps with the cubic prism were unexpectedly good compared to those in simulation. This discrepancy may arise from the differences in the contact characteristics specific to the stereolithography design (STL) used in simulation compared to the actual contact characteristics of the cubic prism. Also, while the fidelity of the simulation was tested with a set of virtual experiments, the contact dynamics in terms of restitution and friction may be different from those in the real world; thus, real-world results may be more reliable than those in simulation.

CHAPTER 6

CONCLUSION

6.1 Research contributions

The data-driven design and control method of a semi-anthropomorphic prosthetic hand is proposed in this thesis. Through this work, progress is made in the development of reduced-degrees of freedom grasps from human subject experiments, and a data-driven design and control method of an upper-limb prosthesis is explored. Additionally, this thesis introduces the utilization of synergistic contact forces to stabilize grasps while applying postural synergies in forming grasp poses to maximize the functionalities of a prosthetic hand. These are all accomplished while keeping the cost of fabrication and the overall weight below those for some of the more sophisticated robotic upper-limb prostheses on market. Two main methods are developed in this thesis to develop a data-based design and control of a semi-anthropomorphic hand:

1. **Grasp characterization with kinematics and contact dynamics of daily grasps:** A database of grasps is attained from human subject experimentation with daily objects to extract the core kinematic and contact kinetic components of grasps. Machine learning methods such as PCA and LDA are adopted to develop a grasp synergy matrix and grasp classifiers that allow mapping between the grasp feature space and the latent space represented by the principal components from the database. Using these mapping methods, anthropomorphic grasps are translated to robotic grasps by using virtual spheres that are generated by a set of contact points at the fingertips and the palm. The performances of the classifiers and the synergy matrix are evaluated using classification metrics such as Calinski-Harabasz indices, F1-scores, and confusion matrices.

2. **Data-driven design and control of a semi-anthropomorphic prosthetic hand:** The results from the grasp database and literature study on the correlation of the hand digits in daily grasp motivate the design and control method of a semi-anthropomorphic hand. The number of digits is reduced to three to reduce control complexity and power requirements. The prosthetic hand is controlled using synergistic mapping of the pose and contact forces of the human hand to the robotic hand model. The functionality of the semi-anthropomorphic hand and improved grasp stability using the proposed grasp dataset are first validated with simulation using CoppeliaSim. After statistical validation of the benefits of synergy-based modulation of joint pose and torques using t-tests, the physical system is also tested by mounting the semi-anthropomorphic hand system to the KUKA serial manipulator. Grasp stability is evaluated again with t-tests and improved stability with synergy-based joint pose and torque modulation is observed.

6.2 Applications and future works

The dataset of grasp kinematics and contact kinetics have numerous potential applications and expansion to future research not only in robotic grasps but also in non-robotics related fields such as sports therapy, grasp rehabilitation of stroke patients, and grasp synthetic in virtual environments.

In the field of robotic upper-limb prostheses, future designs may allow modification of grasp choices not by the individual digits of the hand, but by the object to be grasped using control variables in the latent space of the grasp dataset as demonstrated in this thesis work. For example, combined pose and contact force inputs can be used in the EMG control of a soft synergy-inspired robotic hand by Fani. et. al., where in addition to their EMG-based generation of robotic hand poses, piezoresistive pressure sensors can be added to the fingertips such that contact forces can be modulated simultaneously so that the generated grasps are similar to natural human grasps [111]. Furthermore, this thesis work demonstrates the improvement in grasp stability and robustness by utilizing the combined synergy matrix of grasp kinematics and contact kinetics; thus, strategic methods in joint torque modulation of synergistic robotics hands (e.g. the four-finger tendon-driven hand by Yen et. al. or the synergy-inspired three-fingered hand by Chen et. al.) may be adopted for improved grasp stability and dexterity [77][78][80].

Another example for application of this work include rehabilitation for patients with impaired grasps. Currently, the most adopted rehabilitation method for recovering healthy grasps of stroke patients is the Graded Repetitive Arm Supplementary Program (GRASP), where the clinicians monitor the kinematics and kinetics of grasps while providing psychological support for the patient to perform the rehabilitation tasks [112]. However, automation of the GRASP program may be accomplished with a therapeutic gaming system, where the grasp database established in this thesis work is used as a baseline for the patients to obtain healthy grasps of daily objects, while also getting psychological support by providing a metric in the improvement of grasps as many video games do with scoring systems.

6.3 Summary

This thesis work demonstrates a data-driven approach to designing and controlling a semi-anthropomorphic hand. While the span of objects test is limited to a subset of daily objects and statistical validation is even more limited to a smaller subset, significant differences between the synergy-enabled grasp methods and the previous methods are observed from classification tests, simulated experiments, and experiments with the physical system. It is hoped that this thesis work makes meaningful contributions to the progress in closing the gap between the functionality of the human hand and robotic upper limb prostheses.

Appendices

APPENDIX A

MASS OF VOLUME OF OBJECTS USED IN HUMAN SUBJECT TRIALS

Objects	Grasp Taxonomy	Volume (cm^3)	Mass (g)
Tennis ball	power sphere	157.5	57.2
Glass bottle	medium wrap	102.51	194.4
Kitchen spoon	light tool	41.53	48.5
Book	parallel extension	1172.86	908
Bowl	palmar	77.03	332.8
Credit card	lateral	2.42	2.1
CD	precision disk	11.14	14.6
Cereal box	parallel extension	1682.69	219.1
Comb	adducted thumb	22.05	19.8
Game controller	lateral	69.15	111.4
Cubic prism	sphere finger	129.8	30.6
Dish	parallel extension	180.43	816.5
Dispenser	medium wrap	386.47	37.3
Door lever	small diameter	92.84	323.4
Dust brush	medium wrap	293.99	94.9
Fork	prismatic finger	5.59	5.7
Hammer	small diameter	415.08	913.1
Lid of a jar	precision disk	17.02	13.1
Key	tip pinch	0.6	1.1
Knife	index finger extension	27.58	17.8
Measuring cup	adducted thumb	28.1	24.8
Milk carton	large diameter	1890.56	604.7
Mouse	precision sphere	14.16	64.1
Mug	lateral	164.2	377.1
Notebook	parallel extension	621.4	249.5
Peeler	adducted thumb	26.99	16.8
Pen	writing tripod	9.97	12.1
Tape roll	small diameter	357.69	140
Screwdriver	prismatic finger	5.75	5.4
Spoon	prismatic finger	4.98	4.5
Spray	sphere finger	495.11	486.7842
Espresso cup	tip pinch	49.88	114.8
Toothbrush	stick	29.78	17.7
Tumbler	large diameter	314.97	195
Whiskey glass	large diameter	72.91	304.3

APPENDIX B

GRASP TAXONOMY [25]

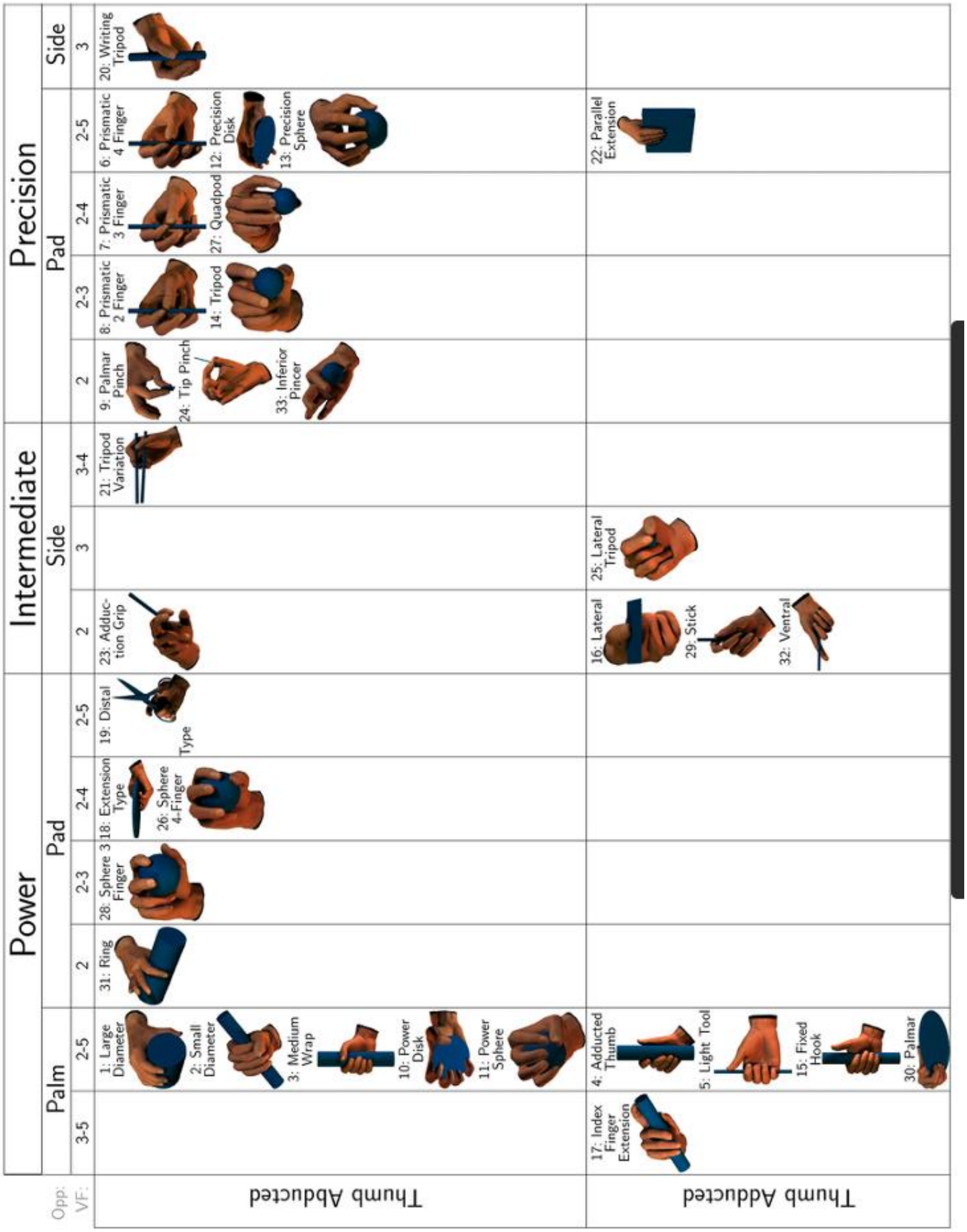

APPENDIX C

CASES OF GRASP SUCCESSES AND FAILURES

GLASS BOTTLE:

	Multiplier											
	0.4		**0.5**		**0.60**		**0.7**		**0.8**		**0.9**	
Trial #	**w**	**w/o**	**w**	**w/o**	**w**	**w/o**	**w**	**w/o**	**w**	**w/o**	**w**	**w/o**
1 (rotation)	X	X	X	X	O	X	O	O	O	O	O	O
2 (linear)	O	X	X	X	O	X	O	O	O	O	O	O
3	X	O	O	O	O	O	O	O	O	O	O	O
4	X	X	O	X	O	O	O	O	O	X	O	O
5	X	X	O	X	O	O	O	O	O	O	O	O
6	O	X	X	X	O	X	O	O	O	O	O	O
O =	SUCCESS											
X =	FAILURE											

CUBIC PRISM:

	Multiplier											
	0.4		**0.5**		**0.60**		**0.7**		**0.8**		**0.9**	
Trial #	**w**	**w/o**	**w**	**w/o**	**w**	**w/o**	**w**	**w/o**	**w**	**w/o**	**w**	**w/o**
1(rotation)	O	X	O	X	O	O	O	O	O	O	O	O
2 (linear)	X	X	O	O	O	O	O	O	O	O	O	O
3	O	O	O	O	O	O	O	O	O	O	O	X
4	O	O	O	O	O	O	O	O	O	O	O	O
5	O	X	O	O	O	O	O	O	O	O	O	O
6	X	O	O	O	O	O	O	O	O	O	O	O
O =	SUCCESS											
X =	FAILURE											

CEREAL BOX:

	Multiplier											
	0.4		**0.5**		**0.60**		**0.7**		**0.8**		**0.9**	
Trial #	**w**	**w/o**	**w**	**w/o**	**w**	**w/o**	**w**	**w/o**	**w**	**w/o**	**w**	**w/o**
1(rotation)	O	O	O	O	O	O	O	O	O	O	O	O
2 (linear)	O	O	O	O	O	O	O	O	O	O	O	O
3	O	O	O	O	O	O	O	O	O	O	O	O
4	O	O	O	O	O	O	O	O	O	O	O	O
5	O	O	O	O	O	O	O	O	O	O	O	O
6	O	O	O	O	O	O	O	O	O	O	O	O
O =	SUCCESS											
X =	FAILURE											

KETCHUP DISPENSER

	Multiplier											
	0.4		**0.5**		**0.60**		**0.7**		**0.8**		**0.9**	
Trial #	**w**	**w/o**	**w**	**w/o**	**w**	**w/o**	**w**	**w/o**	**w**	**w/o**	**w**	**w/o**
1(rotation)	O	O	O	O	O	O	O	O	O	O	O	O
2 (linear)	O	O	O	O	O	O	O	O	O	O	O	O
3	O	O	O	O	O	O	O	O	O	O	O	O
4	O	O	O	O	O	O	O	O	O	O	O	O
5	O	O	O	O	O	O	O	O	O	O	O	O
6	O	O	O	O	O	O	O	O	O	O	O	O
O =	SUCCESS											
X =	FAILURE											

SPRAY BOTTLE:

	Multiplier											
	0.4		**0.5**		**0.60**		**0.7**		**0.8**		**0.9**	
Trial #	**w**	**w/o**	**w**	**w/o**	**w**	**w/o**	**w**	**w/o**	**w**	**w/o**	**w**	**w/o**
1(rotation)	O	O	O	O	O	O	O	O	O	O	O	O
2 (linear)	O	O	O	O	O	O	O	O	O	O	O	O
3	O	O	O	O	O	O	O	O	O	O	O	O
4	O	O	O	O	O	O	O	O	O	O	O	O
5	O	O	O	O	O	O	O	O	O	O	O	O
6	O	O	O	O	O	O	O	O	O	O	O	O
O =	SUCCESS											
X =	FAILURE											

REFERENCES

[1] Armour, B. S., Courtney-Long, E. A., Fox, M. H., Fredine, H., Cahill, A. (2016). Prevalence and causes of paralysis—United States, 2013. American Journal of Public Health, 106(10), 1855–1857. https://doi.org/10.2105/ajph.2016.303270

[2] F. Cordella, A. L. Ciancio, R. Sacchetti, A. Davalli, A. G. Cutti, E. Guglielmelli, and L. Zollo, "Literature review on needs of upper limb prosthesis users," Frontiers in Neuroscience, vol. 10, 2016.

[3] B. Maat, G. Smit, D. Plettenburg, and P. Breedveld, "Passive prosthetic hands and Tools," *Prosthetics & Orthotics International*, vol. 42, no. 1, pp. 66–74, 2018.

[4] G. Gioioso, G. Salvietti, M. Malvezzi, and D. Prattichizzo, "An object-based approach to map human hand synergies onto robotic hands with dissimilar kinematics," Robotics: Science and Systems VIII, 2012.

[5] M. Ciocarlie, C. Goldfeder, and P. Allen, "Dimensionality reduction for hand-independent dexterous robotic grasping," 2007 IEEE/RSJ International Conference on Intelligent Robots and Systems, 2007.

[6] I. M. Bullock, J. Z. Zheng, S. De La Rosa, C. Guertler, and A. M. Dollar, "Grasp frequency and usage in daily household and machine shop tasks," IEEE Transactions on Haptics, vol. 6, no. 3, pp. 296–308, 2013.

[7] M. Santello and J. F. Soechting, "Force synergies for multifingered grasping," *Experimental Brain Research*, vol. 133, no. 4, pp. 457–467, 2000.

[8] M. A. Roa, R. Koiva, and C. Castellini, "Experimental evaluation of human grasps using a sensorized object," 2012 4th IEEE RAS EMBS International Conference on Biomedical Robotics and Biomechatronics (BioRob), 2012.

[9] S. A. Winges, S. E. Eonta, J. F. Soechting, and M. Flanders, “Multi-digit control of contact forces during rotation of a hand-held object,” *Journal of Neurophysiology*, vol. 99, no. 4, pp. 1846–1856, 2008.

[10] L. Sartori, E. Straulino, and U. Castiello, “How objects are grasped: The interplay between affordances and end-goals,” *PLoS ONE*, vol. 6, no. 9, 2011.

[11] T.H. Pham, N. Kyriazis, A. A. Argyros, and A. Kheddar, “Hand-object contact force estimation from Markerless Visual Tracking,” IEEE Transactions on Pattern Analysis and Machine Intelligence, vol. 40, no. 12, pp. 2883–2896, 2018.

[12] P. K. Allen, A. Timcenko, B. Yoshimi, and P. Michelman, “Automated Tracking and grasping of a moving object with a robotic hand-eye system,” IEEE Transactions on Robotics and Automation, vol. 9, no. 2, pp. 152–165, 1993.

[13] S. Sundaram, P. Kellnhofer, Y. Li, J.-Y. Zhu, A. Torralba, and W. Matusik, “Learning the signatures of the human grasp using a scalable tactile glove,” *Nature*, vol. 569, no. 7758, pp. 698–702, 2019.

[14] Y. M. Zhou, D. Wagner, K. Nuckols, R. Heimgartner, C. Correia, M. Clarke, D. Orzel, C. O'Neill, R. Solinsky, S. Paganoni, and C. J. Walsh, “Soft robotic glove with integrated sensing for intuitive grasping assistance post spinal cord injury,” *2019 International Conference on Robotics and Automation (ICRA)*, 2019.

[15] F. Vecchi, S. Micera, F. Zaccone, M. C. Carrozza, A. M. Sabatini, and P. Dario, “A sensorized glove for applications in biomechanics and motor control,” Proceedings of the 2001 Conference of the International FES Society, 2001.

[16] P. Eccarius, R. Bour, and R. A. Scheidt, “Dataglove measurement of joint angles in Sign language handshapes,” *New Methodologies in Sign Language Phonology: Papers from TISLR 10*, vol. 15, no. 1, pp. 39–72, 2012.

[17] R. D. Flint, J. M. Rosenow, M. C. Tate, and M. W. Slutzky, “Continuous decoding of human grasp kinematics using epidural and subdural signals,” Journal of Neural Engineering, vol. 14, no. 1, p. 016005, 2016.

[18] C. Della Santina, M. Bianchi, G. Averta, S. Ciotti, V. Arapi, S. Fani, E. Battaglia, M. G. Catalano, M. Santello, and A. Bicchi, “Postural hand synergies during environmental constraint exploitation,” *Frontiers in Neurorobotics*, vol. 11, 2017.

[19] M. R. Cutkosky, “On grasp choice, grasp models, and the design of hands for manufacturing tasks,” *IEEE Transactions on Robotics and Automation*, vol. 5, no. 3, pp. 269–279, 1989.

[20] M. Santello, M. Flanders, and J. F. Soechting, “Postural hand synergies for tool use,” *The Journal of Neuroscience*, vol. 18, no. 23, pp. 10105–10115, 1998.

[21] N. Kamakura, M. Matsuo, H. Ishii, F. Mitsuboshi, and Y. Miura, “Patterns of static prehension in normal hands,” *The American Journal of Occupational Therapy*, vol. 34, no. 7, pp. 437–445, 1980.

[22] S. J. Lederman and R. L. Klatzky, “Hand movements: A window into haptic object recognition,” *Cognitive Psychology*, vol. 19, no. 3, pp. 342–368, 1987.

[23] N. Jarrassé, A. Ribeiro, A. Sahbani, W. Bachta, and A. Roby-Brami, “Analysis of hand synergies in healthy subjects during bimanual manipulation of various objects,” *Journal of NeuroEngineering and Rehabilitation*, vol. 11, no. 1, p. 113, 2014.

[24] S. H. Ahn, S. Kwon, Y. Na, and M. H. Yun, “Grasp behavior analysis using muscle and postural hand synergies for smartphones,” *International Journal of Precision Engineering and Manufacturing*, vol. 22, no. 4, pp. 697–707, 2021.

[25] T. Feix, J. Romero, H.-B. Schmiedmayer, A. M. Dollar, and D. Kragic, “The grasp taxonomy of human grasp types,” *IEEE Transactions on Human-Machine Systems*, vol. 46, no. 1, pp. 66–77, 2016.

[26] J. Romero, T. Feix, C. H. Ek, H. Kjellstrom, and D. Kragic, “Extracting postural synergies for robotic grasping,” IEEE Transactions on Robotics, vol. 29, no. 6, pp. 1342–1352, 2013.

[27] M. Santello and J. F. Soechting, “Gradual molding of the hand to object contours,” Journal of Neurophysiology, vol. 79, no. 3, pp. 1307–1320, 1998.

[28] J. Starke, C. Eichmann, S. Ottenhaus, and T. Asfour, “Synergy-based, data-driven generation of object-specific grasps for anthropomorphic hands,” 2018 IEEE-RAS 18th International Conference on Humanoid Robots (Humanoids), 2018.

[29] T. Calinski and J. Harabasz, “A dendrite method for cluster analysis,” Communications in Statistics - Theory and Methods, vol. 3, no. 1, pp. 1–27, 1974.

[30] Divya, V., Devi, K. N. (2018). An efficient approach to determine number of clusters using principal component analysis. 2018 International Conference on Current Trends towards Converging Technologies (ICCTCT). https://doi.org/10.1109/icctct.2018.8551182

[31] Cangelosi, R., & Goriely, A. (2007). Component retention in principal component analysis with application to cDNA microarray data. Biology Direct, 2(1), 2. https://doi.org/10.1186/1745-6150-2-2

[32] R. A. FISHER, “The use of multiple measurements in taxonomic problems,” Annals of Eugenics, vol. 7, no. 2, pp. 179–188, 1936.

[33] Q. Liu, M. Li, C. Yin, G. Qian, W. Meng, Q. Ai, and J. Hu, “CNN-based hand grasping prediction and control via postural synergy basis extraction,” Sensors, vol. 22, no. 3, p. 831, 2022.

[34] J. Li, M. Yang, Y. Liu, Q. Zheng, and D. Wang, “Dynamic Hand Gesture Recognition Using Multi-direction 3D Convolutional Neural Networks,” Engineering Letters, vol. 27, no. 3, 2019.

[35] E. Zhang, B. Xue, F. Cao, J. Duan, G. Lin, and Y. Lei, “Fusion of 2D CNN and 3D DenseNet for dynamic gesture recognition,” Electronics, vol. 8, no. 12, p. 1511, 2019.

[36] J. McNeil, "Americans with disabilities: Household economic studies (No. P70-73)," Washington, DC: US Census Bureau, 2001.

[37] P. Maciejasz, J. Eschweiler, K. Gerlach-Hahn, A. Jansen-Troy, and S. Leonhardt, “A survey on robotic devices for Upper Limb Rehabilitation,” Journal of NeuroEngineering and Rehabilitation, vol. 11, no. 1, 2014.

[38] S. Katz, "Assessing self-maintenance: activities of daily living, mobility, and instrumental activities of daily living," J. of the American Geriatrics Society, vol. 31, no. 12, pp. 721-727, 1983.

[39] M. Marino, S. Pattni, M. Greenberg, A. Miller, E. Hocker, S. Ritter, and K. Mehta, “Access to prosthetic devices in developing countries: Pathways and challenges,” 2015 IEEE Global Humanitarian Technology Conference (GHTC), 2015.

[40] “Upper Limb Prosthetics Market Share Report 2022-2028,” Global Market Insights Inc. [Online]. Available: https://www.gminsights.com/industry-analysis/upper-limb-prosthetics-market.

[41] H. Mano, S. Noguchi, S. Fujiwara, and N. Haga, “Relationship between degree of disability, usefulness of assistive devices, and daily use duration: An investigation in children with congenital upper limb deficiencies who use upper limb prostheses,” Assistive Technology, pp. 1–6, 2021.

[42] L. Resnik, M. R. Meucci, S. Lieberman-Klinger, C. Fantini, D. L. Kelty, R. Disla, and N. Sasson, “Advanced Upper Limb Prosthetic Devices: Implications for upper limb prosthetic rehabilitation,” Archives of Physical Medicine and Rehabilitation, vol. 93, no. 4, pp. 710–717, 2012.

[43] E. A. Biddiss and T. T. Chau, “Upper limb prosthesis use and abandonment,” Prosthetics Orthotics International, vol. 31, no. 3, pp. 236–257, 2007.

[44] A. P. Johnson and B. Veatch, “Upper-extremity prostheses: A renewed approach,” Volume 8: 14th Design for Manufacturing and the Life Cycle Conference; 6th Symposium on International Design and Design Education; 21st International Conference on Design Theory and Methodology, Parts A and B, 2009.

[45] Hudspeth Stevenson, E., McAlinden, M., Gaffney, K., Hudspeth Stevenson, E. (2022). A retrospective review of the Bebionic multiarticulating hand. are patients continuing to use the hands? https://doi.org/10.26226/m.621602804a84e7b4701eb832

[46] K. F. Gretsch, H. D. Lather, K. V. Peddada, C. R. Deeken, L. B. Wall, and C. A. Goldfarb, “Development of novel 3D-printed robotic prosthetic for Transradial Amputees,” Prosthetics Orthotics International, vol. 40, no. 3, pp. 400–403, 2016.

[47] S. L. Carey, D. J. Lura, and M. J. Highsmith, “Differences in myoelectric and body-powered upper-limb prostheses: Systematic Literature Review,” JPO Journal of Prosthetics and Orthotics, vol. 29, no. 4S, 2017.

[48] A. Fougner, Ø. Stavdahl, P. J. Kyberd, Y. G. Losier, and P. A. Parker, “Control of upper limb prostheses: Terminology and proportional myoelectric control—a review,” IEEE Transactions on Neural Systems and Rehabilitation Engineering, vol. 20, no. 5, pp. 663–677, 2012.

[49] L. Resnik, S. L. Klinger, and K. Etter, “The Deka Arm,” Prosthetics Orthotics International, vol. 38, no. 6, pp. 492–504, 2014.

[50] A. H. Al-Timemy, R. N. Khushaba, G. Bugmann, and J. Escudero, “Improving the performance against force variation of EMG controlled multifunctional upper-limb prostheses for Transradial amputees,” IEEE Transactions on Neural Systems and Rehabilitation Engineering, vol. 24, no. 6, pp. 650–661, 2016.

[51] D. Estay, A. Basoalto, J. Ardila, M. Cerda, and R. Barraza, “Development and implementation of an anthropomorphic underactuated prosthesis with adaptive grip,” Machines, vol. 9, no. 10, p. 209, 2021.

[52] Y. Wang, Y. Tian, H. She, Y. Jiang, H. Yokoi, and Y. Liu, “Design of an effective prosthetic hand system for adaptive grasping with the control of Myoelectric Pattern Recognition Approach,” Micromachines, vol. 13, no. 2, p. 219, 2022.

[53] J. A. Lerman, E. Sullivan, D. A. Barnes, and R. J. Haynes, “The Pediatric Outcomes Data Collection Instrument (PODCI) and functional assessment of patients with unilateral upper extremity deficiencies,” Journal of Pediatric Orthopaedics, vol. 25, no. 3, pp. 405–407, 2005.

[54] K. A. Raichle, “Prosthesis use in persons with lower- and upper-limb amputation,” The Journal of Rehabilitation Research and Development, vol. 45, no. 7, pp. 961–972, 2008.

[55] N. Fallahian, H. Saeedi, H. Mokhtarinia, and F. Tabatabai Ghomshe, “Sensory feedback add-on for upper-limb prostheses,” Prosthetics Orthotics International, vol. 41, no. 3, pp. 314–317, 2017.

[56] C. MEDYNSKI and B. RATTRAY, “Bebionic prosthetic design,” Myoelectric Symposium, 2011.

[57] O. van der Niet, R. M. Bongers, and C. K. van der Sluis, “Functionality of I-limb and I-Limb Pulse Hands: Case Report,” Journal of Rehabilitation Research and Development, vol. 50, no. 8, pp. 1123–1128, 2013.

[58] T. Jarus and R. Poremba, “Hand function evaluation: A factor analysis study,” The American Journal of Occupational Therapy, vol. 47, no. 5, pp. 439–443, 1993.

[59] K. Matheus and A. M. Dollar, “Benchmarking grasping and manipulation: Properties of the objects of daily living,” 2010 IEEE/RSJ International Conference on Intelligent Robots and Systems, 2010.

[60] M. Liu and C. Xiong, “Synergistic characteristic of human hand during grasping tasks in daily life,” Intelligent Robotics and Applications, pp. 67–76, 2014.

[61] M. A. Roa and R. Suárez, “Grasp quality measures: Review and Performance,” Autonomous Robots, vol. 38, no. 1, pp. 65–88, 2014.

[62] H. Dang and P. K. Allen, “Learning grasp stability,” 2012 IEEE International Conference on Robotics and Automation, 2012.

[63] K. Harada, T. Tsuji, S. Uto, N. Yamanobe, K. Nagata, and K. Kitagaki, “Stability of soft-finger grasp under gravity,” 2014 IEEE International Conference on Robotics and Automation (ICRA), 2014.

[64] R. M. Murray, Z. Li, and S. S. Sastry, “A mathematical introduction to robotic manipulation,” 2017.

[65] C. Y. Brown and H. H. Asada, “Inter-finger coordination and postural synergies in Robot Hands via mechanical implementation of Principal Components Analysis,” 2007 IEEE/RSJ International Conference on Intelligent Robots and Systems, 2007.

[66] K. Xu, H. Liu, Y. Du, X. Sheng, and X. Zhu, “Mechanical implementation of postural synergies using a simple continuum mechanism,” 2014 IEEE International Conference on Robotics and Automation (ICRA), 2014.

[67] F. Ficuciello, A. Federico, V. Lippiello, and B. Siciliano, “Synergies evaluation of the Schunk S5FH for grasping control,” Advances in Robot Kinematics 2016, pp. 225–233, 2017.

[68] M. E. Puhaindran, S. J. Sebastin, A. Y. Lim, W. X. Xu, and Y. M. Chen, “Absence of flexor digitorum superficialis tendon in the little finger is not associated with decreased grip strength,” Journal of Hand Surgery (European Volume), vol. 33, no. 2, pp. 205–207, 2008.

[69] X. Liu and Q. Zhan, “Description of the human hand grasp using graph theory,” Medical Engineering Physics, vol. 35, no. 7, pp. 1020–1027, 2013.

[70] A. Buryanov and V. Kotiuk, “Proportions of hand segments,” International Journal of Morphology, vol. 28, no. 3, 2010.

[71] T. Nilsen, M. Hermann, C. S. Eriksen, H. Dagfinrud, P. Mowinckel, and I. Kjeken, “Grip force and pinch grip in an adult population: Reference values and factors associated with Grip Force,” Scandinavian Journal of Occupational Therapy, vol. 19, no. 3, pp. 288–296, 2011.

[72] D. U. Ozsahin, M. Hejazi, O. S. Adnan, H. Alloush, A. Khabbaz, J. B. Idoko, B. B. Duwa, and I. Ozsahin, “Designing a 3D printed artificial hand,” Modern Practical Healthcare Issues in Biomedical Instrumentation, pp. 3–18, 2022.

[73] “Body segment data,” ExRx.net: Exercise Prescription on Internet. [Online]. Available: https://exrx.net/Kinesiology/Segments.

[74] W. Williams, “Bionic hand price list,” Bionics For Everyone, 12-Apr-2022. [Online]. Available: https://bionicsforeveryone.com/bionic-hand-price-list/.

[75] A. Boeing and T. Bräunl, “Evaluation of real-time physics simulation systems,” Proceedings of the 5th international conference on Computer graphics and interactive techniques in Australia and Southeast Asia - GRAPHITE '07, 2007.

[76] G. Grioli, M. Catalano, E. Silvestro, S. Tono, and A. Bicchi, “Adaptive synergies: An approach to the design of under-actuated robotic hands,” 2012 IEEE/RSJ International Conference on Intelligent Robots and Systems, 2012.

[77] W. Chen, Z. Xiao, J. Lu, Z. Zhao, and Y. Wang, “Design and analysis of a synergy-inspired three-Fingered hand,” 2020 IEEE International Conference on Robotics and Automation (ICRA), 2020.

[78] R. Ozawa, K. Hashirii, Y. Yoshimura, M. Moriya, and H. Kobayashi, “Design and control of a three-fingered tendon-driven robotic hand with active and passive tendons,” Autonomous Robots, vol. 36, no. 1-2, pp. 67–78, 2013.

[79] I. M. Bullock and A. M. Dollar, “A two-fingered underactuated anthropomorphic manipulator based on human precision manipulation motions,” 2016 IEEE International Conference on Robotics and Automation (ICRA), 2016.

[80] W. Yan, H. Nie, J. Chen, and D. Han, “Optimal design and grasp ability evaluation of four-finger tendon-driven hand,” International Journal of Advanced Robotic Systems, vol. 14, no. 6, p. 172988141774844, 2017.

[81] R. Balasubramanian, Ling Xu, P. D. Brook, J. R. Smith, and Y. Matsuoka, “Human-guided grasp measures improve grasp robustness on physical robot,” 2010 IEEE International Conference on Robotics and Automation, 2010.

[82] D. Prattichizzo, J. K. Salisbury, and A. Bicchi, “Contact and grasp robustness measures: Analysis and experiments,” Experimental Robotics IV, pp. 83–90, 1997.

[83] D. Seita, F. T. Pokorny, J. Mahler, D. Kragic, M. Franklin, J. Canny, and K. Goldberg, “Large-scale supervised learning of the grasp robustness of surface patch pairs,” 2016 IEEE International Conference on Simulation, Modeling, and Programming for Autonomous Robots (SIMPAR), 2016.

[84] J. Mahler, M. Matl, X. Liu, A. Li, D. Gealy, and K. Goldberg, “DEX-NET 3.0: Computing robust vacuum suction grasp targets in point clouds using a new analytic model and Deep Learning,” 2018 IEEE International Conference on Robotics and Automation (ICRA), 2018.

[85] M. Zechmair and Y. Morel, “Assessing grasp quality using local sensitivity analysis,” 2021 IEEE/RSJ International Conference on Intelligent Robots and Systems (IROS), 2021.

[86] H. Bruyninckx, S. Demey, and V. Kumar, “Generalized stability of compliant grasps,” Proceedings. 1998 IEEE International Conference on Robotics and Automation (Cat. No.98CH36146).

[87] W. S. Howard and V. Kumar, “On the stability of grasped objects,” IEEE Transactions on Robotics and Automation, vol. 12, no. 6, pp. 904–917, 1996.

[88] Hao Dang and P. K. Allen, “Grasp adjustment on novel objects using tactile experience from similar local geometry,” 2013 IEEE/RSJ International Conference on Intelligent Robots and Systems, 2013.

[89] H. Dang and P. K. Allen, “Stable grasping under pose uncertainty using tactile feedback,” Autonomous Robots, vol. 36, no. 4, pp. 309–330, 2013.

[90] D. D. Damian, M. Fischer, A. Hernandez Arieta, and R. Pfeifer, “The role of quantitative information about slip and grip force in prosthetic grasp stability,” Advanced Robotics, vol. 32, no. 1, pp. 12–24, 2017.

[91] A. Naceri, A. Moscatelli, M. Santello, and M. O. Ernst, “Coordination of multi-digit positions and forces during unconstrained grasping in response to object perturbations,” 2014 IEEE Haptics Symposium (HAPTICS), 2014.

[92] R. Barone, A. L. Ciancio, R. A. Romeo, A. Davalli, R. Sacchetti, E. Guglielmelli, and L. Zollo, “Multilevel control of an anthropomorphic prosthetic hand for grasp and slip prevention,” Advances in Mechanical Engineering, vol. 8, no. 9, p. 168781401666508, 2016.

[93] C. Piazza, A. M. Simon, K. L. Turner, L. A. Miller, M. G. Catalano, A. Bicchi, and L. J. Hargrove, “Exploring augmented grasping capabilities in a multi-synergistic soft Bionic Hand,” Journal of NeuroEngineering and Rehabilitation, vol. 17, no. 1, 2020.

[94] V. Patel, M. Martin, and I. Florescu, “A Novel Biometric based on Neural Representations of Synergistic Hand Grasps,” Future Technologies Conference, 2017.

[95] C. Fricke, R. Gentner, J.-J. Rumpf, D. Weise, D. Saur, and J. Classen, “Differential spatial representation of precision and power grasps in the Human Motor System,” NeuroImage, vol. 158, pp. 58–69, 2017.

[96] J. Ritter, “An efficient bounding sphere,” Graphics Gems, pp. 301–303, 1990.

[97] B. Siciliano, O. Khatib, D. Prattichizzo, and J. C. Trinkle, “Grasping,” in Springer Handbook of Robotics, Berlin: Springer, 2016, pp. 955–988.

[98] J. C. F. De Winter, “Using the Student's t-test with extremely small sample sizes,” Practical Assessment, Research, and Evaluation, vol. 18, 2013.

[99] J. Shao and H. Feng, “Group sequential T-test for clinical trials with small sample sizes across stages,” Contemporary Clinical Trials, vol. 28, no. 5, pp. 563–571, 2007.

[100] G. Salvietti, M. Z. Iqbal, and D. Prattichizzo, “Bilateral haptic collaboration for human-robot cooperative tasks,” IEEE Robotics and Automation Letters, vol. 5, no. 2, pp. 3517–3524, 2020.

[101] N. Hong, M. Kim, C. Lee, and S. Kim, “Head-mounted interface for intuitive vision control and continuous surgical operation in a surgical robot system,” Medical Biological Engineering Computing, vol. 57, no. 3, pp. 601–614, 2018.

[102] J. Bolarinwa, I. Eimontaite, T. Mitchell, S. Dogramadzi, and P. Caleb-Solly, “Assessing the role of gaze tracking in optimizing humans-in-the-loop telerobotic operation using multimodal feedback,” Frontiers in Robotics and AI, vol. 8, 2021.

[103] J. Cohen, “Statistical Power Analysis for the behavioral sciences,” 2013.

[104] R. A. Romeo, F. Cordella, L. Zollo, D. Formica, P. Saccomandi, E. Schena, G. Carpino, A. Davalli, R. Sacchetti, and E. Guglielmelli, “Development and preliminary testing of an instrumented object for force analysis during grasping,” 2015 37th Annual International Conference of the IEEE Engineering in Medicine and Biology Society (EMBC), 2015.

[105] V. Prado da Fonseca, T. E. Alves de Oliveira, and E. M. Petriu, “Estimating the orientation of objects from tactile sensing data using machine learning methods and visual frames of reference,” Sensors, vol. 19, no. 10, p. 2285, 2019.

[106] J. Lobo, P. Trindade, and J. Dias, “Observing hand grasp type and contact points using hand distributed accelerometers and instrumented objects,” IEEE ICRA, 2011.

[107] J. Fan, J. He, and S. I. Tillery, “Control of hand orientation and arm movement during reach and grasp,” Experimental Brain Research, vol. 171, no. 3, pp. 283–296, 2005.

[108] M. Hallett, “Faculty opinions recommendation of virtual lesions of the anterior intraparietal area disrupt goal-dependent on-line adjustments of grasp.,” Faculty Opinions – Post-Publication Peer Review of the Biomedical Literature, 2005.

[109] D. A. Nowak, J. Hermsdörfer, E. Schneider, and S. Glasauer, “Moving objects in a rotating environment: Rapid prediction of coriolis and centrifugal force perturbations,” Experimental Brain Research, vol. 157, no. 2, 2004.

[110] A. Takagi, G. Xiong, H. Kambara, and Y. Koike, “Endpoint stiffness magnitude increases linearly with a stronger power grasp,” Scientific Reports, vol. 10, no. 1, 2020.

[111] S. Fani, M. Bianchi, S. Jain, J. S. Pimenta Neto, S. Boege, G. Grioli, A. Bicchi, and M. Santello, “Assessment of myoelectric controller performance and kinematic behavior of

a novel soft synergy-inspired robotic hand for Prosthetic Applications," Frontiers in Neurorobotics, vol. 10, 2016.

[112] J. E. Harris, J. J. Eng, W. C. Miller, and A. S. Dawson, "A self-administered graded repetitive arm supplementary program (GRASP) improves arm function during inpatient stroke rehabilitation," Stroke, vol. 40, no. 6, pp. 2123–2128, 2009.